Coffin, M.F., Frey, F.A., Wallace, P.J., et al., 2000
Proceedings of the Ocean Drilling Program, Initial Reports Volume 183

4. Site 1136[1]

Shipboard Scientific Party[2]

BACKGROUND AND OBJECTIVES

Site 1136 was one of two sites drilled on the southern Kerguelen Plateau (SKP) during Leg 183 (Fig. F1). The collapse of Hole 1135A (see "Operations," p. 2, in the "Site 1135" chapter) before reaching igneous basement forced us to consider alternatives for sampling basaltic crust of the SKP. Because the sediment formation responsible for making us abandon Site 1135 appeared to be of similar thickness and reflection character at the JOIDES Pollution Prevention and Safety Panel–approved alternate site, we used multichannel seismic (MCS) data provided by the Ocean Drilling Program (ODP) site-survey data bank to select a new alternate site. Site 1136 is on the SKP approximately midway between two previous sites where basaltic basement was recovered, Site 738 (Leg 119) and Site 750 (Leg 120). Site 1136 is 8 km west of the fault scarp marking the eastern boundary of the SKP with the Labuan Basin (Fig. F1). To maximize our chances of sampling igneous basement, we located Site 1136 on *Marion Dufresne* MCS line MD47/10 (Fig. F2), where the water depth is 1931 m and sediment thickness is only 133 m. Here, ~32 km from Site 1135, the chert-rich formation that created hole instability at Site 1135 appeared to be either thin or absent on the MCS data. The sedimentary section at Site 1136 is characterized by moderate- to high-amplitude continuous reflections, and the reflection from the top of basaltic basement is strong and continuous and has an apparent 1° dip to the west (Fig. F3). West of the site, a wedge of intrabasement reflections also has an apparent westward dip. The wedge is disrupted by normal faults and terminates against an interpreted normal fault 12 km west of Site 1136. To the east of the site, one major fault and several minor faults offset igneous basement >3000 m downward into the Labuan Basin (Rotstein et al., 1991). Although most motion on these faults delineating the northeastern boundary of the SKP probably occurred in

F1. Satellite-derived free-air gravity map of the Kerguelen Plateau, p. 34.

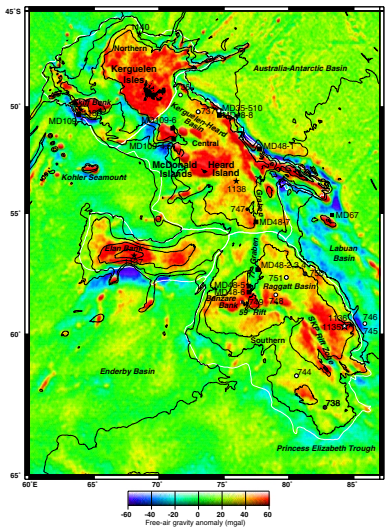

F2. Location of Site 1136 and site-survey data, p. 36.

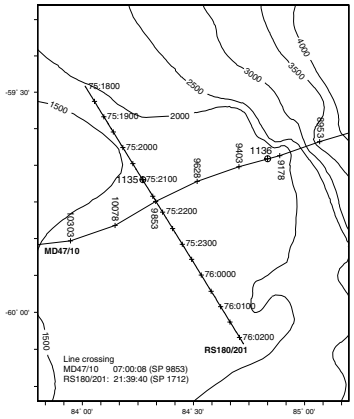

[1]Examples of how to reference the whole or part of this volume.
[2]Shipboard Scientific Party addresses.

Cretaceous time, earthquake activity along the scarp continues today (Okal, 1981; Adams and Zhang, 1984).

Summary of Objectives

The main objectives at this site were to

1. Characterize the petrography and compositions of the lavas, with particular focus on testing for the presence of a continental lithospheric component found in Site 738 basalt to the south, but not identified in Site 750 basalts to the north (Fig. F1) (see "Background and Objectives," p. 1, in the "Site 1135" chapter);
2. Determine the age of the lavas testing the hypothesis that the uppermost igneous basement of the SKP is ~110 Ma, the age yielded by basalts from Sites 738, 749, and 750;
3. Determine the physical characteristics of the lava flows;
4. Identify the environment of eruption (subaerial or submarine);
5. Obtain minimum estimates for the age of the basement from overlying sediment;
6. Estimate the duration of possible subaerial and shallow marine environments from the sedimentary and igneous record;
7. Determine the facies of the two seismic stratigraphic sequences;
8. Define the ages of seismic sequence boundaries;
9. Determine the paleoceanographic history of this high-latitude site.

F3. *Marion Dufresne* cruise 47, line 10 multichannel seismic profile across Site 1136, p. 37.

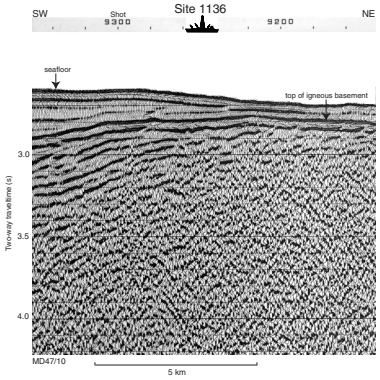

OPERATIONS

Site 1136

The 32-km move to Site 1136 was made in dynamic positioning mode in 7.75 hr. The ship arrived at Site 1136 early on the morning of 27 December 1998. Weather conditions upon arrival were 3- to 6-m swells, ~1-m seas, and wind from 228° at 17 kt gusting to 19 kt. At 0530 hr on 27 December 1998, we deployed a beacon on the precise Global Positioning System coordinates for Site 1136.

Hole 1136A

We spudded Hole 1136A at 1215 hr 27 December 1998, using the rotary core barrel (RCB) coring assembly and an RBI C-7 core bit. The depth of the seafloor was 1930.6 m below sea level. Continuous wireline coring proceeded in homogeneous white foraminifer-bearing nannofossil ooze interspersed with thin chert layers to a depth of 60.9 mbsf. Recovery for this interval was 74.7%, and the average rate of penetration (ROP) was 41.9 m/hr. The formation then graded into a pale brown foraminifer-bearing calcareous ooze. The average recovery dropped in this 19.0-m-interval to 41.7%, and the average ROP increased to 51.8 m/hr. The interval from 79.9 to 128.0 mbsf consisted of sand and silt. Recovery through this interval was an extremely poor 0.9%, and the average ROP decreased to 23.1 m/hr. At a depth of ~133.0 mbsf (Core 183-1136A-15R), the driller noted a dramatic slowing of the drilling rate, indicating that basement had been encountered. Coring continued in basalt to a depth of 161.4 mbsf, or ~28 m into basement. Recovery in basement was 55.0%, but the ROP was very low (2.8 to 1.1

m/hr). A summary of core numbers, depths, and recovery is given in Tables T1 and T2.

Because the ROP was so slow and the limited basement recovery allowed some of the scientific objectives to be achieved, a decision was made to abandon further coring into basement. The previously planned wireline logging program was also canceled because very little basement had been penetrated (~28 m) and the amount of hole that could be logged (~85 m) was limited compared with the time required. By making this decision, we were able to regain the time lost during the transit south and depart Site 1136 essentially on schedule for the remaining 5 "primary" drill sites of the leg.

While the drill string was being recovered, the positioning beacon was released and, incredibly, came up inside the lower guide horn of the ship. This required partially pulling the upper guide horn. The beacon was ultimately recovered at 1115 hr on 29 December 1998. The ship was secured for transit, and, at 1130 hr on 29 December 1998, we were under way for Site 1137.

Only two icebergs were observed during operations at Site 1136. Neither posed any threat to the drilling operation. The closest point of approach for the two icebergs was 32 and 10 km, respectively.

T1. Coring summary, p. 81.

T2. Expanded coring summary, p. 82.

LITHOSTRATIGRAPHY

Introduction

Site 1136 is located in 1948.4 m of water on the eastern margin of the SKP, 8 km west of the Labuan Basin. This site is located 32 km east of Site 1135 and was chosen because the sediments overlying basement appeared on seismic profiles to be only ~150 m thick. Hole 1136A was rotary cored continuously to a depth of 161.4 mbsf. Sediments were recovered from approximately the upper 130 m, and basalts were recovered from approximately the lower 30 m of the hole (Fig. F4). The sedimentary section consists of ~66 m of pelagic ooze that overlies about 48 m of zeolitic calcareous silty clay and clayey sand (Table T3). We recognize five sedimentary units in Hole 1136A. The basalts at the base of the hole are designated as Unit VI and are described in "Physical Volcanology," p. 10, "Igneous Petrology," p. 17, "Alteration and Weathering," p. 20, and "Structural Geology," p. 22. Cores 183-1136A-1R (0–4.70 mbsf) and 8R (60.90–70.30 mbsf) had no recovery; hence, they are not included in any of the sedimentary units (Fig. F4). Core recovery was poor throughout the sedimentary section of the hole. Even in the upper 75 m of the hole, where recovery appears to be relatively high (Fig. F4), portions of many of the recovered intervals are very disturbed by drilling and appear to be flow-in.

F4. Composite stratigraphic section, p. 38.

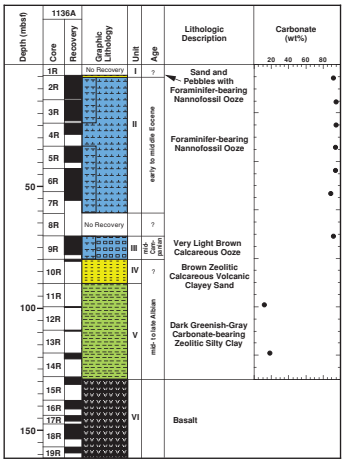

T3. Summary of lithologic units, p. 84.

Unit I

Interval: 183-1136A-2R-1, 0 cm, to 2R-1, 118 cm
Depth: 4.70–5.88 mbsf
Age: Pleistocene(?)

Unit I is highly disturbed mixed clastic sediment (intervals 183-1136A-2R-1, 0–44 cm, and 95–118 cm) and ooze (interval 183-1136A-2R-1, 44–118 cm). Pebble lithologies are varied, including granite and gneiss. The sand, granules, and pebbles are ice-rafted debris that was

concentrated during drilling, probably by washing out of the fine-grained pelagic sediment. The boundary with Unit II is arbitrarily placed at Section 183-1136A-2R-1, 118 cm, which is the lowest occurrence of concentrated sands and pebbles. We recognize that all the sediment recovered from Unit I has been highly disturbed by drilling, and, thus, the true composition of the sediment in this unit is uncertain.

Unit II

Interval: 183-1136A-2R-1, 118 cm, to 7R-CC, 25 cm
Depth: 5.88–60.90 mbsf
Age: early to middle Eocene

Unit II consists of white foraminifer-bearing nannofossil ooze that is similar to the ooze recovered in Subunit IIA of Hole 1135A. All of the cores in Unit II of Hole 1136A contain soupy intervals, suggesting that much of the recovered material flowed into the cores. Scattered pebbles and chert fragments are found at several locations. Within undisturbed intervals, the ooze is homogeneous and bioturbation is absent to slight. The carbonate content of this unit is 89–95 wt% $CaCO_3$(Fig. **F4**). The upper and lower boundaries of Unit II are uncertain because of the absence of recovery in Cores 183-1135A-1R and 8R.

Unit III

Interval: 183-1136A-9R-1, 0 cm, to 9R-CC, 5 cm
Depth: 70.30–79.90 mbsf
Age: mid-Campanian

This unit consists predominantly of very light brown foraminifer-bearing calcareous ooze. Some undisturbed intervals contain sediment that is partially cemented and lithified. The carbonate is predominantly micrite, and a sample of ooze from the top of the unit yielded a carbonate content of 92 wt% $CaCO_3$ (Fig. **F4**). X-ray diffraction (XRD) analyses indicate the presence of only minor amounts of clay minerals and possibly quartz (Table **T4**). The light brown color is caused by disseminated (<5%), silt-sized palagonitized basaltic glass shards. These yellowish grains are as much as 0.3 mm in diameter, generally oblate or tabular, and subangular to subrounded. They are nonvesicular and do not contain crystallites; however, they display internal polygonal ("jigsaw") quench textures. Inoceramid fragments are present in Sections 183-1136A-9R-6 and 9R-CC. A pebble at the top of Core 183-1136A-9R was most likely emplaced during drilling. Several intervals of the core are disturbed or soupy.

T4. XRD results and calcium carbonate contents expressed as $CaCO_3$, **p. 85.**

Unit IV

Interval: 183-1136A-10R-1, 0 cm, to 10R-1, 100 cm
Depth: 79.90–89.50 mbsf
Age: mid- to late Albian

The dominant lithology in Unit IV is brown zeolitic calcareous volcanic clayey sand, which constitutes a 1-m-thick bed in Core 183-1136A-10R. This bed is reversely graded, with medium sand in interval 183-1136A-10R-1, 0–25 cm, and fine sand below. The sand is well sorted and individual grains are subangular to subrounded and moderately spheri-

cal. Several rounded, centimeter-sized pebbles in the middle of the bed are of a similar dark brown indurated lithology. The composition of the sand is predominantly white grains of carbonate and aggregates of zeolite. Minor amounts of orange to yellow palagonitized basaltic glass shards, minor green glauconitic foraminifer casts, and trace amounts of opaque silt also are found in the sand. The palagonitized shards range up to 1 mm in diameter, are nonvesicular, do not contain crystallites, and display granulated textures suggestive of quenching. These shards resemble those in the overlying Unit III. Calcareous nannofossils are rare.

In smear slides, abundant zeolites are observed to be tabular prisms as much as 20 µm long. XRD indicates that these zeolites are dominantly clinoptilolite with minor heulandite. XRD also indicates that minor amounts of nontronite (a dioctahedral Fe smectite) and plagioclase are present. X-ray fluorescence (XRF) analysis of two samples indicates a total Fe content of 13%–14%, which is consistent with the estimated abundance of the Fe-bearing components (palagonite, glauconitic foraminifer casts, and nontronite).

A thin interval of breccia at the base of Unit IV (interval 183-1136A-1R-1, 87–92 cm) consists of brown angular fragments in a brown matrix. The material is noncalcareous and possibly silicified. The fragments are internally brecciated, indicating repeated brecciation. The contact between this breccia and the overlying sand appears to be sharp; however, the relationship between this breccia and the overlying sand is not clear.

Unit V

Interval: 183-1136A-11R-1, 0 cm, to 15R-1, 8 cm
Depth: 89.50–128.08 mbsf
Age: mid- to late Albian

Unit V is dark greenish gray carbonate-bearing zeolitic silty clay. This unit is massive, except for a thin sand bed in interval 183-1136A-14R-1, 30–40 cm, and a thin, normally graded sand bed with a sharp base in interval 183-1136A-14R-1, 139–140 cm. Fossil debris is common, including bryozoans, bivalves, and sponge spicules. The fossils do not appear to be in growth positions; however, the presence of an articulated bivalve suggests a quiet depositional environment. Foraminifers, including both planktonic and benthic species and calcareous nannofossils, are present (<5%). Palagonitized basaltic glass shards also are present (<5%). Burrows are common. Dark green clay is found in streaks and as halos around burrows.

The carbonate content of Unit V sediment is relatively low (12–18 wt% $CaCO_3$) (Fig. **F4**). The XRD analyses indicate calcite, clinoptilolite, heulandite, glauconite, and minor nontronite are present in the sediment. An analysis of the dark green clay from Core 183-1136A-15R indicates that it is a mixture of celadonite, saponite, and nontronite. XRF analyses indicate 5–8 wt% total Fe_2O_3, which probably is in celadonite, palagonite, glauconite, and/or nontronite.

Unit V appears to directly overlie the basalt basement; however, the nature of this lower contact is uncertain. Drilling records indicate that basalt was encountered at ~133 mbsf (see **"Operations,"** p. 2), slightly deeper than the base of Unit V, which was placed at the contact between Unit V sediments and basalt (128.08 m) in Core 183-1136A-15R. Three pieces from Core 183-1136A-15R, presumably from the base of

Unit V, are particularly rich in fossil fragments, including bryozoans, bivalve, and ostracode fragments.

Discussion

Lower Cretaceous basalt flows (Unit VI) are mantled by fine-grained volcanic sediments of Unit V, which were deposited in a neritic environment beginning in early Albian time. This sediment was deposited below wave base and the high diversity of shelly fossils (bivalves, bryozoans, ostracodes, and benthic foraminifers) suggests a shallow shelf environment, whereas the presence of calcareous nannofossils indicates communication with the open ocean. The oldest sediments were altered, along with the uppermost basalts (which host identical celadonite veins, see **"Alteration and Weathering,"** p. 20) in this shelf environment. The overlying brown volcanic sand (Unit IV) was probably also deposited in a shelf environment, and its grain size and size-sorting, and the presence of rounded pebbles indicate a somewhat higher energy environment. The intervening breccia (at the base of Unit IV) is probably a result of hydrothermal alteration rather than subaerial exposure.

The calcareous ooze of overlying Unit III records deepening to pelagic conditions by Turonian/Santonian time. Sparse palagonitized basaltic glass shards, with internal quench textures, indicate either minor submarine volcanism through this interval or reworking of older material. The oozes of Unit II document pelagic sedimentation during Eocene time, with major hiatuses before (Late Cretaceous to Paleocene) and after (Oligocene to Pleistocene) deposition of this unit.

BIOSTRATIGRAPHY

Site 1136 is located at 59°S on the eastern margin of the SKP, ~35 km east of Site 1135. The relatively thin (~162 m) sediment sequence above basement is composed of ~61 m of lower–middle Eocene foraminifer-bearing nannofossil ooze unconformably overlying ~67 m of Lower and Upper Cretaceous calcareous ooze, sands, and silty clays. The minimum sedimentation rate above and below the major unconformities, is ~10 m/m.y. (Fig. **F5**).

Relatively good recovery in Cores 183-1136A-2R through 7R revealed an expanded lower to middle Eocene section (foraminifer Zones AP7–AP6; nannofossil Zones CP12b–CP9) containing well-preserved microfossils. This interval has not been recovered from previous drill holes on the Kerguelen Plateau or any other southern high-latitude sites because recovery was prevented by chert stringers. Recovery of this key section at Site 1136A should aid in the refinement of high-latitude middle Eocene biostratigraphic zonations.

The first sediments below the unconformity (lithostratigraphic Unit III) consist of light brown ooze, of probable early Maastrichtian to Cenomanian age, containing abundant inoceramid prisms, sponge spicules, and ostracodes in addition to common planktonic foraminifers and nannofossils. A major hiatus occurs at the boundary between this unit and the zeolitic sands and silty clays of lithostratigraphic Units IV and V. These upper bathyal to outer neritic sediments contain dilute but relatively well-preserved microfossil assemblages (including palynomorphs) of probable mid- to late Albian age, indicating a minimum age for the underlying basalts of ~105–106 Ma. Marine lower Albian has not

F5. Age-depth plot, **p. 39.**

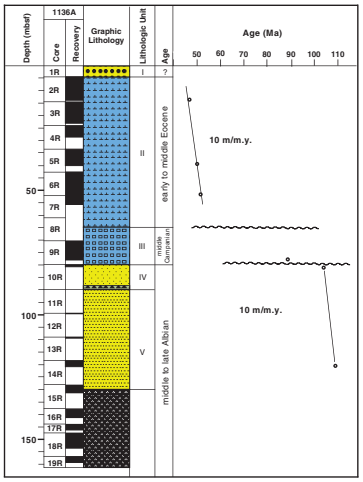

been recovered during previous drilling on the Kerguelen Plateau. The dark green sands and clays are similar in microfossil composition to Albian sediment drilled at Site 511 (Leg 71) on the Falkland Plateau and appear to be only slightly younger in age than complementary nonmarine, palynomorph-bearing lower Albian red-brown silts and claystones from Site 750 (Leg 120) on the SKP.

Calcareous Nannofossils

The first core recovered no sediment so the first material we dated was from Sample 183-1136A-2R-CC. Preservation is good and nannofossils are abundant in this sample, and, based on the presence of *Chiasmolithus solitus, Chiasmolithus* sp. cf. *Chiasmolithus grandis,* and *Neococcolithes dubius* in the absence of *Nannotetrina fulgens* and *Discoaster kuepperi,* we dated this sample as early middle Eocene (upper Zone CP12b–CP13). We also noted rare *Lapideacassis* sp. and *Coronocyclus prionion*. We assigned Sample 183-1136A-3R-CC to the same zone, although several discoasters (*Discoaster barbadiensis, Discoaster sublodoensis,* and *Discoaster praebifax*) along with *Coccolithus formosus* and *Ellipsolithus* sp. document a warmer water influence. Preservation is moderate because of overgrowths on the discoasters.

Based on the presence of common *D. kuepperi,* abundant *D. praebifax, Toweius magnicrassis,* rare *Discoaster lodoensis, Discoaster* sp. cf. *D. sublodoensis* (five rayed and overgrown) and a single but perfectly preserved specimen of *Discoaster cruciformis* (Zones CP10–CP12a), we assigned Sample 183-1136A-4R-CC to Subzone CP12a. We also noted *Sphenolithus moriformis, C. formosus,* and *Markalius inversus*.

No specimens of *D. sublodoensis* are present in Sample 183-1136A-5R-CC, which belongs to Subzone CP11b. *D. kuepperi* is common to abundant and large *T. magnicrassus* (15 µm) is common.

A few *Tribrachiatus orthostylus* are present in Sample 183-1136A-6R-CC (which also contains *D. lodoensis*) and are common in 7R-CC. On that basis we assign both to combined Zones mid-CP11a–CP10, although the former might belong one zone higher if *T. orthostylus* is reworked. Similarly, the latter sample might belong a half zone lower because it contains no impeccable *D. lodoensis*. Also present in Sample 183-1136A-7R-CC are *Sphenolithus radians, Toweius pertusus* (Zones CP5–CP10), *Discoaster binodosus* (eight rayed), and abundant *D. kuepperi* (Zones CP10–CP12b).

A marked disconformity separates the above sequence from Sample 183-1136A-9R-CC, which contains a lower Maastrichtian nannoflora strongly diluted by a buff-colored zeolitic silty clay. Present are a few *Kamptnerius magnificus, Micula decussata, Reinhardtites levis, Arkhangelskiella cymbiformis,* common *Biscutum magnum,* and a few fragmented *Watznaueria barnesae*. We noted no *Biscutum coronum* or *Nephrolithus* spp., so we assigned the sample to the lower Maastrichtian *B. magnum* Zone.

Two lithologies were represented in Sample 183-1136A-10R-CC, including a buff zeolitic clay very poor in nannofossils and rich in detrital carbonate. A dark green lithology, however, also rich in zeolite, yielded a mid-Cretaceous assemblage better represented in the subjacent core catcher, as described below.

Samples 183-1136A-11R-CC through 14R-CC (dark clay) contained an abundant and well-preserved assemblage with few to common *Axopodorhabdus albianus*. In the absence of *Eiffellithus turriseiffelii, Sollasites falklandensis*, and *Eiffellithus monechiae (= Eiffellithus* cf. *Eiffellithus exi-*

mius of authors), we assign them to the tropical/temperate nannofossil Zone NC9A of Bralower et al. (1992, 1993) or the Austral lower *Biscutum constans* Subzone of Wise and Wind (1977) and Wise (1983). This assignment assumes that *S. falklandensis* is absent form this site not because of ecological exclusion but rather extinction. Other members of the assemblage include common *Prediscosphaera columnata/avitus* (6 µm), *Prediscosphaera spinosa,* rare *Sollasites horticus,* common *Eprolithus floralis,* plus *Nannoconus truitti, Braarudosphaera africana, Octocyclus reinhardtii, Rhagodiscus splendens, Tetrapodorhabdus decorus, Cyclagelosphaera margerelii, W. barnesae, Watznaueria biporta, Watznaueria ovata, Repagalum parvidentatum, Rotelapillus laffittei, Broinsonia* sp. cf. *B. dentata, Lapideacassis* sp. cf. *L. mariae* (no spines), *B. constans,* and *Biscutum dissimilis* (in Sample 183-1136A-10R-CC).

We reproportioned the correlations of nannofossil datums given in Bralower et al. (1992, 1993, fig. 2) to the newer time scale calibration of Gradstein et al. (1995) for the Albian, and we derived a numerical age for the base of *A. albianus* of ~106 Ma. Similarly, Subzone NC9A, to which we assigned Cores 183-1136A-10R through 14R, ranges from 105 to 106 Ma. According to this recalibration of the Bralower et al. nannofossil datums, this would be the maximum age for the bottom of the sedimentary sequence at this site (or minimum age for the top of the igneous sequence). In their compilation of Lower Cretaceous nannofossil zones, Bown et al. (1998, fig. 5.2) also recognize nannofossil Subzones NC8C, 9A, and 9B and their definitions; however, these authors extend Subzone NC9A into the upper Albian, rather than confining it to the mid- Albian as do Bralower et al. (1993). In addition, Bown et al. (1998) place the last occurrence datum of *S. falklandensis* above rather than below the first occurrence datum of *A. albianus*. They do not, however, attempt to tie their datums to a linear time scale. Nevertheless, their correlations might provide closer agreement between the nannofossil and palynomorph correlations for the age of Sample 183-1136A-10R-CC, which is assigned according to palynomorphs to the upper rather than the mid-Albian (see **"Palynology,"** p. 10). Until more precise calibrations are established for Albian nannofossil zones, any numerical ages assigned to zonal boundaries must still be considered only approximate.

Planktonic Foraminifers

Planktonic foraminifers of Paleogene and Late Cretaceous age are comparable to those encountered during previous drilling on the Kerguelen Plateau and are very similar to those recovered from Sites 1135 and 1138 during Leg 183 drilling. The Eocene can be characterized in terms of the Antarctic (AP) zonal scheme of Stott and Kennett (1990; modified by Huber, 1991, and Berggren, 1992). Cita et al.'s (1997) Late Cretaceous biostratigraphy for the Southern Ocean, modified during Leg 183 drilling within the framework of Huber's (1992) Late Cretaceous Austral realm zonal scheme, is used for dating Upper Cretaceous sediments. Further refinement is needed in the Cenomanian to Campanian. Major stratigraphic gaps exist for the Early Cretaceous in the south polar region because of hiatuses and poor microfossil preservation. Therefore, no detailed zonal scheme exists for high-latitude faunas. We therefore compare foraminifers in the stratigraphically lowest part of the section to Albian assemblages encountered during Leg 71 drilling (Deep Sea Drilling Project Site 511) on the Falkland Plateau (Krasheninikov and Basov, 1983; Bralower et al., 1993).

The first core contained only sand and gravel, and we obtained no paleontological core-catcher sample. We examined core-catcher samples from all subsequent cores. Planktonic foraminifers are abundant and well preserved in the Eocene nannofossil ooze of Unit II but are less common in the Upper Cretaceous as a result of dilution by abundant inoceramid prisms. Approximately 60% of the >63-mm size fraction of washed-carbonate residue of Sample 183-1136A-9R-CC consists of these 1- to 2-mm-long calcite crystals. Rare, but moderately well-preserved, foraminifers occur in the clay-rich Albian sediments.

Cenozoic

Sample 183-1136A-2R-CC contains a well-preserved assemblage of typical high-latitude middle Eocene acarinimids, subbotinids, *Globanomalina* spp., and *Pseudohastigerina*. The age-diagnostic species include *Pseudohastigerina micra, Acarinina primitiva, Acarinina matthewsae,* and probable *Acarinina bullbrooki,* placing this sample in the zonal range AP8–AP9. *Chiloguembelina* spp. and a small six- to seven-chambered planispiral form comparable to *Praetenuitella* sp. (Huber, 1991, pl. 4, figs. 3, 4) are also common in this sample. *Acarinina matthewsae* is absent in Sample 183-1136A-3R-CC; we accordingly assign it to Zone AP8. Present in this sample and the subjacent Eocene cores is a very compressed form of *Globanomalina,* which has four chambers in the final whorl and a distinct peripheral keel. We compare this form to the Paleocene species *Globanomalina pseudomenardii*. We also found this species in Hole 1135A during Leg 183 drilling (see **"Biostratigraphy,"** p. 7, in the "Site 1135" chapter), but it has not been previously reported on the Kerguelen Plateau.

Acarinina bullbrooki is absent from the next sample downhole. We assigned this and the subjacent three samples (Samples 183-1136A-5R-CC to 7R-CC) to the AP7 interval that ranges from the last occurrence of *A. bullbrooki* to the base of the *An. primitiva* range. Other common elements of the fauna are *Globanomalina planoconicus, Globanomalina australiformis, Subbotina velascoensis, Guembelitrioides* spp., and *Chiloguembelina cubensis*. The first appearance datum of *P. micra* is found approximately within the middle of Zone AP7 (Huber, 1991). On this basis, we assign Samples 183-1136A-4R-CC to 6R-CC, containing *P. micra,* to the upper part of this zone, and Sample 183-1136A-7R-CC, in which *P. micra* is absent, to the lower part of Zone AP7. We obtained no core catcher for Core 183-1136A-8R.

Mesozoic

The middle Eocene foraminifer-bearing ooze of Unit II unconformably overlies a short interval (~15 m) of light brown calcareous ooze dated as Late Cretaceous. The core catcher of the single core representing this interval (Sample 183-1136A-9R-CC) is dominated by inoceramid prisms but contains relatively common and well-preserved Campanian planktonic foraminifers. The assemblage includes *Globigerinelloides multispinus, Heterohelix globulosa, Heterohelix planata, Archeoglobigerina australis, Schackoina multispinata, Globotruncana* spp., and *Globigerinelloides impensus*. *Globigerinelloides impensus* is a late Campanian marker. The presence of this species allowed us to place the sample in the total range zone bearing that name. It occurs with a small planispiral form resembling *G. impensus,* which is comparable to *Globigerinelloides* sp. recorded by Huber (1990, pl. 1, figs. 8, 9) and Quilty

(1992, pl. 1, figs. 22, 23) and present in the Campanian across the Kerguelen Plateau (see "Biostratigraphy," p. 7, in the "Site 1135" chapter, "Biostratigraphy," p. 8, in the "Site 1137" chapter, and "Biostratigraphy," p. 10, in the "Site 1138" chapter). Inoceramid prisms are common in samples of this age.

The zeolitic sands and silty clays of Unit IV and V that lie unconformably below the Campanian nannofossil ooze contain extremely rare but relatively well-preserved planktonic foraminifers. Among the abundant detrital carbonate grain aggregates and zeolite crystals in Samples 183-1136A-11R-CC to 14R-CC, we find impoverished, low-diversity assemblages that lack characteristic Upper Cretaceous taxa, but contain small genera such as *Globigerinelloides*, *Hedbergella*, and *Schackoina*. We found the best preserved and abundant microfossils of this interval in Sample 183-1136A-14R-CC. In this sample, we recognized *Hedbergella planispira* and *Hedbergella delrioensis*. The occurrence of these species in the absence of bisereal *Heterohelix* spp. and ornate keeled forms is indicative of the Early Cretaceous (Caron et. al., 1985; Bralower et al., 1993).

Palynology

Palynomorphs were found in the lowermost sediment cores. Sample 183-1136A-10R-CC definitely represents a marine environment, possibly from shallow water, close to shore. The kerogen is dominantly of marine origin, composed of amorphous organic matter and more than 90% dinoflagellate cysts.

The dinoflagellate flora are diverse, well preserved, and contain the genera *Oligosphaeridium, Litosphaeridium, Trichodinium, Spiniferites, Gardodinium,* and *Pseudoceratium*. According to Williams (1993), the species *Litosphaeridium siphonophorum*, identified in this sample, is a good index fossil for a mid- to late Albian age. Another taxon, *Pseudoceratium exquisitum*, also indicates a mid- to late Albian age. We also found a few smooth, thin-walled trilete spores, which are not age diagnostic but indicate a terrestrial influence.

Sample 183-1136A-14R-CC, from the terminal sediment core, also contains a marine flora, but the environment represents a stronger terrestrial influence than in the previous sample. The terrestrial influence is reflected by diverse spores with various wall shapes and appendices; the material also contains fungal spores and *Vitrisporites* sp., a saccate pteridosperm pollen. Among a rich flora of dinoflagellate cysts, we also found organic foraminiferal remains (test linings).

PHYSICAL VOLCANOLOGY

Introduction

The volcanic section at Site 1136 consists of three sedimentary lithologies with volcanic components (Units III, IV, and V) (Table T5) overlying three lava flows (Units 1, 2, and 3) (Table T6). Unit III is a very light brown foraminifer-bearing calcareous ooze with <5% disseminated palagonitized basaltic glass shards. Unit IV is a brown zeolitic calcareous volcanic clayey sand, which contains 10%–15% palagonitized basaltic glass. Unit V is a dark greenish gray carbonate-bearing zeolitic silty clay with <5% palagonitized basaltic glass, but with abundant authigenic clinoptilolite and heulandite. The three underlying lavas are of

T5. Summary of volcaniclastic components, p. 86.

T6. Location of three lava flow units in Hole 1136A, p. 87.

tholeiitic composition, and all are sparsely to moderately phyric basalts containing phenocrysts of plagioclase, clinopyroxene, and olivine. We have identified flow units on the basis of their internal textures, internal vesicle distribution patterns, and contact relationships. Volcaniclastic sediments immediately overlying the lavas were deposited at 105–107 Ma (see "Biostratigraphy," p. 6).

Foraminifer-Bearing Calcareous Ooze—Unit III

The lowermost few meters of Unit III (Core 183-1136A-9R) contain <5% disseminated silt-sized palagonitized basaltic glass shards. The abundance of shards decreases upward from the base of the unit. Shards are dominantly oblate to tabular, but blocky and equant shapes are also common. There is little evidence of rounding, and shards have conchoidal and stepped surfaces. No microcrystallites or vesicles were observed; however, shards are small (<0.3 mm). The glass ranges from pale golden brown or dark brown to dark red. Some shards have a green rim, a few micrometers wide, of a more crystalline phase, which we interpret to be an iron-rich smectite clay mineral (nontronite) after palagonite. This observation is supported by XRD analysis of similar glassy material from lower in the stratigraphic section (Core 183-1136A-10R). A few shards show an internal polygonal (jigsaw fit) fracture texture that is consistent with quenching of glass in water.

Brown Zeolitic Calcareous Volcanic Clayey Sand—Unit IV

The brown color of the volcanic clayey sand interval (Core 183-1136A-10R) is attributed to the 10%–15% silt to sand-sized yellow-brown palagonitized glass component. Texturally, the sand is composed of silt-sized aggregates of zeolites, calcareous microfossils, and volcanic shards forming a matrix enclosing sands dominated by palagonitized volcanic glass. Glass shards are angular to subrounded, equant, and blocky with conchoidal and stepped surfaces. We observed microcrystallites or vesicles in these shards. Some shards have green nontronite clay mineral rims.

A reverse graded interval at the top of Section 183-1136A-10R-1, 0–25 cm, shows a transition from medium to fine sand. The lower part of Section 183-1136A-10R-1, 25–87 cm, is fine sand and is internally massive (Fig. F6). Four subrounded centimeter-sized basaltic pebbles are distributed in this interval.

The clast-to-matrix ratio of the clayey-sand is ~70% sand and 30% silt and clay. The sand-sized component is dominated by palagonitized basaltic glass fragments with scattered opaque grains (10%–15%), authigenic glauconite grains, which are commonly casts of foraminifer tests (<5%), and calcareous microfossils (5%–10%). The silt- and clay-sized fraction is dominated by the zeolites clinoptilolite and heulandite (60%–70%), palagonitized basaltic glass shards (5%–10%), and a mixture of opaque grains, glauconite casts, and calcareous microfossils (10%–20%). The rounding of enclosed clasts and mixed nature of the sediment suggests that the clayey sand is epiclastic.

One piece of brown and white silicified mafic volcanic breccia is preserved at the base of Unit IV (Section 183-1136A-10R-1, 87–92 cm) (Fig. F6). Petrographic observations show that clasts in the breccia are internally brecciated. Domains that were once glassy are now replaced by opaline silica and sheaves of chalcedony, which are stained with iron

F6. Color close-up photograph of interval 183-1136A-10R-1, 80–90 cm, p. 40.

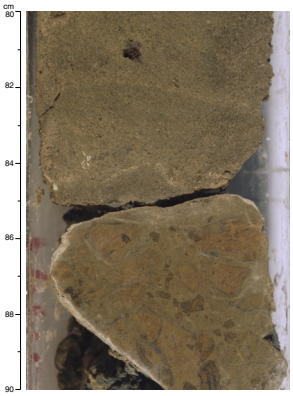

oxide (hematite) and oxyhydroxide (goethite). Late-stage quartz veins further disrupt the silicified material. Silicification of sediments rich in volcanic glass may be caused by hydrothermal alteration after emplacement.

Carbonate-Bearing Zeolitic Silty Clay—Unit V

The gray-colored zeolitic silty-clay in Cores 183-1136A-11R through 14R does not contain a high proportion of palagonitized volcanic glass (<5%) and is principally composed of silt-sized aggregates of clay-sized zeolites and biogenic carbonate (fossil fragments) (see "Lithostratigraphy," p. 3). In the marine environment, zeolites commonly form in situ in the presence of altered volcanic glass. Fine-grained well-formed crystals of authigenic clinoptilolite and heulandite are extremely abundant in Unit V, suggesting a greater proportion of volcanic glass in these fine-grained sediments when they were originally deposited.

In the lower part of the section, especially Core 183-1136A-14R, bivalve shell material and other fossil detritus are mixed with the volcaniclastic sediments, indicating reworking. An articulated bivalve implies that reworking was relatively gentle and that the sediment mixture has not been transported far. In Core 183-1136A-14R green iron-rich clay (nontronite and saponite) and mica (celadonite) are present in halos around fossil fragments, in permeable silt layers, and along fractures (Fig. F7).

F7. Color close-up photograph of interval 183-1136A-14R-1, 97–115 cm, p. 41.

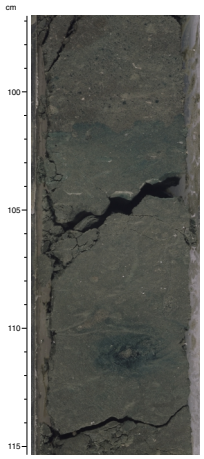

Discussion

Foraminifer-Bearing Calcareous Ooze—Unit III

We made seven principal observations about the palagonitized volcanic glass and its distribution in the calcareous ooze in Core 183-1136A-9R: (1) the glass is variably oxidized, (2) glass shards retain angular to subangular shapes, (3) glass shards do not have vesicles or microcrystallites, (4) there is more glassy material closer to the base of the unit, (5) glass shards are almost wholly palagonitized, (6) some shards have clay mineral (nontronite) rims, and (7) some have internal polygonal fractures.

The proposed mechanism for distributing these shards into accumulating calcareous microfossil-rich sediment is that flow resedimentation elutriated fine-grained particles from mafic volcanic sediments forming a cloud of suspended material above the flow. These fine particles may be transported for short distances in the water column and will eventually settle on adjacent sediment. This mechanism is supported by the identification of flow resedimented volcanic clayey sands in Core 183-1136A-10R. Angular to subangular shards imply little abrasion during transport.

Whether the glassy material is originally derived from a subaerial or subaqueous environment is equivocal. The variation in extent of oxidation of the shards suggests subaerial exposure, but the lack of preserved vesicles, equant blocky shard shapes, and internal polygonal fracturing of grains are consistent with fragmentation during subaqueous quenching. The glass may have more than one origin in epiclastic sediments.

Devitrification of volcanic glass commences when shards start to cool, and immersion in seawater enhances the process of palagonitization and ultimately the formation of more crystalline phyllosilicate

minerals. This process imparts the yellow-brown color to the preserved glass shards and explains the green nontronite rims on some shards.

Brown Zeolitic Calcareous Volcanic Clayey Sand—Unit IV

The brown zeolitic calcareous volcanic clayey sand has a mixture of grain types, including marine microfossils indicating deposition in a marine environment. Absence of lamination in most of the clayey sand suggests limited traction during deposition, implying formation either by rapid deposition from suspension or deposition from a highly concentrated sediment flow. The preferred mechanism for emplacement is as a subaqueously deposited mass flow. The upper reverse-graded bed may have been formed during waning of flow when there was more grain-grain contact.

The variation in degrees of oxidation of the shards and the brown color of the silicified mafic volcanic breccia suggests subaerial exposure of the glassy material from which the volcanic clayey sand and breccia were derived; however, equant blocky shards in the clayey sand are consistent with interaction with water at the time of formation. A range in clast shape from angular to subrounded implies that some grains have been abraded before or during transport. Incorporation of a few subrounded basaltic pebbles supports this observation.

Euhedral tabular to prismatic heulandite and clinoptilolite are abundant in the clay-sized fraction and appear to have precipitated in situ. If clay-sized zeolites form at the expense of sand-sized basaltic glass shards similar to those preserved in Unit IV, the material initially deposited may have been a fine sand. Iron from altered basaltic volcanic glass and potassium from seawater contribute to the formation of authigenic glauconite.

Carbonate-Bearing Zeolitic Silty Clay—Unit V

Fine grained silty clay in Cores 183-1136A-11R through 14R suggests a quiet environment of deposition. Shallow marine fauna in Core 183-1136A-14R, including an articulated mollusk, implies deposition in, or reworking from, a shallow marine environment. Unit V is dominated by clay-sized euhedral calcium and potassium bearing zeolite minerals. Authigenic clinoptilolite and heulandite form in the marine environment when the activity of silica and of the alkali cations are high and pH in the pore fluids is low. Celadonite and iron-bearing smectite clay minerals (nontronite and saponite) in veins, pore spaces, and halos around fossil fragments or burrows suggest postdepositional alteration, possibly at elevated temperatures (Fig. F7) (see "Lithostratigraphy," p. 3, and "Alteration and Weathering," p. 20).

Environment of Emplacement of Epiclastic Volcanic Sediments

Unit III was deposited in a midbathyal to bathyal marine environment. Unit IV was reworked, probably into a deep neritic to midbathyal marine environment. Unit V was deposited in a shallow neritic environment, below wave base (see "Lithostratigraphy," p. 3; Table T3). It appears that a progressive increase in water depth with time is reflected in the epiclastic succession and overlying calcareous sediments. This corresponds with a decreasing volcanic signature in the sediments with increasing water depth. Basaltic volcanic components in the epiclastic

sediments at this site may be genetically associated with the effusive volcanic activity immediately preceding their deposition.

Lava Flows

In Cores 183-1136A-15R through 19R, we recovered basalt from three separate lava flows (Fig. F8). In this section we focus on physical structures preserved in the core. Their petrography and geochemistry are described in "Igneous Petrology," p. 17. Table T6 lists the recorded and estimated original thickness of the flows.

Unit 1

The upper portion of the first flow is highly altered (see "Alteration and Weathering," p. 20), and no vesicular flow top material was recovered. However, drillers noted a distinct drop in the drilling rate at 133 mbsf (see "Operations," p. 2). Three thin, subplanar, vesicular regions are present in Core 183-1136A-15R-1 at 49, 98, and 128 cm (see Fig. F8 for vertical distribution and Fig. F9 for one example). These regions contain up to 20 vol% elongate, angular vesicles ranging from 0.5 to 4 mm in diameter. The petrographic texture of the groundmass crystals and bulk composition of the lava changes distinctly in these regions (see "Igneous Petrology," p. 17). Another discrete vesicular patch, at interval 183-1136A-15R-2, 10–15 cm, is more subvertical. The vesicles inside this patch are similar to those in the subplanar regions, but are slightly more rounded in shape. The remainder of the lava has 0.5%–0.1% spherical vesicles with 1–5 mm diameter.

Vesicularity gradually increases near the base of the flow, changing from 0.1% in interval 183-1136A-16R-2, 0–80 cm, to 10% in interval 183-1136A-16R-2, 135–152 cm. These vesicles are moderately to highly spherical and rounded and are not associated with a groundmass with distinct petrographic texture. However, in interval 183-1136A-16R-2, 135–145 cm, a second population of vesicles appears in the form of one-vesicle-thick wispy bands. These are very small (diameter = <0.3 mm) and angular.

Unit 2

The first recovery of the second lava flow is in Core 183-1136A-16R-2, 0 cm, and the flow extends to almost the base of Core 183-1136A-19R. We used several macroscopic criteria to distinguish Units 1 and 2, and this division has been confirmed by thin-section examination (see "Igneous Petrology," p. 17). The macroscopic criteria used in hand sample are discussed in detail in the interpretive part of this section (see "Distinction of Units 1 and 2," p. 16).

Most of the lava is relatively dense, containing 0.1–0.5 vol% spherical vesicles 1–5 mm in diameter. Subplanar vesicular zones similar to those in Unit 1 are scattered through most of Unit 2 but are most common in the upper parts of Cores 183-1136A-17R, 18R, and 19R. Generally, these vesicular zones become less common and thinner deeper in the flow (Fig. F8). Examination of the individual pieces indicates that the core preferentially split along these vesicular zones. Another important observation is that most of the subplanar vesicular zones and elongate vesicles in Section 183-1136A-16R-2 and Core 183-1136A-17R dip at 40°–60°. A 1.5-cm "megavesicle" is present in Section 183-1136A-17R-1, 70 cm.

F8. Lava-flow recovery and interpretive cross section, p. 42.

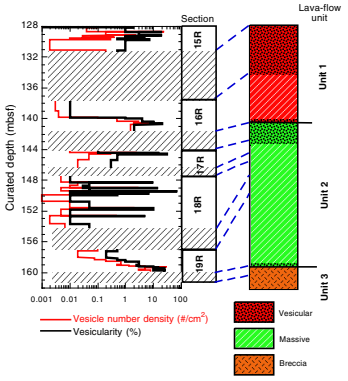

F9. Close-up photograph of interval 183-1136A-15R-2, 120–135 cm, p. 43.

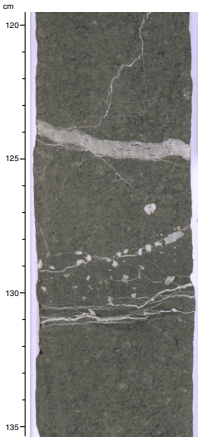

In Section 183-1136A-19R-2, vesicularity gradually increases from 1% from 0–16 cm to 10%–15% from 80–93 cm (Fig. F8). The mean vesicle size decreases downward over this same distance, but the number density of vesicles increases strongly (from <0.01/cm^2 to 30/cm^2), producing a net increase in vesicularity. The lowermost 2 to 4 cm of the above described region also has a very fine grained groundmass. The frequency and degree of fracturing marginally increases in this same region.

Unit 3

The volcanic breccia recovered at the base of Hole 1136A in the interval 183-1136A-19R-2, 93–149 cm, is the third lava unit. Clasts range from 1 cm to larger than the core diameter (7 cm). These clasts have irregular shapes with moderate sphericity and are subangular to rounded with fluidal margins in places (Fig. F10). However, no signs of plastic deformation are observed. Vesiculation is variable, but generally 10–15 vol% with nonspherical, angular vesicles more prevalent in the upper 10 cm. In places, clasts are in close contact and could be agglutinated, but surfaces adjacent to void spaces have irregular apophyses and protrusions. Void spaces are infilled by a dark gray-green clay-bearing material, most likely dominated by Fe-rich smectite clay minerals (saponite and nontronite) formed after volcanic glass. No sedimentary structures are preserved in the infilling material. The pieces of lava are held together by a matrix of dark-colored smectite clays, which are likely to be the product of altering of fine-grained volcanic glass.

F10. Close-up photograph of interval 183-1136A-19R-2, 80–120 cm, p. 44.

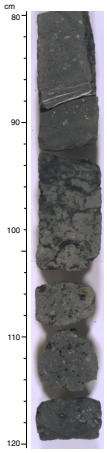

Interpretation of Lava Flows

In discussing our interpretations of features within the lavas, we proceed from smaller to the larger features. Correspondingly, there are increasing levels of interpretation and decreasing levels of certainty.

Vesicles

Most lava recovered from Hole 1136A consists of dense, almost nonvesicular lava typical of the massive interior of inflated or ponded lavas. The subplanar vesicular zones with associated distinct petrographic groundmass appear to be identical to horizontal vesicle sheets (HVSs) exposed in subaerial basalt flows, but the 5- to 7-cm width of the core is insufficient to define sheets. The subvertical vesicular zone at interval 183-1136A-15R-2, 10–15 cm, is probably a vesicle cylinder. Such features are usually found in the massive interiors of flows, and HVSs, in particular, are typically concentrated near the top of the massive interior. Megavesicles, such as observed at Section 183-1136A-17R-1, 70 cm, also indicate the upper part of the massive interior. From these vesicle features, we conclude that most recovered rock from Units 1 and 2 is from the massive interiors of inflated or ponded flows.

The other key vesicle feature is the increase in vesicularity toward the bases of both Units 1 and 2 (Fig. F11). These profiles are similar to the bases of inflated pahoehoe flows in the Columbia River flood basalt province (L. Keszthelyi and Th. Thordarson, unpubl. data). The thin zone with a high density of small vesicles is the chilled base of Unit 2. We interpret the wispy features in interval 183-1136A-16R-2, 0–80 cm, to be differentiated material (mesostatis) just starting to segregate from the lava when it was frozen in place. The trapping of these wispy segre-

F11. Vesicle distribution at the base of basement Units 1 and 2, p. 45.

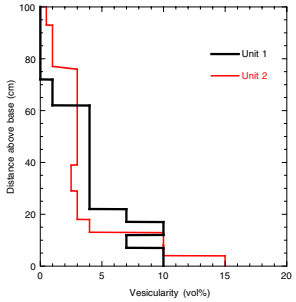

gation veins by the cooling front and the increasing vesicularity strongly suggest that the base of Unit 1 is within a few centimeters of Sample 183-1136A-16R-2, 145 cm. However, the actual chill margin was not recovered.

Vesicularity and vesicle number density correlate closely (Fig. F8). Vesicle size and vesicularity also generally correlate, but some of the most interesting vesicle features do not. In particular, the chilled margin at the base of Unit 2 has high vesicularity but very small vesicles.

Distinction of Units 1 and 2

We initially separated Units 1 and 2 on the basis of vesicle structures. Although the vesicular base of Unit 1 was a good indicator, it is possible to confuse vesicular bases with horizontal vesicle zones, which can form in the upper vesicular crust of large inflated pahoehoe flows (see "Physical Volcanology," p. 16, in the "Explanatory Notes" chapter). The most convincing macroscopic evidence that Unit 1 and 2 are separate lava flows comes from the orientation of HVSs and other usually subhorizontal features. Within Unit 1, these features dip about 20°, but in the upper part of Unit 2 they dip 40°–60°. In the lower part of Unit 2, they again dip ~20°. Dip of HVSs should not vary like this deep within a single flow. See "Structural Geology," p. 22, for a more detailed description of these dipping features and their interpretation. As noted earlier, the igneous petrology confirms that Units 1 and 2 are different lavas (see "Igneous Petrology," p. 17).

Formation of Unit 3 (Volcanic Breccia)

The volcanic breccia below the chilled base of Unit 2 does not fit any textbook examples. The cauliflower-like clasts are not the typical jagged, spinose aa clinker, nor are they like Hawaiian slab pahoehoe. No evidence, such as long stretched vesicles, was observed that would suggest the recovered lava clasts were extensively distorted while in a plastic state. The rounding of the clasts suggests some movement and/or reworking. The individual clasts are not highly fractured as is typical of hyaloclastites or peperites.

We interpret the clay matrix between the clasts as altered granulated or pulverized glassy volcanic silt and sand. Such material is present in quantity in quench fragmented hyaloclastitic rubble and in subaerial aa flow tops.

All that we can confidently conclude is that Unit 3 is a part of a disrupted flow top. Although similar rubbly flow tops are found in the Columbia River Basalts and Iceland (L. Keszthelyi, unpubl. data; Th. Thordarson, unpubl. data), the interpretation of these transitional lava types with no Hawaiian analog is problematic.

Lava Flow Thicknesses and Core Recovery

Based on our interpretation of the vertical distribution of vesicles and study of inflated flows elsewhere, it is possible to make tentative conclusions about original flow thicknesses (Table T6) and which portions of the core were not recovered. This is shown in diagram form in Figure F8. The general rule used in determining original flow thicknesses is that the massive interior of inflated flows typically makes up 40%–60% of the total flow thickness. The 6.23 m of recovered massive core from Unit 1 and ~13 m from Unit 2 suggests total original flow

thicknesses of ~12 and ~25 m, respectively. Correcting for the possible ~20° local dip (Fig. F36; see "Structural Geology," p. 22) lowers these values to 11 and 23 m, which is well within the errors of this crude estimate. There is insufficient unrecovered core to accommodate the >20 m estimated thickness of Unit 2. The vesicular flow top would be thinner in proportion to the massive interior if the flow was emplaced relatively rapidly for an inflated flow. Alternatively, there might have been sufficient time between the emplacement of Units 1 and 2 for significant erosion. However, the most likely explanation, given the highly tilted HVSs in the top of Unit 2, is that there is significant topography to the top of Unit 2. Topography of 3–5 m is very common on inflated sheet flows (e.g., Self et al., 1997). In contrast, there is sufficient nonrecovery to accommodate the full estimated thickness of Unit 1, if we assume that the contact felt by the drillers at 133 mbsf represented a reduction in alteration and vesicularity, rather than the very top of the flow. All that can be concluded about the thickness of Unit 3 is that it should be >1 m and is probably much greater.

Style of Emplacement

As noted above, the observed internal structures and flow thicknesses are very similar to continental flood basalt lava flows interpreted to have been emplaced as inflated pahoehoe sheet flows (e.g., Self et al., 1997). Flows 10–20 m thick are very difficult to produce on slopes >1°, unless they are confined by topography, so it is likely that these flows were originally emplaced on gentle slopes over a period of several months. The vesicularity and morphology of the recovered lava is consistent with emplacement in a subaerial environment.

IGNEOUS PETROLOGY AND GEOCHEMISTRY

Lithology

In this section we describe the primary texture, mineralogy, and geochemistry of the three basaltic units at Site 1136 (Fig. F12). Volcanic structures are described in "Physical Volcanology," p. 10, and secondary mineralogy in "Alteration and Weathering," p. 20.

Unit 1 extends from 128.1 to 140.6 mbsf and comprises the lower part of a massive flow. The base of this unit is oxidized and finer grained than the interior and contains ~10% clay-filled vesicles. The uppermost and lowermost recovered parts of Unit 2, which continues to 159.3 mbsf, are fine grained with relatively high abundances of vesicles. This unit comprises the massive interior and most of the base of a ~18-m-thick flow. From Unit 3, the lowermost unit, only 53 cm of vesicular breccia was recovered. This unit extends to the base of the hole at 161.4 mbsf.

Petrography and Primary Mineralogy

All lavas are sparsely to moderately phyric basalts containing phenocrysts of plagioclase ($An_{65–80}$) with lesser amounts of clinopyroxene and olivine, in an intersertal to granular or intergranular groundmass consisting of plagioclase ($An_{55–65}$), clinopyroxene, titanomagnetite, and variable proportions of altered glass (Fig. F13). The flow interiors are largely crystalline, whereas samples from marginal zones or from vesi-

F12. Interpretative summary of the lithology and abundances of phenocryst minerals in the three basaltic flows sampled in Cores 183-1136A-15R through 19R, p. 46.

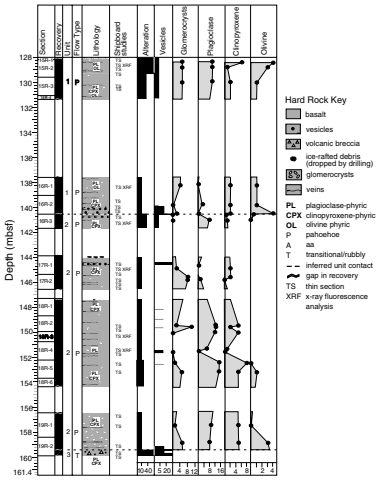

F13. Typical texture of a basalt from Hole 1136A, p. 47.

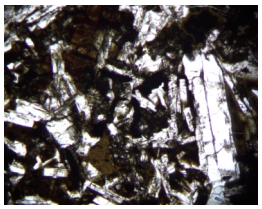

cle-rich segregations contain a higher proportion of altered glass. The extent of alteration varies from complete in the breccia of Unit 3 to slight in the massive lava in the lower part of Unit 2. In this region, plagioclase and clinopyroxene are well preserved, and secondary minerals are found only in altered glass and within vesicles and fractures.

The igneous mineralogy of the three lava flows is similar. The only significant differences are variations in the proportion of the phenocryst phases. Olivine is a persistent phenocryst mineral throughout Unit 1 but is absent from the interior of Unit 2, which contains a higher proportion of phenocryst clinopyroxene (Fig. F12). In Unit 3 the mineralogy is difficult to establish because of the severe alteration and very fine grain size of the brecciated flow top, but one fragment consists of glomerophyric basalt similar to that in Units 1 and 2.

Phenocrysts are found in three forms: as isolated grains, as loose glomeroporphyritic clusters made up of euhedral grains, and as compact, dense intergrowths of grains with diverse habits. Plagioclase is the dominant phenocryst mineral, accompanied in some cases by clinopyroxene or olivine. The loose clusters enclose abundant groundmass material between the aggregated phenocrysts and resemble typical glomerocrysts in basaltic lavas, but the morphology of the dense intergrowths and their constituent crystals is unusual (Figs. F14, F15, F16, F17). The intergrowths are up to 12 mm across and have angular to subrounded shapes (Fig. F14). Larger plagioclase grains commonly display fine oscillatory zoning and corroded cores and contain abundant, small (10–50 µm) glass inclusions (Figs. F14, F15). Also included within large plagioclase grains are small (0.5–1 mm) rounded grains of untwinned plagioclase (Fig. F16). Some intergrowths are surrounded by a thin (100–200 µm) discontinuous plagioclase rim (Fig. F17). The shape of the larger grains and the form of the oscillatory zoning (Fig. F14) indicate that these grains grew radially outward from the center of the cluster. This feature, in particular, suggests that the intergrowths are glomeroporphyritic clusters that formed during the evolution of the magma. We do not know why the grains in these clusters grew together to form a compact mass while those of the other type of glomeroporphyritic cluster remained loosely packed.

Small (~1 cm) subangular microgabbro xenoliths are present in the lower part of Unit 2 (Fig. F18). They mainly consist of medium-grained plagioclase and clinopyroxene with minor olivine. Altered glass forms films between mineral grains and has accumulated at interstices between plagioclase and clinopyroxene grains, which also contain abundant small glass inclusions. These textures may have resulted from remelting of xenoliths after incorporation in the basalt. The corroded plagioclase grains in intergrowths resemble those in these xenoliths and could have come from the same source.

Vesicle-rich segregations form 1- to 2-cm-wide bands or patches in Units 1 and 2. They are commonly horizontal (rarely subvertical) and contain 10%–30% vesicles in a fine- to medium-grained, glass-rich matrix (Figs. F9, F19). Neither large phenocrysts nor glomerocrysts are present in the matrix of these bands, which is coarser grained and richer in titanomagnetite and glass than the surrounding rock. Some grains of plagioclase and many grains of titanomagnetite have skeletal habits indicative of rapid crystallization (Fig. F20). The contacts of the vesicle-rich segregations have several notable features. They are sharp but lack textures such as broken crystals or chilling of one unit against the other that indicate intrusion of magma into solidified rock, and plagioclase crystals have nucleated at the contact and grown into the seg-

F14. Compact glomeroporphyritic intergrowth, p. 48.

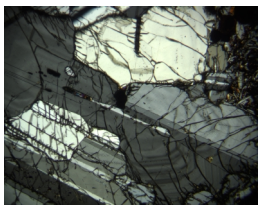

F15. Plagioclase grains with abundant glass inclusions, p. 49.

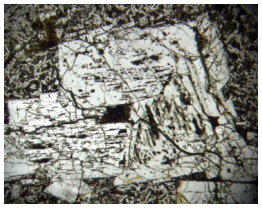

F16. Plagioclase grains included in larger plagioclase grains in a glomeroporphyritic intergrowth, p. 50.

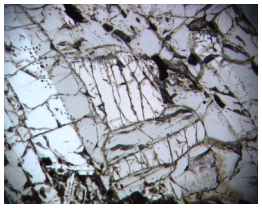

F17. Discontinuous plagioclase rim around a compact glomeroporphyritic intergrowth, p. 51.

F18. Microgabbro xenolith, p. 52.

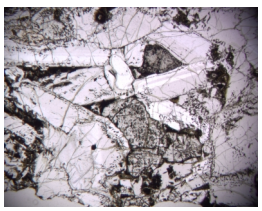

regation (Fig. F21). These observations suggest that the segregations formed when late-stage, volatile-rich interstitial liquids migrated and accumulated within the cooling flow.

Major and Trace Element Compositions

We list XRF analyses of major and trace elements in six samples in Table T7. Four samples from the least-altered (loss on ignition = 0.9%–2.1%) and massive portions of Units 1 and 2 have very similar compositions. Their SiO_2 contents vary from 50 to 51 wt%, MgO from 6.4 to 6.7 wt%, and TiO_2 from 1.60 to 1.76 wt% (Table T7; Figs. F22, F23). The flows are quartz normative tholeiitic basalts with relatively low MgO and Ni contents and low Mg#, similar to basement rocks from other parts of the Kerguelen Plateau (Fig. F23). Mantle-normalized trace element patterns of the least-altered rocks are almost flat, with only slight enrichment of the more incompatible immobile trace elements (Nb and Ce) relative to the more compatible elements (Ti and Y) (Fig. F24).

Trace element abundances in the two analyzed flows differ slightly; the less altered sample from Unit 1 has marginally lower Ti, Nb, Zr, Y, and Ce, distinctly lower V, and higher Cr than the massive samples from Unit 2 (Fig. F25; Table T7).

Two samples are mineralogically and compositionally distinct. In Sample 183-1136A-15R-2 (Piece 2, 69–71 cm) in Unit 1, most of the primary phases have been replaced by secondary minerals (Fig. F12). This sample was analyzed to assess the chemical effects of alteration. As shown in Figures F23 and F25 and Table T7, the contents of MgO and CaO are slightly lower, and Fe_2O_3* (total iron as Fe_2O_3) is slightly higher, than in other samples. However, concentrations of the mobile elements K and Rb are 3.5 and 5.5 times greater than in the less-altered sample from Unit 1, and the Ce content is ~50% lower (Table T7; Fig. F25).

Sample 183-1136A-18R-4 (Piece 2, 89–92 cm) from a vesicle-rich segregation in Unit 2, has slightly lower SiO_2, Al_2O_3, MgO, CaO, Ce, and V contents, distinctly lower Ni and Cr, and markedly higher Fe_2O_3*, TiO_2, P_2O_5, Nb, Zr, and Y contents than other Unit 2 samples (Table T7; Figs. F23, F25). In thin section, the segregations are seen to be relatively rich in titanomagnetite and goethite, which, together with clay minerals, replace domains of altered glass. The low contents of Ni, Cr, and particularly V, elements that are compatible with Fe-Ti oxides, indicate that accumulation of titanomagnetite could not have been responsible for the high Fe_2O_3* and TiO_2 contents. Instead, we propose that the vesicle-rich segregations formed from highly evolved interstitial liquids whose high Fe_2O_3*, TiO_2, P_2O_5, Nb, Zr, and Y contents resulted from fractionation of olivine, clinopyroxene, and plagioclase. A problem with this explanation is the relatively low abundance of Ce, an element incompatible in the crystallizing assemblage that should have been relatively enriched in the segregated liquids. Resolution of this paradox must await shore-based analysis of the rare-earth elements.

Comparison with Other Sites

We compare the compositions of basalts from Site 1136 with those of basalts drilled or dredged in other parts of the Kerguelen Plateau in Figures F23, F26, and F27. The least-altered samples from Site 1136 have compositions within the range of previously recovered basement basalts and distinct from those of the younger, more alkaline rocks on

F19. Groundmass of a subhorizontal segregation, p. 53.

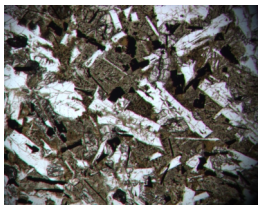

F20. Detail of titanomagnetite grains in the matrix of a segregation, p. 54.

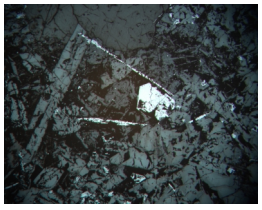

F21. Margin of a segregation showing plagioclase crystals, p. 55.

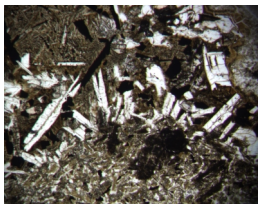

T7. Major and trace element data, p. 88.

F22. Diagram of SiO_2 vs. total alkali abundance, p. 56.

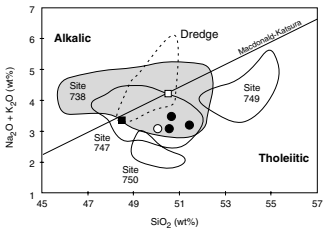

Heard Island and the Kerguelen Archipelago (see **"Previous Sampling of Igneous Basement: Ages and Geochemical Characteristics,"** p. 5, and Fig. **F8,** p. 58, both in the "Leg 183 Summary" chapter). Abundances of incompatible elements in Site 1136 basalts are intermediate between those basalts from Site 750 and the more enriched samples from Sites 747 and 738 (Fig. **F26**). They most closely resemble the low-Al_2O_3 basalts from Site 749 (Figs. **F23, F26, F27**).

Lack of Chemical Evidence of a Continental Crust Component

Two elements analyzed with shipboard XRF are particularly useful for identifying a continental crust component in plateau basalts. The concentrations of Nb, and to a lesser extent Ti, are relatively low in continental crust, compared to concentrations of other elements with similar geochemical behavior. A continental component is therefore reflected in low ratios of Nb/Ce, Nb/Zr, and high Zr/Ti, or as relative depletions (troughs) in mantle-normalized trace element patterns. Such features have been used, in conjunction with isotope data, to identify a continental component in the Bunbury and Rajmahal continental flood basalts and in basalts from Site 738, which forms part of the SKP (see **"Previous Sampling of Igneous Basement: Ages and Geochemical Characteristics,"** p. 5, in the "Leg 183 Summary" chapter). Figure **F27** shows the three ratios, plotted against Zr/Y and Zr content. Basalts from Site 738, whose isotope compositions indicate a continental crust component, have low values of $(Nb/Ce)_N$ and $(Nb/Zr)_N$ and high values of $(Zr/Ti)_N$. Basalts from Site 1136 show no evidence of such a component. Specifically, they are not relatively depleted in Nb or Ti (Fig. **F24**), and they do not overlap with crust-contaminated basalts from Site 738 in Figure **F27.** On the basis of shipboard data, the source of Site 1136 basalts does not contain a continental component, and their magmas did not interact significantly with continental lithosphere during their emplacement.

ALTERATION AND WEATHERING

Weakly indurated sediments containing abundant volcanically derived materials are present in Cores 183-1136A-10R to 15R-1, 7 cm (79.90–128.08 mbsf). Postdepositional processes strongly affected these silty to sandy materials (see **"Lithostratigraphy,"** p. 3). Underlying these sediments are three igneous units from Cores 183-1136A-15R to 19R (128.08–161.40 mbsf), interpreted to be separate lava flows (see **"Igneous Petrology,"** p. 17, and **"Physical Volcanology,"** p. 10).

All basaltic rocks recovered from Hole 1136A are slightly to completely altered to low-temperature secondary phases that partially replace primary minerals, completely replace mesostasis, and partly to completely fill veins and vesicles. The distributions of secondary minerals recorded in the alteration and vein/structure logs (see the **"Supplementary Materials"** contents list) for Hole 1136A are shown in Figure **F28.** The most common secondary phases are clays (both Mg-saponite and celadonite), calcite, and zeolites. In general, clay minerals are abundant at all depths, whereas the abundances of calcite and zeolites exhibit more pronounced downhole variations (Fig. **F28**). In particular, calcite is more common in both veins and vesicles in the upper por-

F23. MgO variation diagrams comparing basalts from Hole 1136A with those from other parts of the Kerguelen Plateau, **p. 57.**

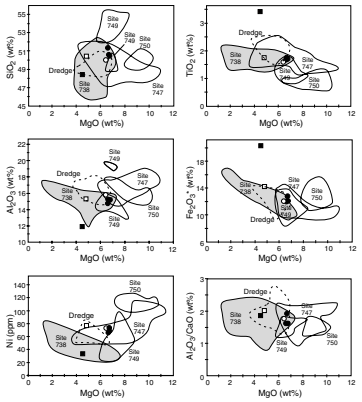

F24. Trace element contents of basalts from Site 1136, **p. 58.**

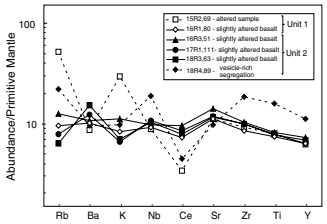

F25. Variations of major and trace element abundances, plotted against depth in Units 1 and 2, **p. 59.**

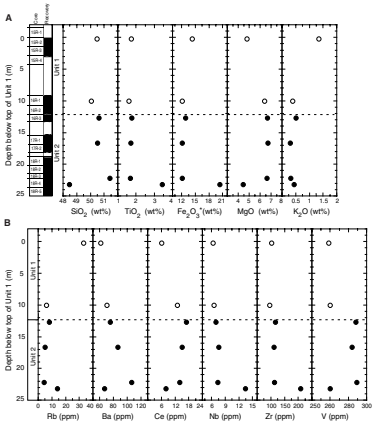

tions of Unit 1 (130–135 mbsf), near the contact between Units 1 and 2 (140–143 mbsf) and in veins near the contact between Units 2 and 3 (158–160 mbsf). Zeolites are absent or present in only minor amounts in Units 1 and 2 and are only abundant in veins and vesicles near the base of Unit 2 and in Unit 3 (Fig. F28).

The uppermost rocks from Unit 1 (e.g., Sections 183-1136A-15R-1 and 15R-2) are moderately altered and display a distinctive blue-green hue, indicative of celadonite, a potassium ferric iron mica (confirmed by XRD) (see Table T8). Alteration in these rocks is similar to that observed in the carbonate-bearing zeolitic silty clays of Unit V, which directly overlie basaltic basement (e.g., Section 183-1136A-14R-2). In the basaltic basement, celadonite ± Mg-saponite partially replace the groundmass and mesostasis and these phases, together with calcite, fill veins and vesicles. Narrow (2 to 5 mm), late-stage oxidation halos are developed around some veins. Veins have developed by both the filling of open cracks, as well as the alteration of wall rock, with thin slivers of the host basalt having been separated and replaced by celadonite ± Mg-saponite (e.g., Fig. F29). Many veins record multiple generations of mineral precipitation, brecciation, and wall-rock alteration (e.g., Figs. F29, F30). The most common paragenesis observed is clay lining veins with calcite interiors.

The dark gray interiors of Units 1 and 2 (Sections 183-1136A-15R-3, 0 cm, to 19R-2, 93 cm) are slightly to moderately altered. Finer-grained basalts have a pinkish brown color. Light to dark green clay, predominantly Mg-saponite replaces olivine ± clinopyroxene phenocrysts, as well as the mesostasis (see Table T8). Uncommon clay-filled veins display weakly developed green alteration halos. Vesicles are generally lined with dark clay minerals and filled with either lighter colored clays or calcite. Zeolites are absent or only minor constituents of either veins or vesicles from both Units 1 and 2, except from directly above the contact with Unit 3 (e.g., Sections 183-1136A-19R-1 and 19R-2), where clinoptilolite (heulandite) line the margins of both veins and vesicles.

Thin-section observations of basalts from Units 1 and 2 support the hand specimen descriptions and confirm the complete alteration of mesostasis and olivine to brown (in thin section) clay minerals with variable staining by iron oxyhydroxides. All samples display a brownish hue indicative of strongly developed groundmass alteration and oxidation. There is a ubiquitous replacement of interstitial glass and coating of most grain boundaries, cleavage traces, and fractures. Plagioclase laths in both glomerocrysts and groundmass are partially altered to clay minerals. Most groundmass and phenocrystic clinopyroxene is degraded to clay minerals, though uncommon, well-preserved clinopyroxene is present in the fresher, near holocrystalline, fine- to medium-grained basalts from the interior of Unit 2 (e.g., Sample 183-1136A-18R-5 [Piece 1B, 111 to 112 cm]). Vesicle and vein filling include celadonite, brown-green clay (Mg-saponite), calcite, and zeolites (individual zeolites were generally not distinguished in thin section).

Unit 3 comprises a highly to completely altered top of a lava flow, in which abundant glassy material and mesostasis is replaced in situ by black to dark green waxy clay, and zeolites fill wispy crosscutting veinlets and vesicles (e.g., Fig. F31).

F26. Trace element compositions of basalts from Hole 1136A, compared with those from other parts of the Kerguelen Plateau, p. 60.

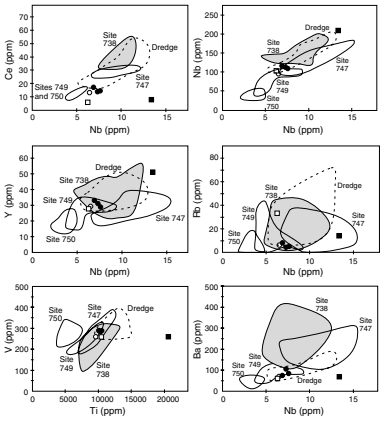

F27. Zr/Ti, Nb/Zr, and Nb/Ce ratios vs. Zr/Y ratio or Zr content, p. 61.

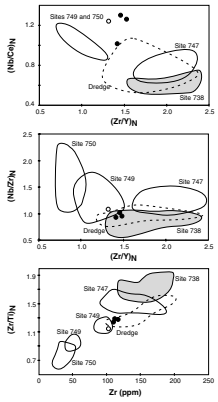

F28. Distribution and abundance of secondary minerals plotted against expanded depth, p. 62.

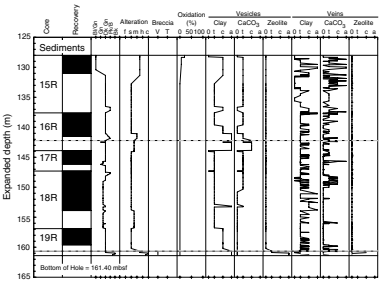

T8. Alteration minerals hosted by igneous rocks, p. 89.

STRUCTURAL GEOLOGY

Rocks from Site 1136 exhibited relatively few structural features. We observed no significant tectonic structures in sediments and sedimentary rocks that overlie the basaltic basement. We measured, and reported in the vein-structure log for this site (see the **"Supplementary Materials"** contents list), the orientation, location, and mineral filling of 315 structural features from the basaltic basement (Sections 183-1136A-15R-1 to 19R-2). Veins are the most common structural phenomena, and we present orientation information for the vast majority of veins in these cores. We also recorded the orientation of primary internal structures such as vesicle sheets coalesced into veins and wispy streaks of clay minerals replacing mesostasis. The absence of downhole logging information at this site, or a consistent structural marker plane (e.g., sedimentary bedding, magmatic/tectonic foliation) precludes reorientation of structural measurements and calculation of true-dip directions. We note, however, that the seismic reflection marking the top of basaltic crust at Site 1136 has an apparent dip of 1° (to the west) (see **"Background and Objectives,"** p. 1).

No tectonic breccias, shear zones, or ductile or cataclastic fault zones were encountered in the Hole 1136A cores. We observed only three microfaults. Two of these features are steeply dipping mineral-filled veins, which disrupt more gently dipping veins with a small (~1 to 2 cm) normal offset. The other feature is a small, steeply dipping clay vein with well-developed subhorizontal slickensides. The mineral fillings of both the displaced and offsetting veins are similar.

Veins are a common feature throughout the basaltic basement (Fig. **F32**). Although data are sparse because of limited basement penetration, veining and, in particular, carbonate veins are most abundant at the top of the basaltic section (Core 183-1136A-15R). The abundance of clay-filled veins is approximately constant with depth (less than a factor of 2 variation). The frequency distribution of the true dip of veins (Fig. **F33**) shows little discernible signal, except the hint that gently dipping veins (<30° true) are relatively more common in Unit 1. This coincides with the presence of abundant subhorizontal to gently dipping calcite-filled veins in Cores 183-1136A-15R and 16R. The number of wider, subvertical sets of conjugate veins increases near the base of Unit 2 (Cores 183-1136A-18R and 19R).

To examine possible tilting of the lava flows in response to regional or local faulting, we examined the orientation of 26 features in lava Units 1 and 2 that are interpreted to be originally subhorizontal. These features included vesicle sheets, wispy sheets of mesostasis defining a subtle foliation in the lava, and flattened vesicles. These features commonly develop with a subhorizontal, planar orientation because of flow of magma beneath a solidified upper crust. Especially in large sheet flows, the cooling front defining the base of the upper crust is generally horizontal, but exceptions can arise from significant surface topography (e.g., tumuli and inflation pits) (see **"Physical Volcanology,"** p. 16, in the "Explanatory Notes" chapter).

Inspection of the true dips of the 26 volcanic features as a function of depth in the lava flows (Fig. **F34**) leads to two postulations. First, the highly variable dip angles in the upper part of Unit 2 do not result from tectonics, and they probably reflect nearby topography in the upper surface of this flow. Second, both units consistently dip about 20°, perhaps related to faulting associated with formation of the Labuan Basin,

F29. Color close-up photograph of Sample 183-1136A-15R-2 (Piece 1B, 33–41 cm), **p. 63.**

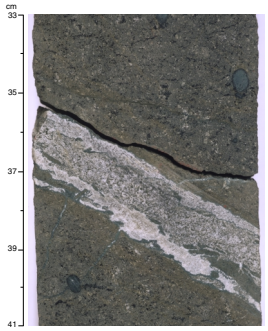

F30. Color close-up photograph of Sample 183-1136A-15R-2 (Piece 1B, 47–62 cm), **p. 64.**

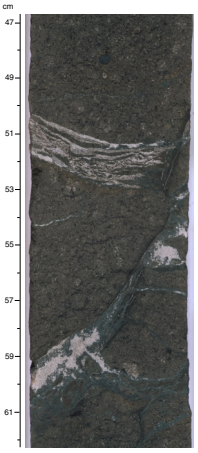

F31. Color close-up photograph of Sample 183-1136A-15R-2 (Pieces 9 to 12, 47–62 cm), **p. 65.**

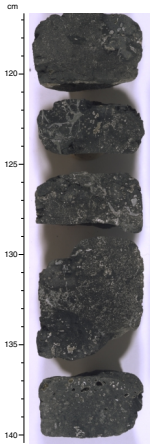

which is only 8 km to the east. However, without downhole logging data, it is not possible to confirm that all dips are in the same direction, or that they are consistent with orientation of faults seen in the seismic lines (see "Background and Objectives," p. 1).

PALEOMAGNETISM

We measured the natural remanent magnetization (NRM) of all archive halves from Hole 1136A with the pass-through cryogenic magnetometer using measurement intervals of 5 and 2.5 cm for sediment and basalt sections, respectively. After measuring the NRM, all sediment cores were demagnetized with a peak alternating field (AF) of 20 mT. Two discrete samples were taken per section and were stepwise AF demagnetized up to 60 mT. All basalt archive-half cores were stepwise AF demagnetized with a peak field of 60 mT. Discrete basalt samples were stepwise AF demagnetized in a peak field of 60 mT or thermally demagnetized in temperatures of up to 620°C. We determined the anisotropy of magnetic susceptibility (AMS) of discrete basement samples to obtain information about the magnetic fabric.

Sediments

We obtained reliable results in undisturbed cores with high recovery, and correlated normal and reversed segments with biostratigraphic zones (see "Biostratigraphy," p. 6). However, RCB cores do not provide a continuous magnetostratigraphic record as a result of core disturbance and incomplete recovery. Secondary components of remanent magnetization could be removed by AF demagnetization at 10 mT (Fig. F35A). Stable remanent magnetizations were obtained after AF demagnetization at 20 mT, especially for sediments with a higher median destructive field (MDF) (Fig. F35B). For the magnetostratigraphic study of Hole 1136A (Fig. F36), we used the data selection criteria as described in "Paleomagnetism," p. 27, in the "Explanatory Notes" chapter. The selection criteria were that (1) the intensity of remanent magnetization after AF demagnetization at 20 mT was > 2×10^{-4} A/m and hence above the noise level of the magnetometer in rough-sea conditions, (2) the inclination was > ±30°, (3) at least three consecutive values (which corresponds to a 15-cm length of split core) had the same polarity, and (4) there was no significant core disturbance. We calculated characteristic remanent magnetic directions of discrete samples using component analysis. Characteristic inclinations from discrete samples generally agree well with selected inclinations from whole-core measurements (Fig. F36).

Correlation of biostratigraphic data and polarity reversals (Fig. F36) suggests that the reversed and normal chrons in Hole 1136A are middle Eocene to Early Cretaceous in age (see "Biostratigraphy," p. 6). Both Sections 183-1136A-2R-CC (14 mbsf) and 3R-CC (23 mbsf) lie within nannofossil Subzone CP12b (see "Biostratigraphy," p. 6). This reversed polarity interval at ~15 mbsf correlates with Chron C21r. We correlated the next reversed polarity interval at ~27 mbsf to Chron C21r, based on the paleontological identifications; Section 183-1136A-CC lies within nannofossil Subzone CP12a and upper foraminifer Zone AP7 (see "Biostratigraphy," p. 6). We correlate reversed and normal polarity intervals at ~35 mbsf and between 42 and 53 mbsf to Chrons C22r and C23n, respectively, according to biostratigraphic data (see "Biostratig-

F32. Distribution of clay- and calcium carbonate-filled veins with depth, p. 66.

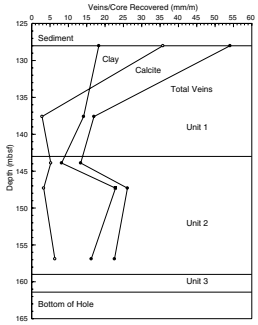

F33. Frequency distribution of the true dips of veins from basaltic host rocks, p. 67.

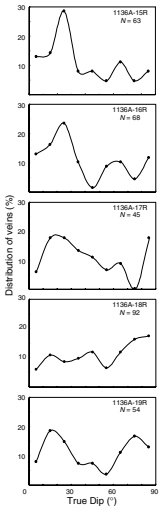

F34. Dips within flows, p. 68.

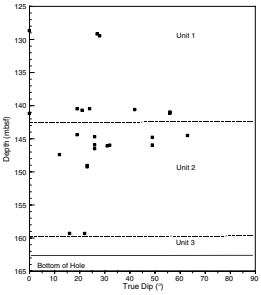

F35. AF demagnetization of discrete sediment samples, p. 69.

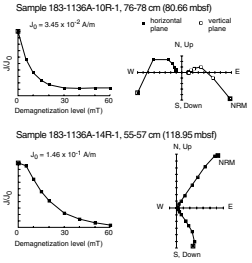

raphy," p. 6). Normal polarity sequences at ~80 and ~120 mbsf can be correlated to early Maastrichtian Chron C31r and Albian Chron C34n, respectively, according to nannofossil zoning (see "Biostratigraphy," p. 6).

A summary of NRM intensities and susceptibilities (see "Physical Properties," p. 26) for the four lithostratigraphic units (see "Lithostratigraphy," p. 3) is presented in Table T9. In the upper part of Unit II (nannofossil ooze) we observed negative susceptibilities and weak NRM intensities. Remanent magnetization was less stable, and magnetization of discrete samples collected from this part was too weak to measure reliably with the shipboard magnetometer during rough seas. We observed weak and positive susceptibilities and stronger NRM intensities in the lower part of Unit II than in the upper part. Progressive AF demagnetizations and measurements of discrete samples were successful and provided a reliable paleomagnetic record. High susceptibilities (average >2 × 10^{-4} SI units) and strong NRM intensities (average >1 × 10^{-2} A/m) were observed in Units IV and V. We obtained stable remanent magnetizations during progressive AF demagnetization experiments (Fig. F35). Stable and reliable paleomagnetic data were obtained from both half-core and discrete measurements in this interval.

Basement Rocks

We obtained a continuous record of the NRM inclination and intensity from measurements of half-core basement sections. We chose two discrete samples for thermal demagnetization and one sample for AF demagnetization from each flow unit (basement Units 1 and 2; see "Igneous Petrology," p. 17). We found negative inclinations, and hence, normal polarity in the basement rocks of Site 1136.

To observe the magnetic properties of each basement unit and to determine the variation of magnetic properties within each unit, we performed whole-core measurements of remanent magnetization and susceptibility (Fig. F37). Three different types of susceptibility measurements generally show consistent results. Anomalously low MST susceptibility values and low AMST values are commonly caused by gaps in recovery (see "Paleomagnetism," p. 27, in the "Explanatory Notes" chapter). In basement Unit 1, susceptibilities are constant except for the lower 2 m of the flow, where we observe slightly weaker susceptibilities. The average susceptibility of basement Unit 2 is almost the same as that of basement Unit 1 (Table T9). We found more significant variations in susceptibility within basement Unit 2 than in basement Unit 1. Weaker susceptibilities were observed in the lower half of this unit. The variation in susceptibility is probably caused by variations in the magnetic mineral type or variations in the content of magnetic minerals in the basement units with depth. No significant difference is observed in average NRM intensities between the two basement units. After AF demagnetization at 40 mT, we found a clear difference between the intensities of remanent magnetization of basement Units 1 and 2. NRMs of Unit 2 lose their intensity easily by AF demagnetization (Fig. F37). This is caused by differences in size of magnetic mineral and/or mineralogical differences.

Two samples from the basalt flows of Site 1136 were demagnetized with an AF of up to 60 mT. Both samples possess single-component magnetizations, as is evident from the straight lines on the Zijderveld plots (Fig. F38). We expect single-domain magnetite or titanomagnetite particles to be the magnetic carrier in these samples because of their

F36. Inclination, intensity, and susceptibility of sediments, p. 70.

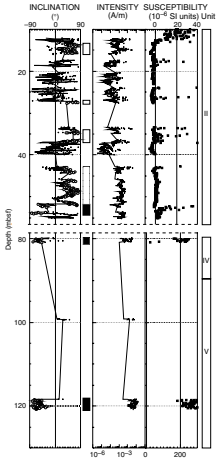

T9. Summary of NRM intensity and susceptibility, p. 90.

F37. Inclination, intensity, and susceptibility of basement rocks, p. 71.

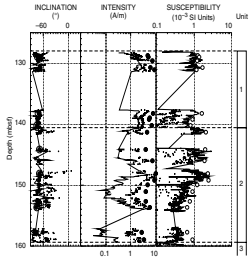

F38. AF demagnetization of a discrete basement sample, p. 72.

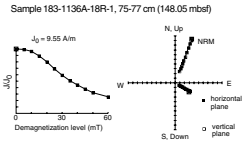

high NRM intensity (7.5 and 9.6 A/m) and high MDF (43 and 37 mT). Four samples were stepwise thermally demagnetized up to 620°C (Fig. F39). We measured the susceptibility of the samples after every heating step to detect changes of their magnetic minerals (Fig. F39). We determined an unblocking temperature of ~580°C in Samples 183-1136A-18R, 132–134 cm, and 15R-2, 116–118 cm (Fig. F39A). This temperature corresponds to the Curie temperature of magnetite or titanium-poor titanomagnetite, which we consider to be responsible for the remanent magnetization of these samples. The constant decrease in susceptibility with temperature is probably caused by a mineral change from (titano)magnetite to (titano)hematite. The decay curve of Sample 183-1136A-18R, 132–134 cm (Fig. F39B) during thermal demagnetization indicates that two magnetic phases are responsible for the remanent magnetization. Most of the magnetization was removed by ~300°C, and the small remaining magnetization disappeared by ~580°C. The low-temperature phase (300°C) is maghemite or titanomaghemite. The increase in susceptibility at 400°–500°C and the following decrease at 500°–600°C correspond to changes from (titano)maghemite to (titano)magnetite and from (titano)magnetite to (titano)hematite, respectively. Maghemite and titanomaghemite are low-temperature oxidation products of magnetite and titanomagnetite, respectively. Sample 183-1136A-17R-1, 22–24 cm, seems to contain components of both (titano)magnetite and (titano)maghemite (Fig. F39C). Titanomaghemite and titanomagnetite have been previously reported from basement basalt of the southern Kerguelen Plateau (Heider et al., 1992).

We obtained characteristic remanent magnetic directions of discrete samples using component analysis. The declinations of all samples are arbitrary because the cores were unoriented. The six samples have inclinations ranging from –69° to –76° (Table T10). For basement Units 1 and 2, we obtained mean inclinations of –74° and –70°, respectively. The small difference between these two values could be insignificant, given the limited shipboard measurements. A certain amount of interunit difference is expected from secular variation of the geomagnetic field, depending on the elapsed time between lava-flow eruptions. The average inclination of the two units is –72° and agrees with the mean inclination obtained from whole-core measurements (Fig. F37). The mean inclination of whole-core measurements is –71° and was obtained using inclinations (after AF demagnetization at 40 mT) from long igneous cores that are longer than the effective sensitivity of the pass-through magnetometer (~15 cm). The paleolatitude calculated from the mean inclination (–72°) assuming a geocentric dipole field is 56°S. Thus, the difference between the paleolatitude and the present latitude of Site 1136 (60°S) is only 4°. Previous paleomagnetic results show a difference of 13° to 16° between the present latitude and paleolatitude of basement rocks from the southern Kerguelen Plateau (Inokuchi and Heider, 1992). The difference between our results and the previous study can be explained by (1) inaccurate paleolatitude estimates caused by limited measurements, (2) secular variation of the geomagnetic field, (3) possible recent overprints of the remanent magnetization, (4) tilting of the basement units, (5) differences in age of the units measured, or (6) divergent motion of separate tectonic blocks. As there is no evidence for the last three explanations, we conclude that the inconsistent results may be caused by inadequate measurements, secular variation, and/or overprints.

From 20 discrete samples of basement Units 1 and 2, we determined the AMS using susceptibility measurements in 15 different orientations

F39. Thermal demagnetization of discrete basement samples, p. 73.

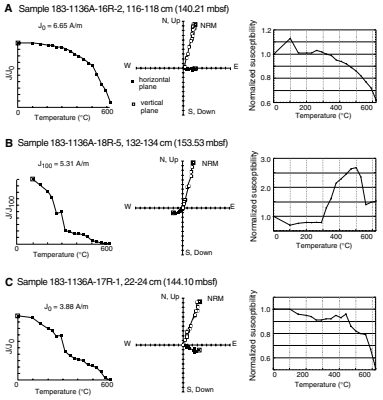

T10. Characteristic inclinations and NRM intensities of Hole 1136A basalt, p. 91.

(Fig. F40). Generally, we found only a low degree of anisotropy, with an average magnitude of 1.016. We used the three principal susceptibilities for each sample to determine the shape of the fabric. Most of the samples have a positive shape parameter, which corresponds to oblate (disk) shapes, while negative values correspond to prolate (rod) shapes. The minimum principal axes are grouped at an inclination of 90° and the maximum and intermediate directions are within a girdle 90° from the minima (Fig. F40), hence there is a predominant magnetic foliation. The foliation plane in basement rocks generally lies close to the flow plane, and the minimum susceptibility axis is perpendicular to the flow plane. The distribution of the minimum axes (Fig. F40) indicates horizontal outflow for Units 1 and 2.

F40. Anisotropy data from flow units, p. 74.

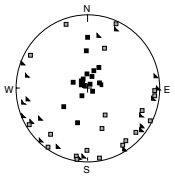

PHYSICAL PROPERTIES

Introduction

Measurements of unsplit sections of core taken at Site 1136 were taken from magnetic susceptibility, gamma-ray attenuation porosity evaluator (GRAPE) bulk density, and natural gamma radiation (NGR). We also determined thermal conductivity for sediments and basement rocks. Compressional wave velocities (V_p) were determined on the working half of the core and in discrete samples with the contact/insertion probe system. We calculated index properties from wet and dry sample masses and dry volumes.

Index Properties

We obtained index properties data (bulk density, grain density, porosity, and water content) using gravimetric methods on discrete samples from Site 1136 (Table T11; Fig. F41). Average grain densities of 2.70 g/cm³ and 2.68 g/cm³ for lithologic Unit II (early to middle Eocene foraminifer-bearing nannofossil ooze) and Unit III (mid-Campanian calcareous ooze), respectively, are virtually the same as those of lithologic Units II and III in Hole 1135A (see "Physical Properties," p. 15, in the "Site 1135" chapter). Between ~90 and ~120 mbsf, within Unit V, grain density decreases to mean value of 2.48 g/cm³. Water content and porosity are also quite uniform within Units II and III. Average porosities of 56.2% and 52.0% are present in Units II and III samples, respectively. Porosity values in Unit V increase to 65.5%.

Sediment and basalt units separate by marked differences in all index properties (Fig. F41). Porosity decreases sharply from an average of ~57% in the overlying sediments to ~16% in the basalt flows. The average grain density of 2.90 ± 0.04 g/cm³ for basaltic Unit VI is slightly less than the average grain density for basalt, 3.01 ± 0.14 g/cm³ (Johnson and Olhoeft, 1984). The slight discrepancy may be caused by less dense clays and calcite filling many of the vesicles and veins within the basalt, as well as alteration in the basaltic flows (see "Alteration and Weathering," p. 20).

T11. Index properties data, p. 92.

F41. Downhole index properties and velocities, p. 75.

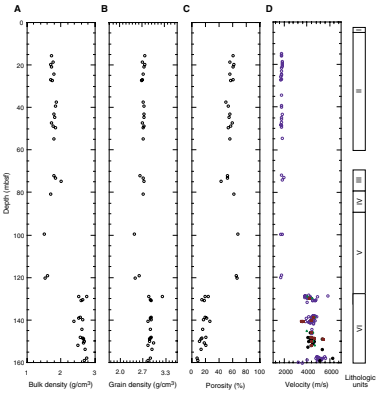

MST Measurements

GRAPE Density

Bulk densities were also estimated from whole-core GRAPE measurements taken in sections recovered from Hole 1136A (Fig. F42). In the sedimentary section, the maximum GRAPE densities are in the uppermost 40 cm in Section 183-1136A-2R-1 at a depth of ~5 mbsf, which coincides with coarse mixed volcanic sand. These mixed sediments are interpreted as mixed ice-rafted debris and ooze that were highly disturbed during coring (see "Lithostratigraphy," p. 3).

The maximum GRAPE densities give the best estimate for true bulk density of the sediment (Blum, 1997; Boyce, 1973). Maximum densities increase at the lithology boundary of the sediment and basalt units (Fig. F42C). In the sedimentary section, between 5.2 and 55.1 mbsf, the average estimated maximum density is 1.7 g/cm³. Below 70.3 mbsf, which is the boundary between lithologic Units II and III (see "Lithostratigraphy," p. 3), the estimated maximum bulk density increases to an average of 2.0 g/cm³. Between 118.4 and 120.6 mbsf, the bulk density decreases to a value of 1.8 g/cm³, corresponding to the highly fractured and altered volcanic sands in Core 183-1136A-14R. Below 128.1 mbsf, recovered cores are basalts that exhibit much higher bulk density with an estimated maximum value of 2.6 g/cm³. Comparison of the downhole maximum bulk density profile (Fig. F42C) and bulk density data obtained from discrete samples (Fig. F41A) shows that the two generally correlate, except that discrete sample data for the basalt units consistently show higher values than the GRAPE density data. The larger scatter in the GRAPE bulk density data for the basalt flows probably results from the fractured nature and narrow diameters of the cores, which consequently do not fill the core liner.

F42. Downhole profiles of whole-core measurements of magnetic susceptibility, natural gamma ray, and GRAPE bulk density, p. 76.

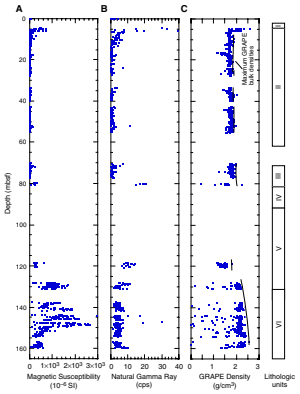

Natural Gamma Radiation

Where sufficient data were present, NGR data obtained from whole-round sections were filtered using a 5-m-wide boxcar function. As shown in Figure F42, NGR measurements on unsplit sections of Hole 1136A show local positive peaks of >20 counts at ~5, ~80, and ~150 mbsf, corresponding to the Pleistocene coarse sand, the Upper Cretaceous calcareous ooze (with minor disseminated volcanic material), and the flow top of basement Unit 2, respectively. In the rest of the section, NGR values vary little. In the sediments, the values drop from an average value of 8 to 2 cps. A local small increase at ~120 mbsf reflects the altered volcanic sand unit (Core 183-1136A-14R). In the basaltic basement (128.1–160 mbsf), NGR averages 5 cps (Fig. F42B).

Magnetic Susceptibility

We determined magnetic susceptibility on all cores from Site 1136, with whole-core sections measured at 4-cm intervals by the Bartington meter and split-half sections at 2-cm intervals by the point-susceptibility meter. The two magnetic susceptibility data sets compare well with each other. The characteristic susceptibility peaks and troughs correlate with flow boundaries, with peaks reflecting flow top and troughs corresponding to flow bottom and intervals with abundant vesicles (Fig. F43A). Detailed results are discussed in "Paleomagnetism," p. 23, in

F43. Summary of physical properties determinations in basaltic basement of Hole 1136A, p. 77.

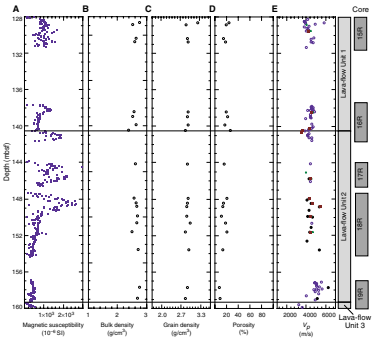

conjunction with the NRM pass-through and discrete sample measurements.

Compressional Wave Velocity

Variations in compressional wave velocity downhole commonly correlate with changes in lithology. In general, compressional wave velocity bears a direct relation to wet bulk density and grain density and is inversely related to water content and porosity. At Site 1136, we calculated compressional wave velocity from both discrete measurements on split-core sections and cut samples (Fig. F41D). Measurements were generally made in the x direction, although some discrete samples were also measured in the other two directions to investigate velocity anisotropy (Table T12). We observed no clear anisotropy trend (Fig. F43; Table T12).

T12. V_p discrete determinations, p. 93.

The compressional wave velocity data for the sedimentary sections show very little scatter (Table T12; Fig. F41D). A marked velocity contrast at a depth of 128.1 mbsf marks the boundary between the sediments and basement. Above 128.1 mbsf, compressional wave velocity are typically <1800 m/s. Within the basalt section, velocities typically exceed 4000 m/s (Fig. F43), with the highest velocities of 5000–6000 m/s corresponding to the bottom of the basement Unit 2 (see "Igneous Petrology," p. 17). The high compressional wave velocity close to 6000 m/s in the lowermost basalt unit are related to high bulk density and very low porosity values (Fig. F43). The velocities close to 6000 m/s appear to be unusually high; however, a comparable data range of 5000–6000 m/s was also observed (e.g., in Hole 917A basalts). These data could also be a consequence of the calibration method (see "Physical Properties," p. 31, in the "Explanatory Notes" chapter).

Thermal Conductivity

We determined thermal conductivity on selected lithified sediments and basaltic rock samples from Site 1136 (Table T13). In the sedimentary section, thermal conductivity values show no significant changes with depth. Between 26.2 and 48.1 mbsf, thermal conductivity averages 1.22 W/(m·K), which agrees well with those of samples measured from Hole 1135A (see "Physical Properties," p. 15, in the "Site 1135" chapter). The basalt, on the other hand, exhibits higher thermal conductivity values ranging between 1.48 and 2.02 W/(m·K) in the depth interval from 130.8 to 157.1 mbsf (Table T13).

T13. Thermal conductivity values, p. 94.

Concluding Discussion

The physical properties data obtained at Site 1136 are heterogeneous, reflecting variations in consolidation and lithology. The most significant change is at the contact between the basalts and overlying sedimentary units (Fig. F42A). Variations in physical properties in the overlying sediments suggest smaller-scale heterogeneities in lithology and/or consolidation, although core recovery was poor throughout the sedimentary section.

ORGANIC AND INORGANIC CHEMISTRY

We determined concentrations of carbonate in sediments from Hole 1136A on ~1 sample per core (Table T14). In addition, we analyzed four of the sediment samples for organic carbon, total nitrogen, sulfur, and hydrogen. The results of the analyses are discussed in "Lithostratigraphy," p. 3.

We also analyzed five altered volcaniclastic sediment samples for total carbon, total nitrogen, sulfur, and hydrogen (Table T15). These data are discussed in "Lithostratigraphy," p. 3, and "Physical Volcanology," p. 10. Finally, for basalts that were analyzed by XRF, we determined total carbon, total nitrogen, sulfur, and hydrogen using the NCS analyzer (Table T15). These data are useful for assessing the degree of alteration in the basalts (e.g., total carbon and hydrogen can be converted to CO_2 and H_2O, respectively, and compared with loss on ignition values). Further discussion of these data can be found in "Igneous Petrology," p. 17, and "Alteration and Weathering," p. 20.

T14. Carbon, nitrogen, sulfur, and hydrogen analyses, p. 95.

T15. Carbon, nitrogen, sulfur, and hydrogen analyses, p. 96.

SEISMIC STRATIGRAPHY

Data

We used densities and compressional wave velocity from index properties and MST measurements to create synthetic seismograms at Site 1136 because no downhole logs were collected. Neither density nor velocity data at this site appear to show much variation within the sedimentary or basement section, except for noise (Fig. F44). Densities determined from core samples and the GRAPE data agree well in the sedimentary section, but not in the basement, where the core liner was not entirely filled with core. Also, core recovery between 80 and 120 mbsf was extremely low. For synthesizing a seismogram, we used densities from discrete samples, as they display much less scattering than GRAPE densities. We used densities from GRAPE data above 315 mbsf and data from discrete samples below this depth. We filtered all density and velocity data identically (Fig. F44).

F44. Comparison of densities determined from core samples, GRAPE, MST, and V_p velocities from downhole logs and core samples, p. 78.

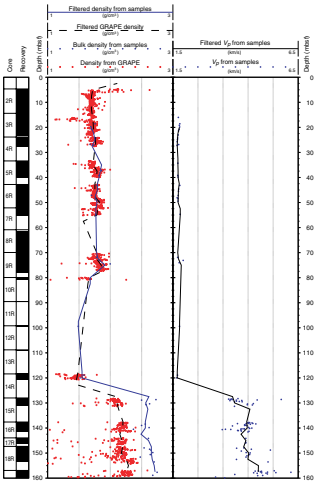

Synthetic Seismogram

We synthesized seismograms for Site 1136 (see "Seismic Stratigraphy," p. 47, in the "Explanatory Notes" chapter). We resampled both densities and velocities every 0.5 ms as a function of two-way traveltime and created profiles for impedance, reflection coefficients, and a seismic trace. The seismic trace is based on convolution with a Ricker wavelet with a peak frequency of 40 Hz. Only reflection coefficients without multiples and transmission losses were constructed for this site, given that its depth below seafloor does not exceed 160 m and that the data are fairly poor (Fig. F45).

F45. Composite of core recovery, depth, lithostratigraphy, age, density, and velocity, p. 79.

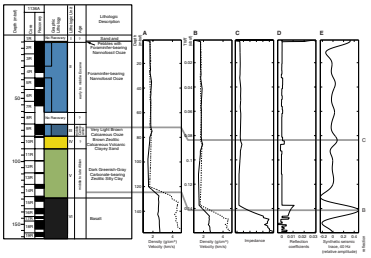

Seismic Stratigraphy

The synthetic seismogram shows only two high-amplitude reflections below the seafloor (Fig. F45). The upper reflection (C) correlates with Unit III, dated as mid-Campanian, and the lower reflection (B) corresponds to the top of acoustic basement. In Figure F45, Reflection C is 5 m above acoustic basement, rather than at the basement contact. This

is entirely an aliasing effect introduced by poor core recovery and subsequent interpolation. Both correlate with reflections in the MCS data (Fig. **F46**). However, a prominent reflection observed at ~40–50 ms below the seafloor in the MCS data is not reproduced by the synthetic seismogram. This reflection was apparently produced by the Flexichoc source used on the *Marion Dufresne* (Fig. **F46**).

F46. Seismic reflection data from *Marion Dufresne* cruise 47, line 10 across Site 1136, and a synthetic seismic trace from Figure F45, **p. 80.**

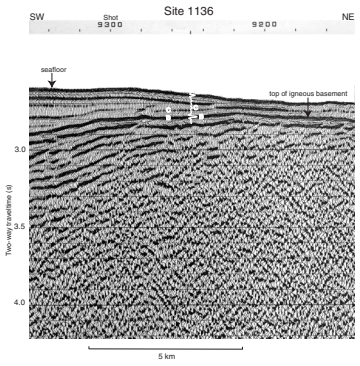

REFERENCES

Adams, R.D., and Zhang, B.M., 1984. A further earthquake on the Kerguelen Plateau. *Geophys. J. R. Astron. Soc.,* 79:697–703.

Alibert, C., 1991. Mineralogy and geochemistry of a basalt from Site 738: implications for the tectonic history of the southernmost part of the Kerguelen Plateau. *In* Barron, J., Larsen, B., et al., *Proc. ODP, Sci. Results,* 119: College Station, TX (Ocean Drilling Program), 293–298.

Berggren, W.A., 1992. Paleogene planktonic foraminifer magnetobiostratigraphy of the Southern Kerguelen Plateau (Sites 747–749). *In* Wise, S.W., Jr., Schlich, R., et al., *Proc. ODP, Sci. Results,* 120 (Pt. 2): College Station, TX (Ocean Drilling Program), 551–568.

Blum, P., 1997. Physical properties handbook: a guide to the shipboard measurements of physical properties of deep-sea cores. *ODP Tech. Note,* 26.

Bown, P.R., Rutledge, D.C., Crux, J.A., and Gallagher, L.T., 1998. Lower Cretaceous. *In* Bown, P.R. (Ed.), *Calcareous Nannofossil Biostratigraphy:* Dordvecht (Kluwer Academic Publishers), 92–131.

Boyce, R.E., 1973. Physical properties—methods. *In* Edgar, N.T., Saunders, J.B., et al., *Init. Repts. DSDP,* 15: Washington (U.S. Govt. Printing Office), 1115–1128.

Bralower, T. J., 1992. Aptian-Albian calcareous nannofossil biostratigraphy of ODP Site 763 and the correlation between high- and low-latitude zonations. *In* Duncan, R.A., Rea, D.K., Kidd, R.B., von Rad, U., and Weissel, J.K. (Eds.), *Synthesis of Results from Scientific Drilling in the Indian Ocean.* Geophys. Monogr., Am. Geophys. Union, 70:245–252.

Bralower, T.J., Sliter, W.V., Arthur, M.A., Leckie, R.M., Allard, D.J., and Schlanger, S.O., 1993. Dysoxic/anoxic episodes in the Aptian-Albian (Early Cretaceous). *In* Pringle, M.S., Sager, W.W., Sliter, M.V., and Stein, S. (Eds.), *The Mesozoic Pacific: Geology, Tectonics, and Volcanism.* Geophys. Monogr., Am. Geophys. Union, 77:5–37.

Caron, M., 1985. Cretaceous planktic foraminifera. *In* Bolli, H.M., Saunders, J.B., and Perch-Nielsen, K. (Eds), *Plankton Stratigraphy:* Cambridge (Cambridge Univ. Press), 17–86.

Cita, M.B., Coccioni, R., Edwards, A.R., Monechi, S., Morgans, H.E.G., Strong, C.P., Watkins, D.K., and Webb, P.-N., 1997. Nannofossils and foraminifera. *In* Hannah, M.J., and Raine, J.I. (Eds.), *Southern Ocean Late Cretaceous/Early Cenozoic Biostratigraphic Datums.* Inst. Geol. Nucl. Sci., Sci. Rep., 97/4:5–10.

Davies, H.L., Sun, S.-S., Frey, F.A., Gautier, I., McCulloch, M.T., Price, R.C., Bassias, Y., Klootwijk, C.T., and Leclaire, L., 1989. Basalt basement from the Kerguelen Plateau and the trail of the DUPAL plume. *Contrib. Mineral. Petrol.,* 103:457–469.

Fisher, R.L., 1997. Bathymetry of the Southern Indian Ocean. *General Bathymetric Chart of the Oceans.* GEBCO, Sheet 97.1.

Gradstein, F.M., Agterberg, F.P., Ogg, J.G., Hardenbol, J., van Veen, P., Thierry, J., and Huang, Z., 1995. A Triassic, Jurassic and Cretaceous time scale. *In* Berggren, W.A., Kent, D.V., and Aubry, M.P., and Hardenbol, J. (Eds.), *Geochronology, Time Scales and Global Stratigraphic Correlation.* Spec. Publ.—Soc. Econ. Paleontol. Mineral., 54:95–126.

Heider, F., Geiss, C., Dunlop, D.J., and Inokuchi, H., 1992. Rock-magnetic investigation of basalts from the southern Kerguelen Plateau (Leg 120). *In* Wise, S.W., Jr., Schlich, R., et al., *Proc. ODP, Sci. Results,* 120: College Station, TX (Ocean Drilling Program), 79–87.

Huber, B.T., 1990. Maestrichtian planktonic foraminifer biostratigraphy of the Maud Rise (Weddell Sea, Antarctica): ODP Leg 113 Holes 689B and 690C. *In* Barker, P.F., Kennett, J.P., et al., *Proc. ODP, Sci. Results,* 113: College Station, TX (Ocean Drilling Program), 489–513.

————, 1991. Paleogene and early Neogene planktonic foraminifer biostratigraphy of Sites 738 and 744, Kerguelen Plateau (southern Indian Ocean). *In* Barron, J.,

Larsen, B., et al., *Proc. ODP, Sci. Results,* 119: College Station, TX (Ocean Drilling Program), 427–449.

————, 1992. Upper Cretaceous planktic foraminiferal biozonation for the Austral Realm. *Mar. Micropaleontol.,* 20:107–128.

Inokuchi, H., and Heider, F., 1992. Paleolatitude of the southern Kerguelen Plateau inferred from the paleomagnetic study of Upper Cretaceous basalts. *In* Wise, S.W., Jr., Schlich, R., et al., *Proc. ODP, Sci. Results,* 120: College Station, TX (Ocean Drilling Program), 89–96.

Johnson, G.R., and Olhoeft, G.R., 1984. Density of rocks and minerals. *In* Carmichael, R.S. (Ed.), *Handbook of Physical Properties of Rocks* (Vol. 3): Boca Raton, FL (CRC Press), 1–38.

Krasheninnikov, V.A., and Basov, I.A., 1983. Stratigraphy of Cretaceous sediments of the Falkland Plateau based on planktonic foraminifers, Deep Sea Drilling Project, Leg 71. *In* Ludwig, W.J., Krasheninnikov, V.A., et al., *Init. Repts. DSDP,* 71: Washington (U.S. Govt. Printing Office), 789–820.

Macdonald, G.A., and Katsura, T., 1964. Chemical composition of Hawaiian lavas. *J. Petrol.,* 5:82–133.

Mahoney, J.J., Jones, W.B., Frey, F.A., Salters, V.J.M., Pyle, D.G., and Davies, H.L., 1995. Geochemical characteristics of lavas from Broken Ridge, the Naturaliste Plateau and southernmost Kerguelen Plateau: Cretaceous plateau volcanism in the southeast Indian Ocean. *Chem. Geol.,* 120:315–345.

Mehl, K.W., Bitschene, P. R., Schminke, H.-U., and Hertogen, J., 1991. Composition, alteration, and origin of the basement lavas and volcaniclastic rocks at Site 738, southern Kerguelen Plateau. *In* Barron, J., Larsen, B., et al., *Proc. ODP, Sci. Results,* 119: College Station, TX (Ocean Drilling Program), 299–322.

Okal, E.A., 1981. Intraplate seismicity of Antarctica and tectonic implications. *Earth Planet. Sci. Lett.,* 52:397–409.

Quilty, P.G., 1992. Upper Cretaceous planktonic foraminifers and biostratigraphy, Leg 120, southern Kerguelen Plateau. *In* Wise, S.W., Jr., Schlich, R., et al., *Proc. ODP, Sci. Results,* 120: College Station, TX (Ocean Drilling Program), 371–392.

Rotstein, Y., Munschy, M., Schlich, R., and Hill, P.J., 1991. Structure and early history of the Labuan Basin, South Indian Ocean. *J. Geophys. Res.,* 96:3887–3904.

Salters, V.J.M., Storey, M., Sevigny, J.H., and Whitechurch, H., 1992. Trace element and isotopic characteristics of Kerguelen-Heard Plateau basalts. *In* Wise, S.W., Jr., Schlich, R., et al., *Proc. ODP, Sci. Results,* 120: College Station, TX (Ocean Drilling Program), 55–62.

Sandwell, D.T., and Smith, W.H.F., 1997. Marine gravity anomaly from Geosat and ERS-1 satellite altimetry. *J. Geophys. Res.,* 102:10039–10054.

Self, S., Thordarson, T., and Keszthelyi, L., 1997. Emplacement of continental flood basalt lava flows. *In* Mahoney, J.J., and Coffin, M. (Eds.), *Large Igneous Provinces: Continental, Oceanic, and Planetary Flood Volcanism.* Am. Geophys. Union., Geophys. Monogr., 100:381–410.

Storey, M., Kent, R.W., Saunders, A.D., Salters, V.J., Hergt, J., Whitechurch, H., Sevigny, J.H., Thirlwall, M.F., Leat, P., Ghose, N.C., and Gifford, M., 1992. Lower Cretaceous volcanic rocks on continental margins and their relationship to the Kerguelen Plateau. *In* Wise, S.W., Jr., Schlich, R., et al., *Proc. ODP, Sci. Results,* 120: College Station, TX (Ocean Drilling Program), 33–53.

Stott, L.D., and Kennett, J.P., 1990. Antarctic Paleogene planktonic foraminifer biostratigraphy: ODP Leg 113, Sites 689 and 690. *In* Barker, P.F., Kennett, J.P., et al., *Proc. ODP, Sci. Results,* 113: College Station, TX (Ocean Drilling Program), 549–569.

Sun, S.-S., and McDonough, W.F., 1989. Chemical and isotopic systematics of oceanic basalts: implications for mantle composition and processes. *In* Saunders, A.D., and Norry, M.J. (Eds.), *Magmatism in the Ocean Basins.* Geol. Soc. Spec. Publ. London, 42:313–345.

Weis, D., Bassias, Y., Gautier, I., and Mennesier, J.-P., 1989. DUPAL anomaly in existence 115 Ma ago: evidence from isotopic study of the Kerguelen Plateau (South Indian Ocean). *Geochim. Cosmochim. Acta,* 53:2125–2131.

Williams, G.L., Stover, L.E., and Kidson, E.J., 1993. Morphology and Stratigraphic Ranges of Selected Mesozoic-Cenozoic Dinoflagellate Taxa in the Northern Hemisphere. *Pap.—Geol. Surv. Can.,* 92-10.

Wise, S.W., Jr., 1983. Mesozoic and Cenozoic calcareous nannofossils recovered by Deep Sea Drilling Project Leg 71 in the Falkland Plateau region, Southwest Atlantic Ocean. *In* Ludwig, W.J., Krasheninnikov, V.A., et al., *Init. Repts. DSDP,* 71 (Pt. 2): Washington (U.S. Govt. Printing Office), 481–550.

Wise, S.W., Jr., and Wind, F.H., 1977. Mesozoic and Cenozoic calcareous nannofossils recovered by DSDP Leg 36 drilling on the Falkland Plateau, Southwest Atlantic sector of the Southern Ocean. *In* Barker, P.F., Dalziel, I.W.D., et al., *Init. Repts. DSDP,* 36: Washington (U.S. Govt. Printing Office), 269–492.

Figure F1. Satellite-derived free-air gravity map of the Kerguelen Plateau (after Sandwell and Smith, 1997). The five plateau province sectors are northern, central, southern, Elan Bank, and Labuan Basin (outlined in white). Current (Leg 183) and previous (Legs 119 and 120) ODP sites are indicated by stars and circles, respectively (black = basement sites; white = sediment sites). Squares = dredge and piston core sites where igneous rock (black) and sediment (white) were recovered. **(Figure shown on next page.)**

Figure F1. (Caption on previous page.)

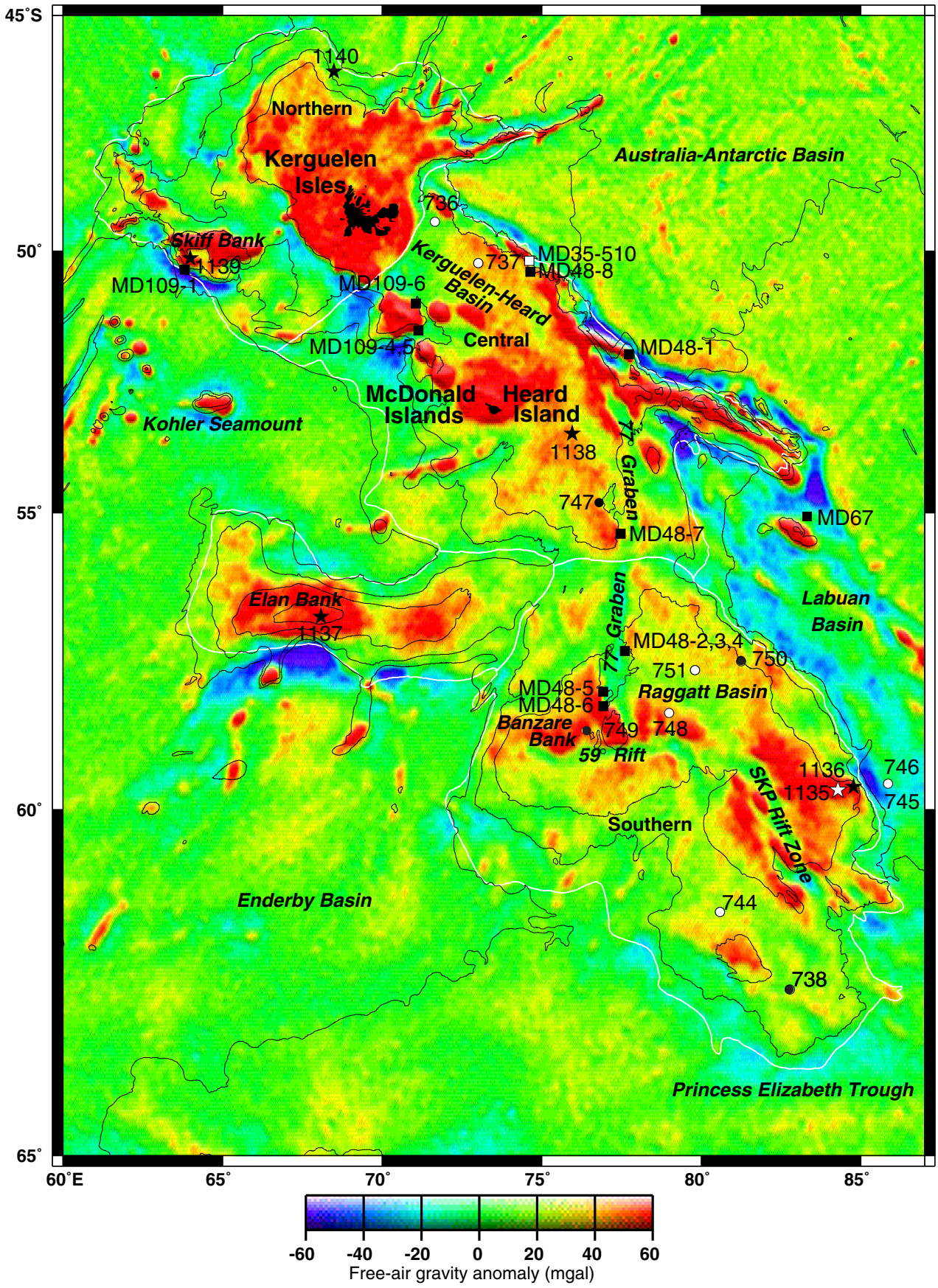

Figure F2. Location of Site 1136 and site-survey data. Navigation for *Rig Seismic* survey 180, line 201 (RS180/201) and *Marion Dufresne* cruise 47, line 10 (MD47/10) is shown in Julian daytime and shotpoint number, respectively. Bathymetric contour interval = 500 m (Fisher, 1997).

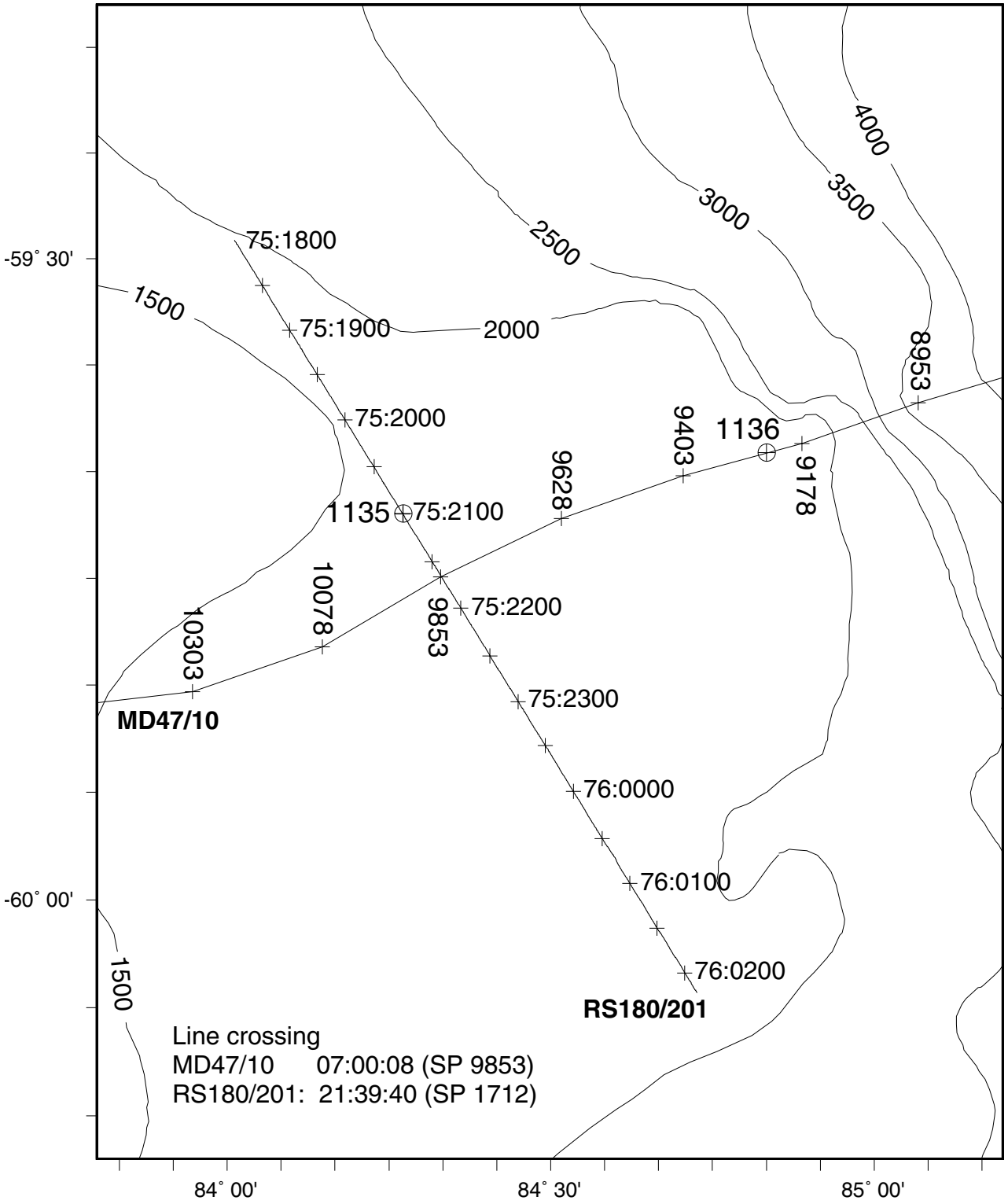

Figure F3. *Marion Dufresne* cruise 47, line 10 multichannel seismic profile across Site 1136. Vertical exaggeration = ~6.67 at seafloor.

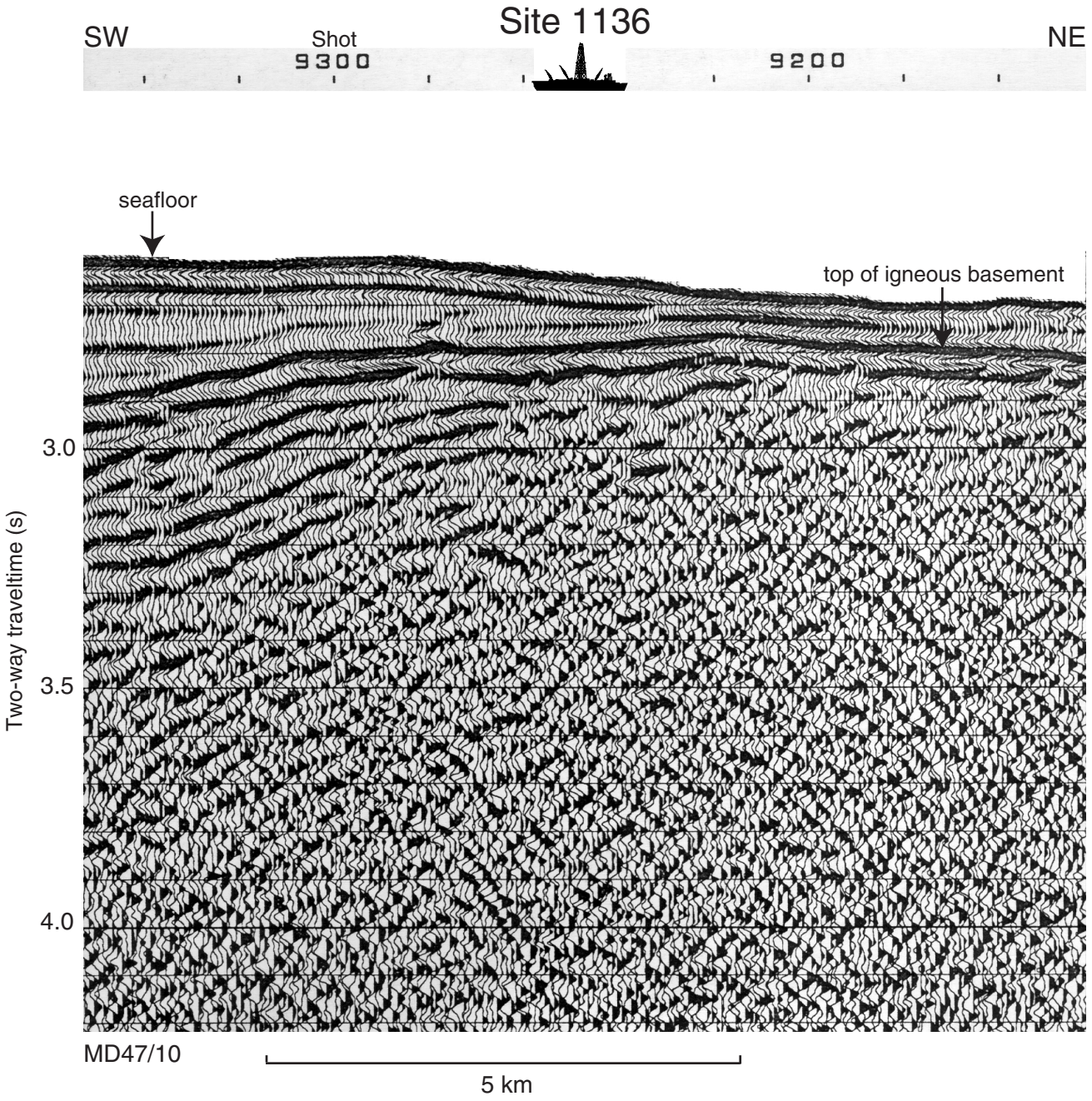

Figure F4. Composite stratigraphic section for Site 1136 showing core recovery, a simplified summary of lithology, lithologic unit boundaries, ages of units, names of lithologies, and calcium carbonate content downhole (Table T14, p. 95). Note that drilling records indicate that basalt was encountered at ~133 mbsf (see "Operations," p. 2), slightly deeper than the curated depth for the base of Unit V, which is placed at the contact between Unit V sediments and basalt (128.08 m) in Core 183-1136A-15R. The lithologic symbols are explained in Figure F3, p. 57, in the "Explanatory Notes" chapter.

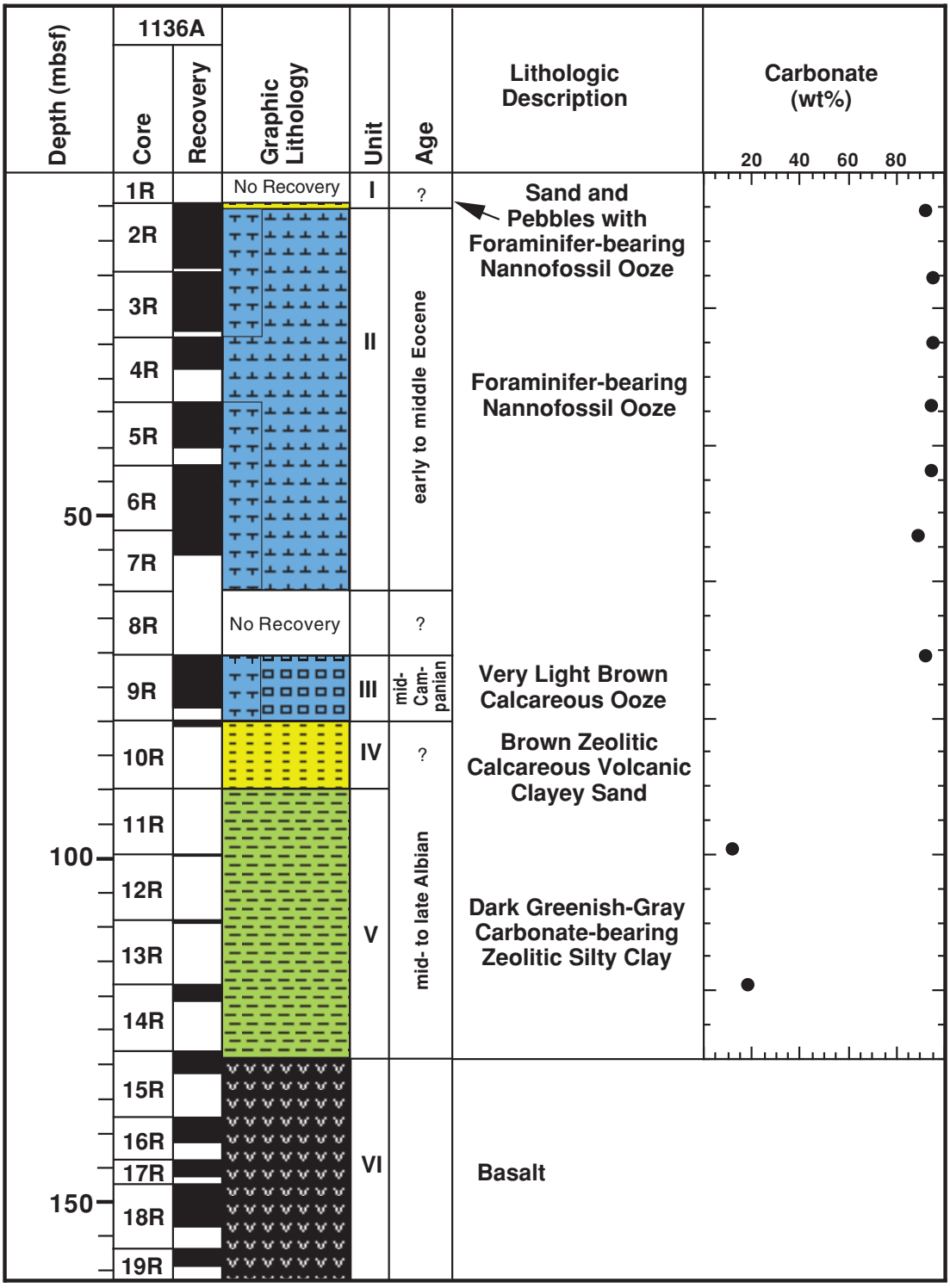

Figure F5. Site 1136 age-depth plot. The lithologic symbols are explained in Figure F3, p. 57, in the "Explanatory Notes" chapter.

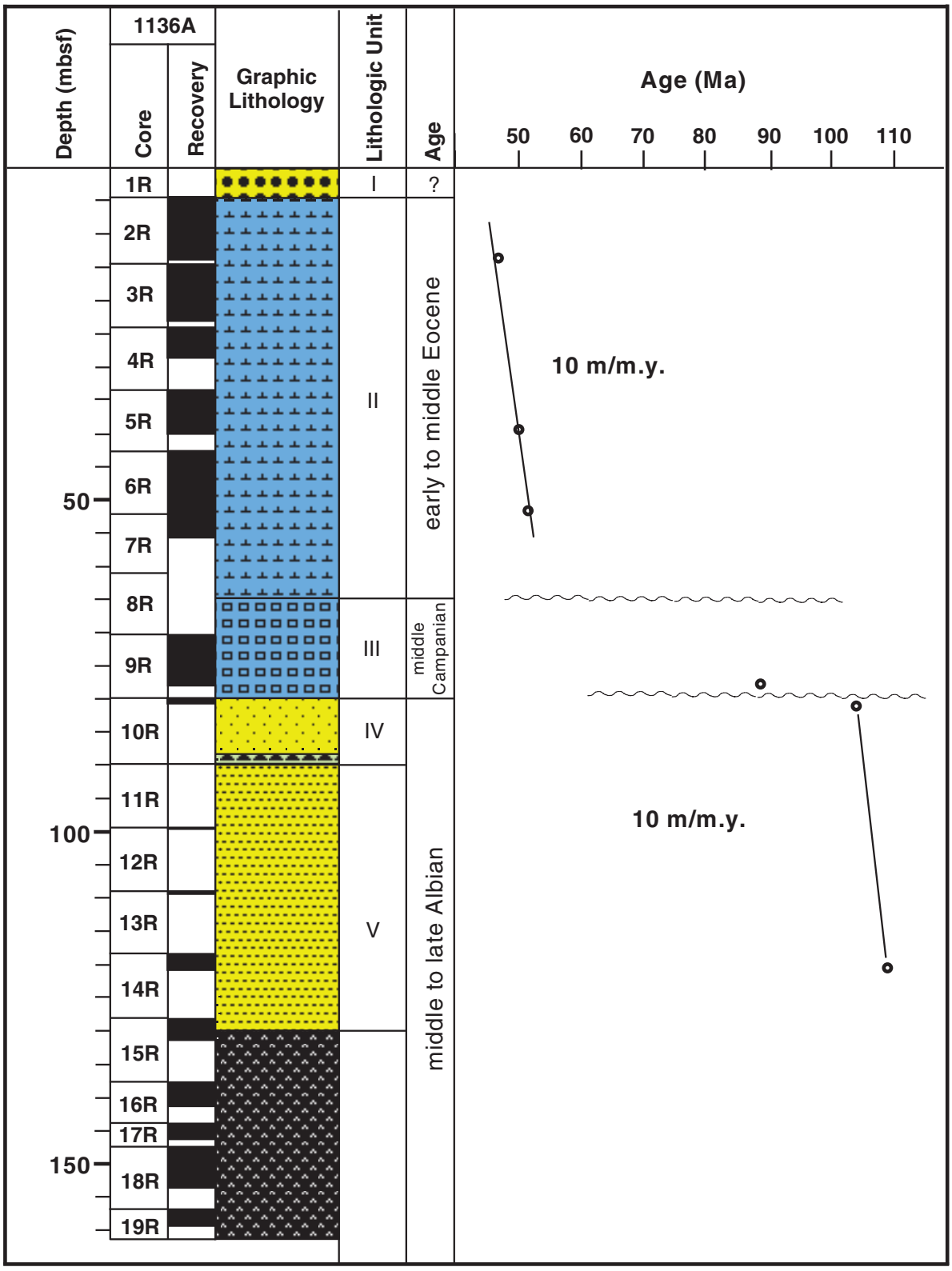

Figure F6. Color close-up photograph of interval 183-1136A-10R-1, 80–90 cm, showing the base of the massive brown zeolitic calcareous volcanic clayey sand from lithologic Unit IV. The presence of 10%–15% palagonitized glass shards imparts the brown color. Note the subrounded basaltic pebble in this interval. Below the sand is a piece of brown and white silicified mafic volcanic breccia with clasts that are internally brecciated.

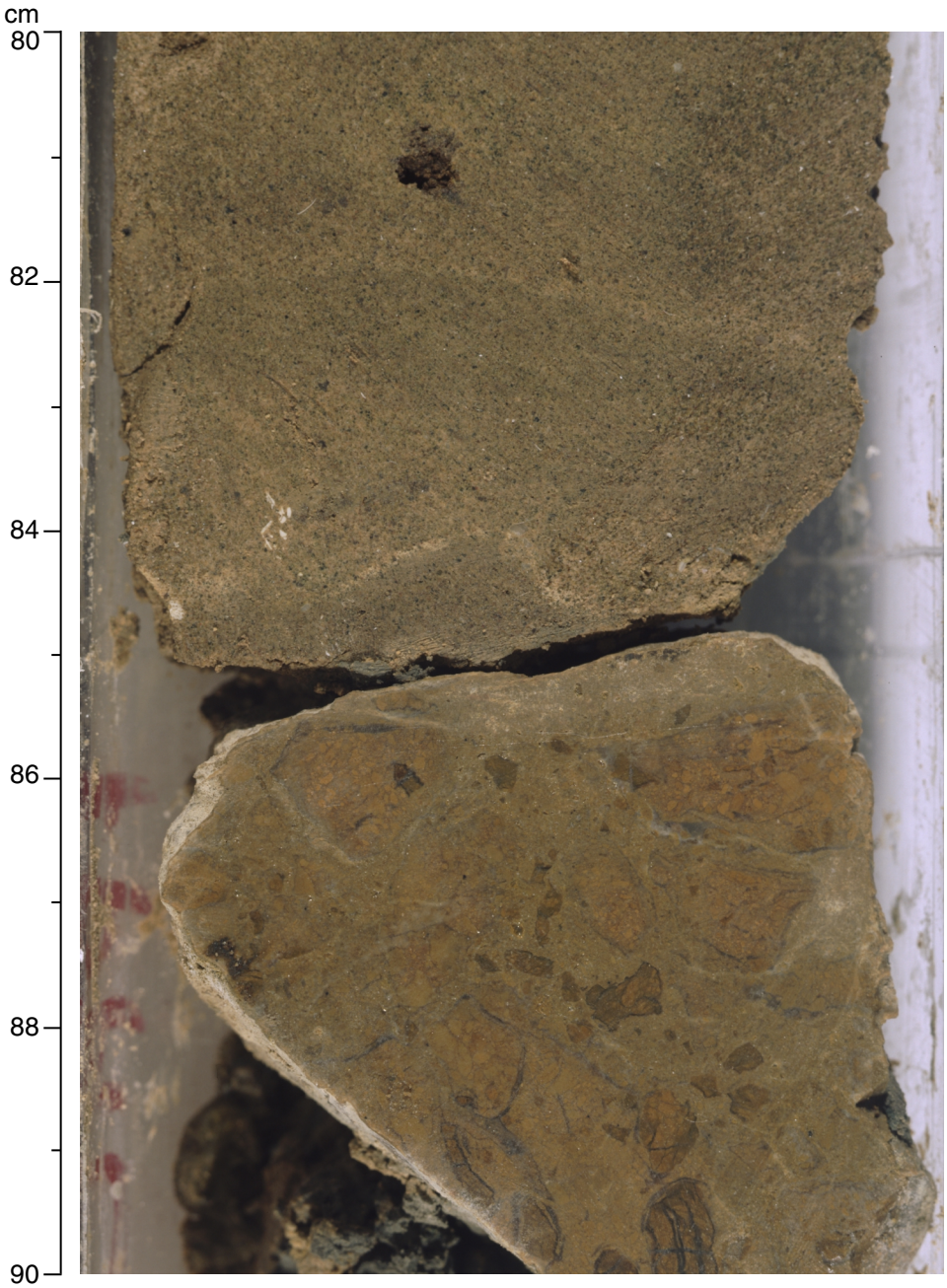

Figure F7. Color close-up photograph of interval 183-1136A-14R-1, 97–115 cm, showing bivalve shell material and other fossil detritus mixed with zeolitic silty clay sediments, indicating reworking. Alteration has resulted in green iron-rich clay (nontronite and/or saponite) and mica (celadonite) in halos around fossil fragments in the permeable silt layers and along fractures.

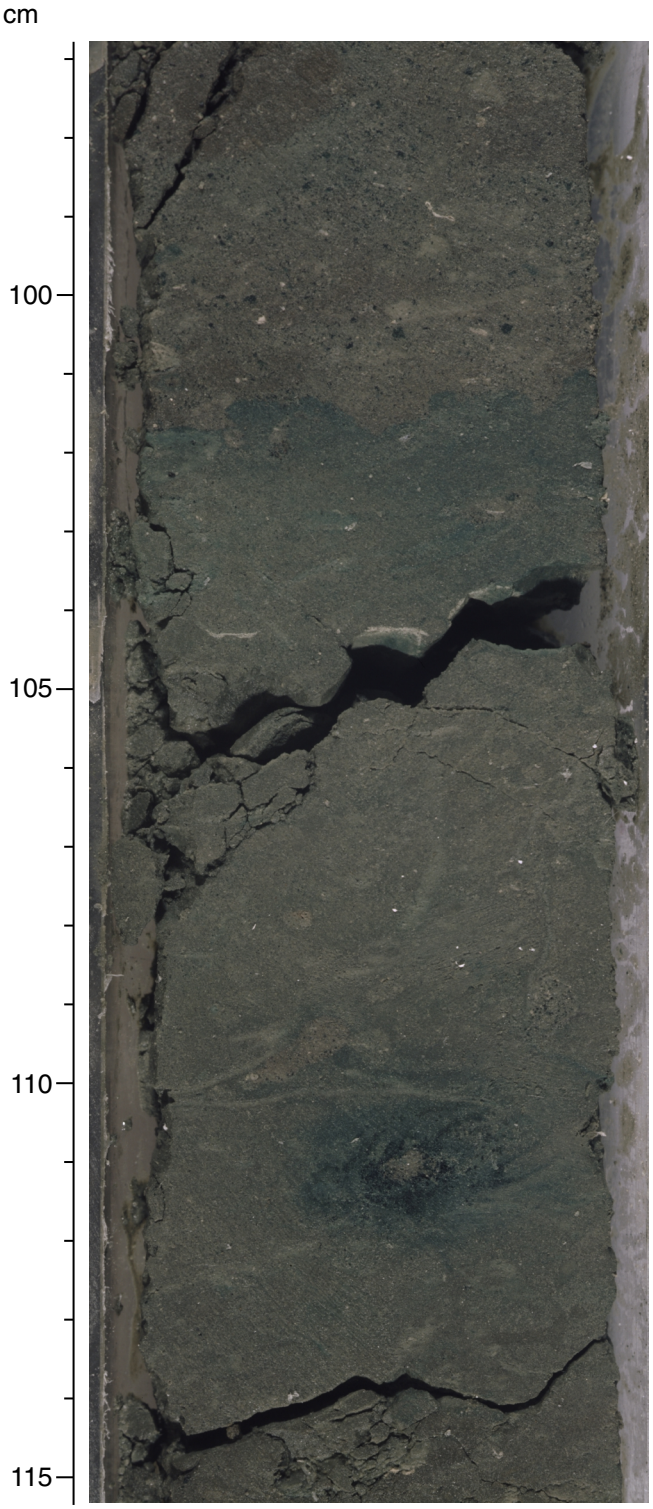

Figure F8. Lava-flow recovery and interpretive cross section. Left side shows curated unit boundary locations, and right side shows interpreted locations. Nonrecovery (hatched area) is interpreted to be primarily in the vesicular flow tops. Note the resulting changes in the estimated thicknesses of parts of individual lava flows.

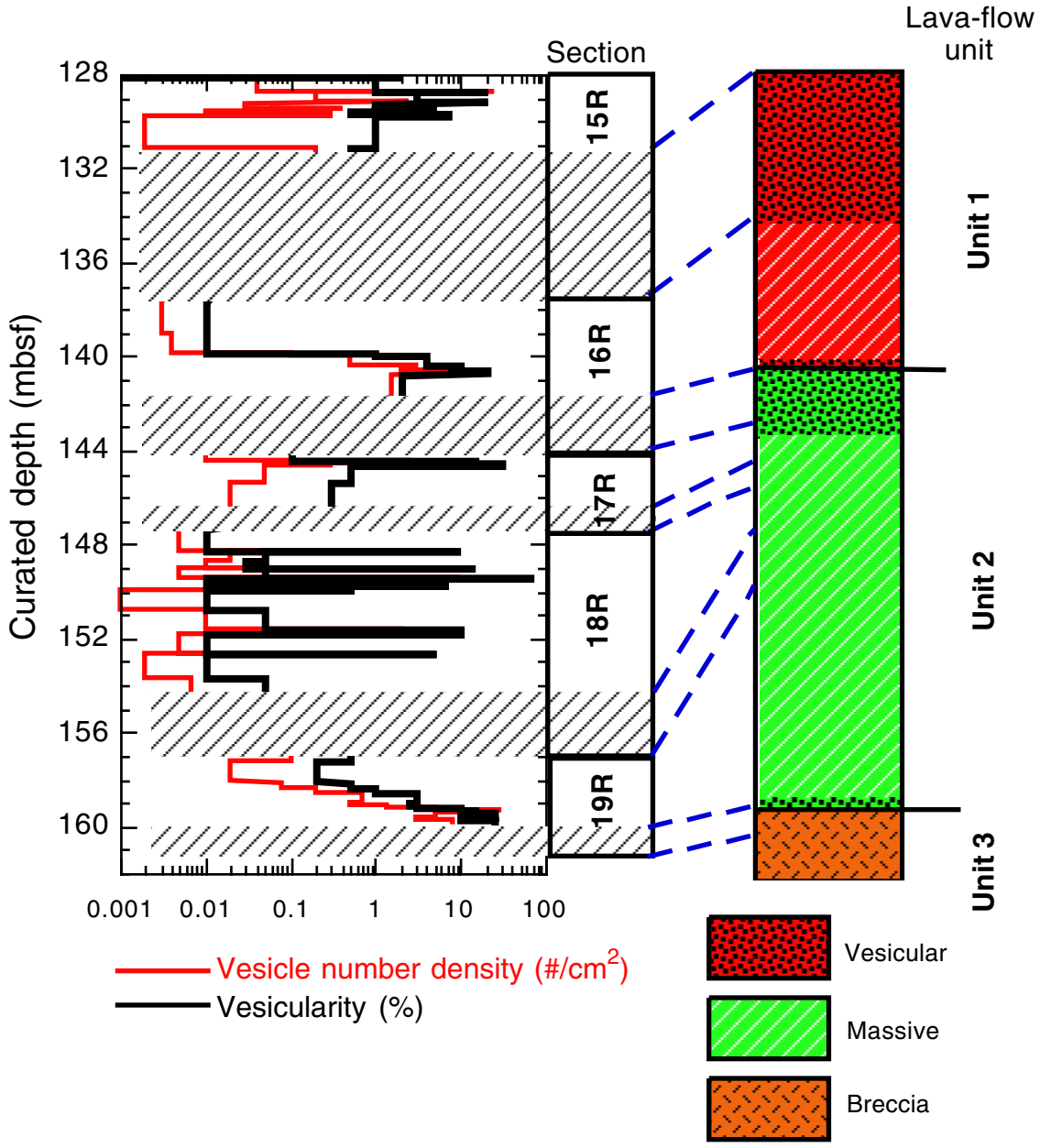

Figure F9. Close-up photograph of interval 183-1136A-15R-2, 120–135 cm. Note the horizontal vesicle sheet from 128 to 130.5 cm with angular vesicles and the change in groundmass texture. Vesicles are filled with carbonate and minor zeolite ± clay, whereas subhorizontal veins are filled with carbonate and minor zeolites.

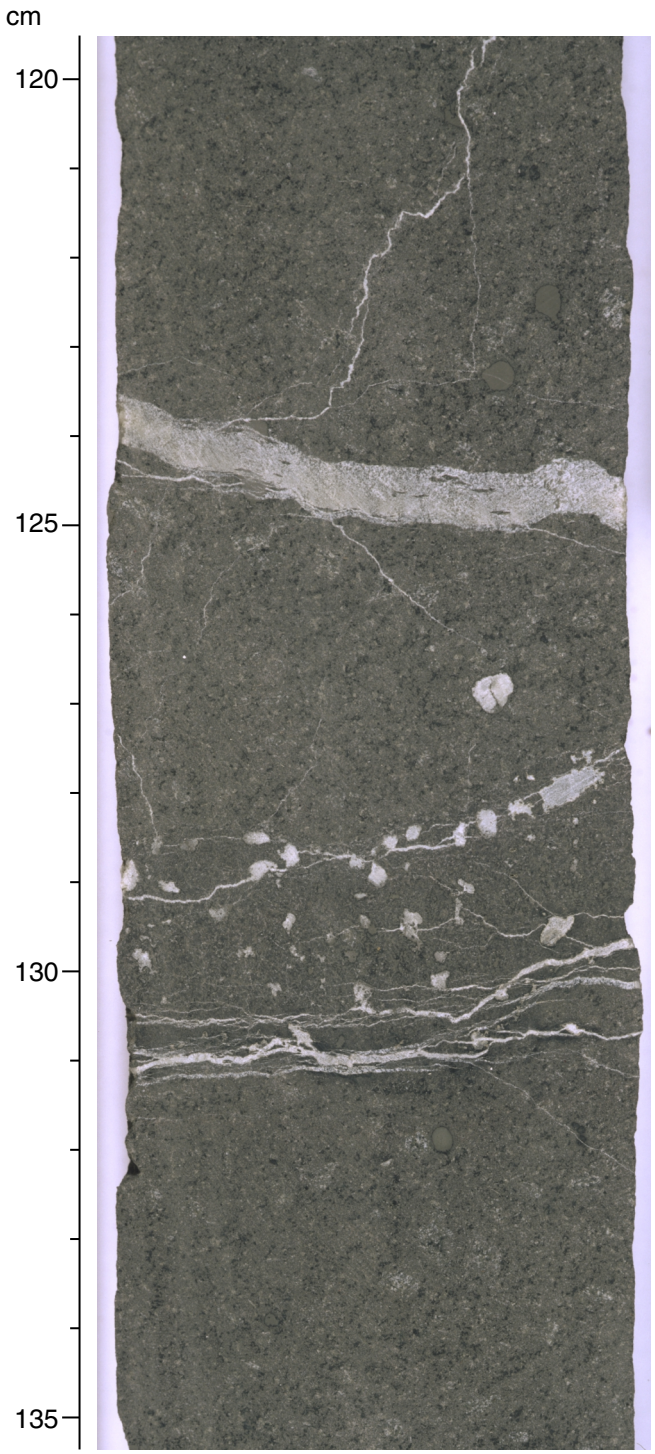

Figure F10. Close-up photograph of interval 183-1136A-19R-2, 80–120 cm, showing the vesicular base of basement Unit 2 and the brecciated top of basement Unit 3.

Figure F11. Vesicle distribution at the base of basement Units 1 and 2. Note the similarities and that the lowermost few centimeters of Unit 1 are missing.

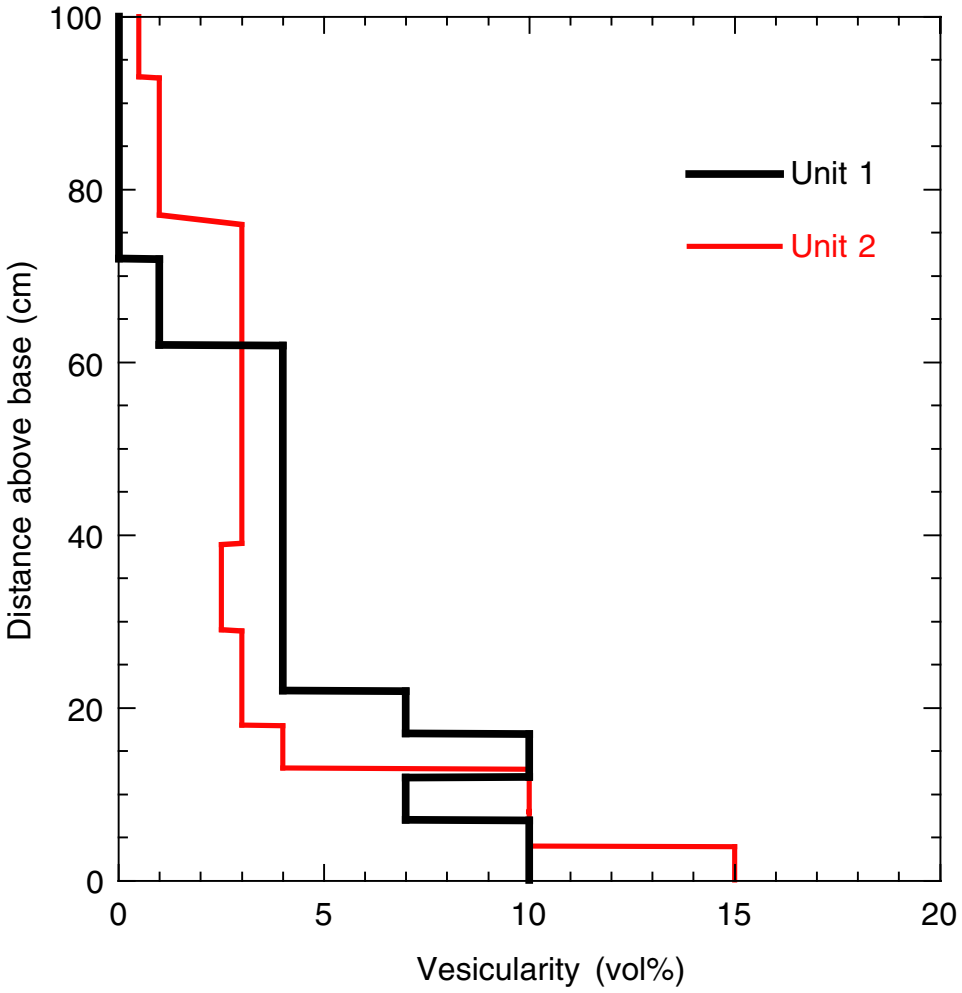

Figure F12. Interpretative summary of the lithology and abundances of phenocryst minerals in the three basaltic flows sampled in Cores 183-1136A-15R through 19R. The proportions of vesicles and phenocrysts, and the degree of alteration, are expressed in volume percent. Solid circles in the four columns on the right of the figure indicate points where thin sections were taken.

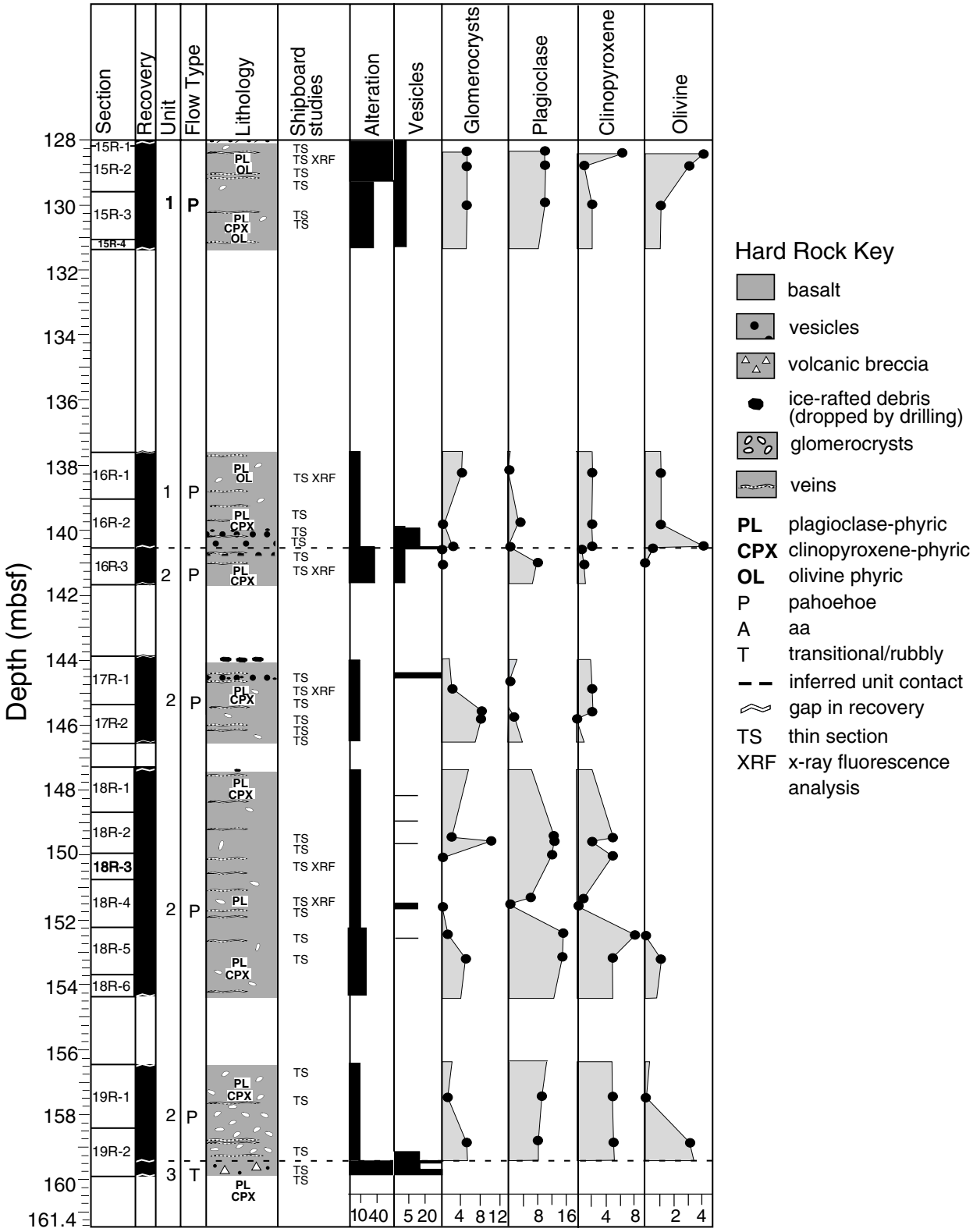

Figure F13. Typical texture of a basalt from Hole 1136A. An isolated subhedral plagioclase phenocryst lies in a groundmass of finer grains of plagioclase, clinopyroxene, titanomagnetite, and altered glass. Sample 183-1136A-16R-1 (Piece 2, 80–82 cm), plane-polarized light; width of field of view = 1 mm.

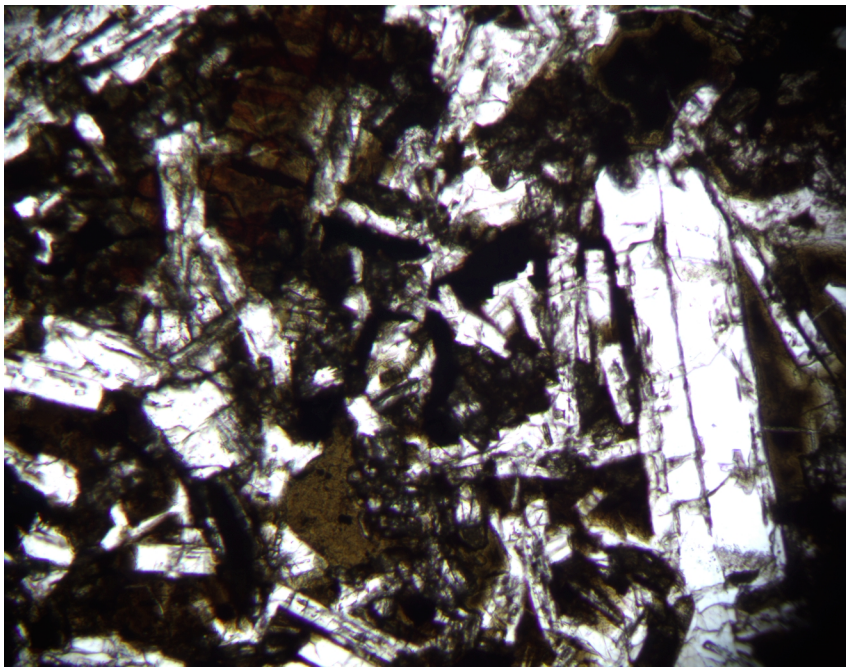

Figure F14. Compact glomeroporphyritic intergrowth. Note the fine oscillatory zoning and the presence of small rounded plagioclase inclusions in the larger plagioclase grains. The shape of the largest grain and the concentric form of the oscillatory zoning indicates that the grain grew radially out from the center of the glomeroporphyritic intergrowth, which lies in the center left of the photo. Sample 183-1136A-16R-1 (Piece 3, 80–82 cm) in cross-polarized light; width of field of view = 3 mm.

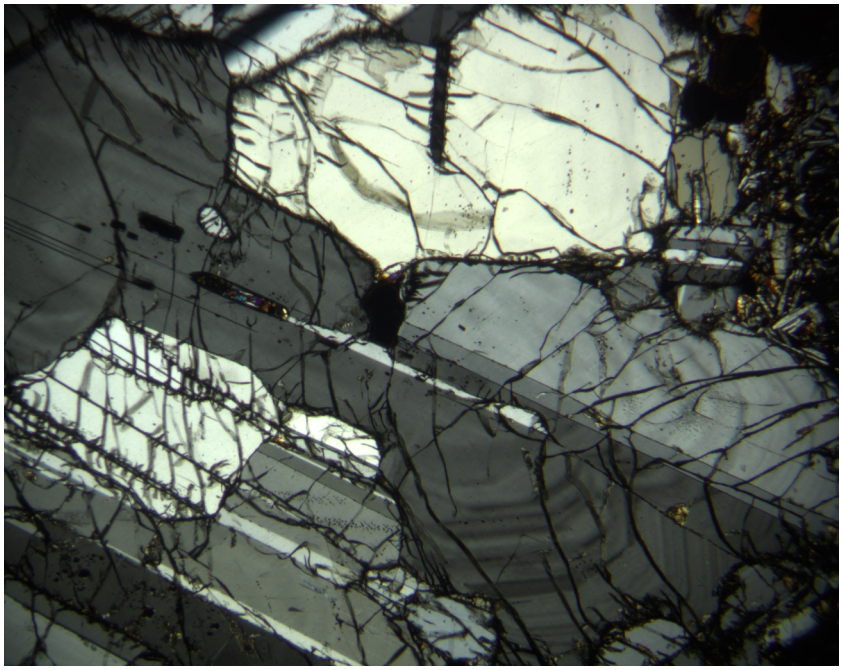

Figure F15. Plagioclase grains with abundant glass inclusions, from a compact glomeroporphyritic intergrowth in Sample 183-1136A-15R-2 (Piece 1, 51–54 cm) in plane-polarized light; width of field of view = 4 mm.

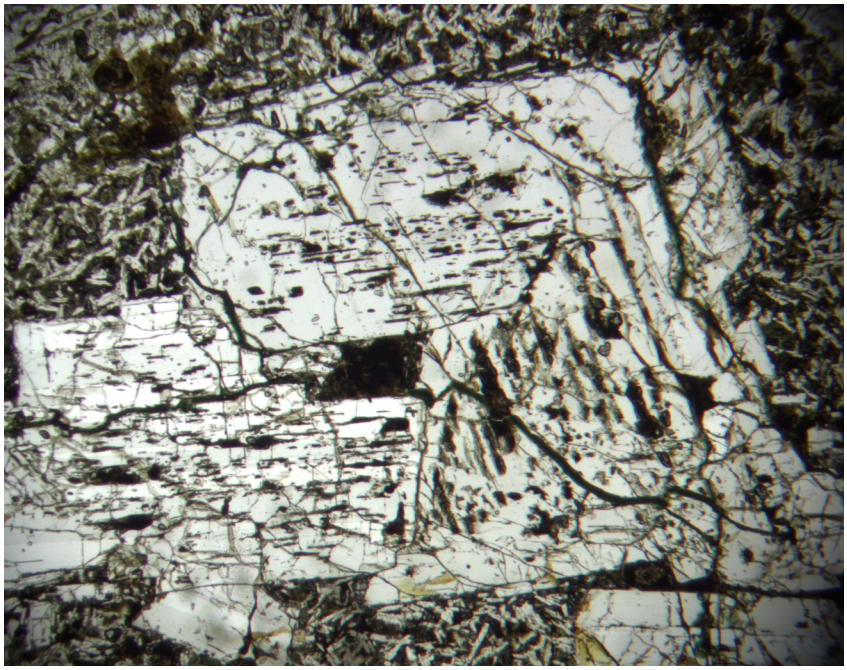

Figure F16. Rounded untwinned plagioclase grains included in larger plagioclase grains in a compact glomeroporphyritic intergrowth. Note the small polygonal glass inclusions in the centers of several grains. Sample 183-1136A-17R-1 (Piece 15, 111–117 cm) in plane-polarized light; width of field of view = 2 mm.

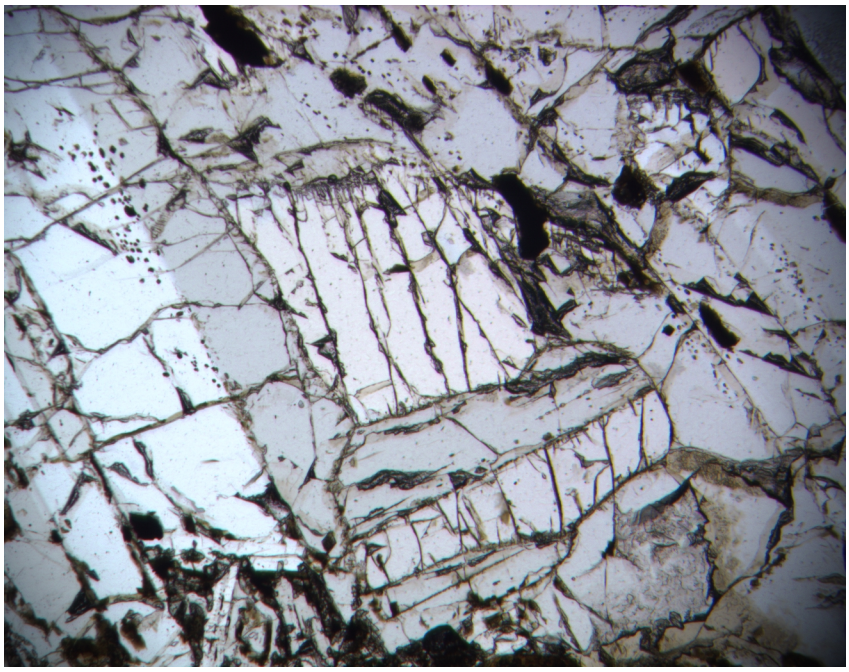

Figure F17. Discontinuous plagioclase rim around a compact glomeroporphyritic intergrowth. Sample 183-1136A-17R-1 (Piece 15, 111–117 cm) in plane-polarized light; width of field of view = 3 mm.

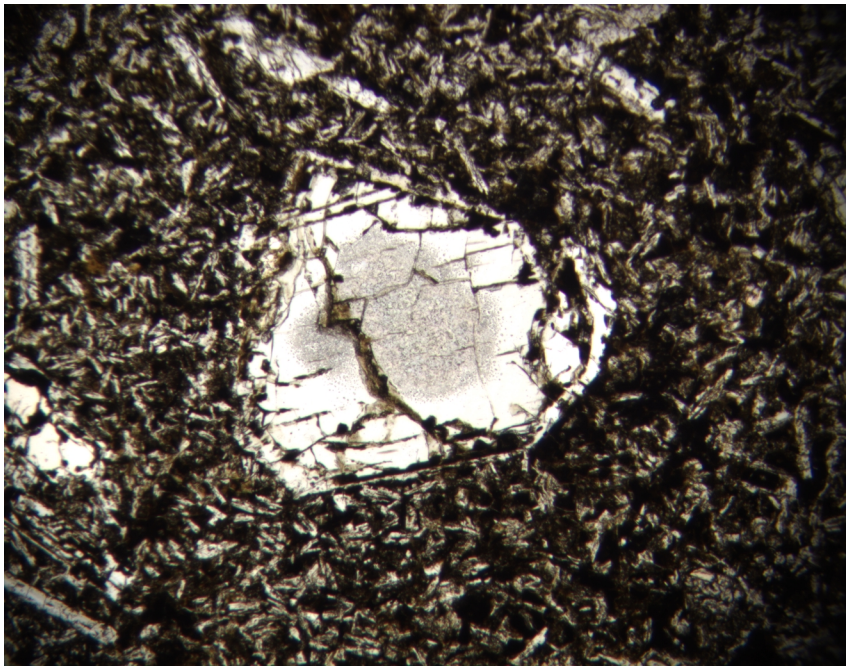

Figure F18. Microgabbro xenolith. Sample 183-1136A-19R-1 (Piece 5, 70–73 cm) in plane-polarized light; width of field of view = 2 mm.

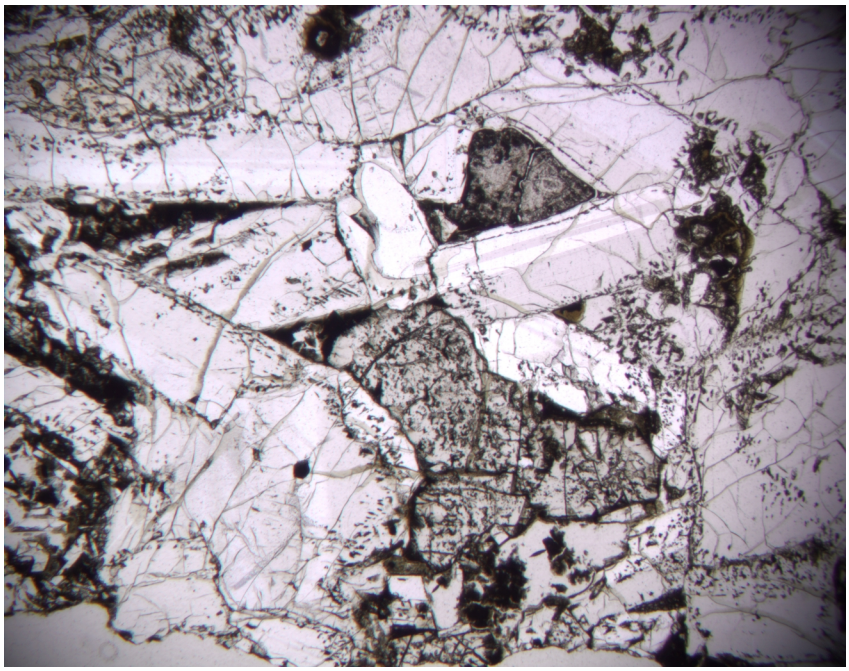

Figure F19. Groundmass of a subhorizontal segregation. Euhedral plagioclase grains, less abundant clinopyroxene crystals, and abundant opaques with two distinct habits in a glass-rich groundmass. Sample 183-1136A-17R-1 (Piece 6, 60–64 cm) in plane-polarized light; width of field of view = 2 mm.

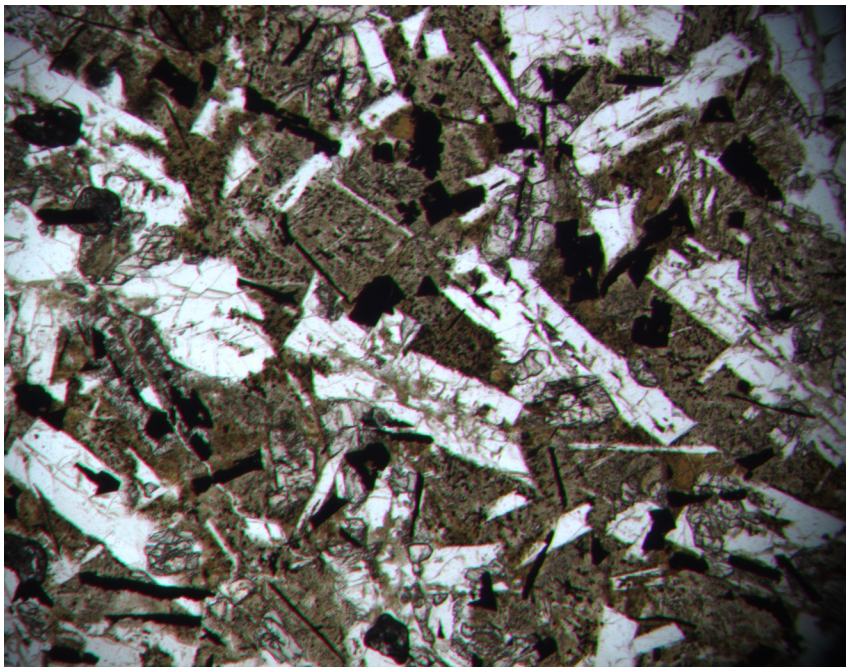

Figure F20. Detail of titanomagnetite grains in the matrix of a segregation, showing the two contrasting habits: subequant skeletal grains and elongate, serrated blades. Sample 183-1136A-17R-1 (Piece 2, 89–92 cm) in reflected light; width of field of view = 1 mm.

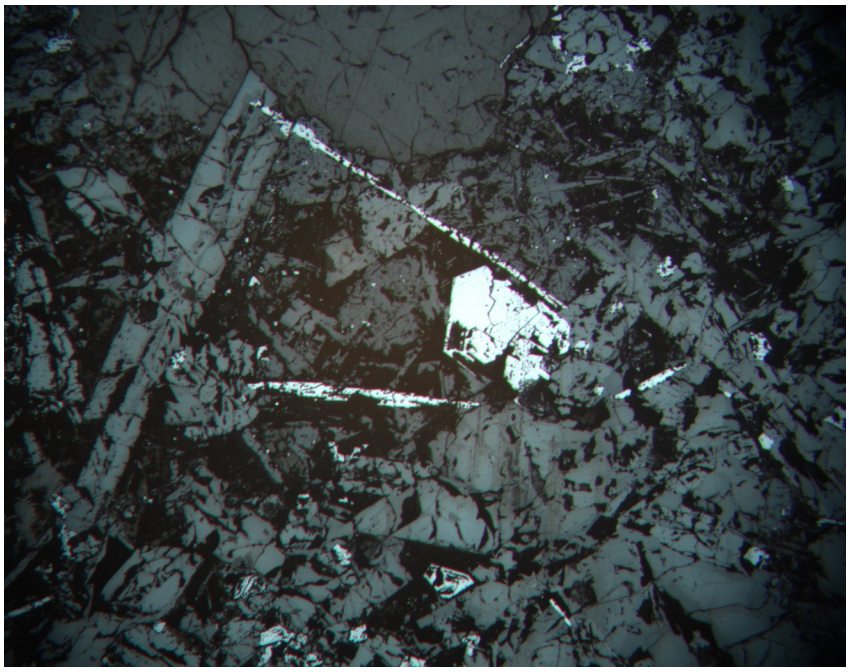

Figure F21. Margin of a segregation showing plagioclase crystals that nucleated at the contact and grew toward the center of the segregation, which is at the top of the image. Sample 183-1136A-17R-2 (Piece 6, 57–60 cm) in plane-polarized light; width of field of view = 2 mm.

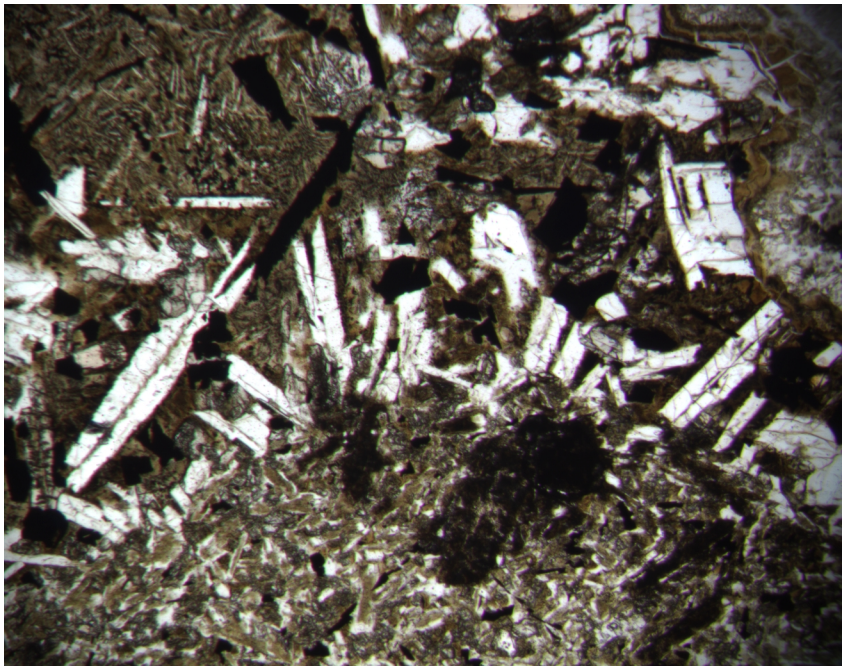

Figure F22. Diagram of SiO_2 vs. total alkalies ($Na_2O + K_2O$) abundance showing the compositions of Site 1136 samples. The boundary between tholeiitic and alkalic basalts is from Macdonald and Katsura (1964). Open symbols = samples from Unit 1; solid symbols = samples from Unit 2; circles = fresh samples; open square = Sample 183-1136A-15R-2 (Piece 2, 69–71 cm) (altered basalt); solid square = Sample 183-1136A-18R-4 (Piece 2, 89–92 cm) (vesicle-rich segregation).

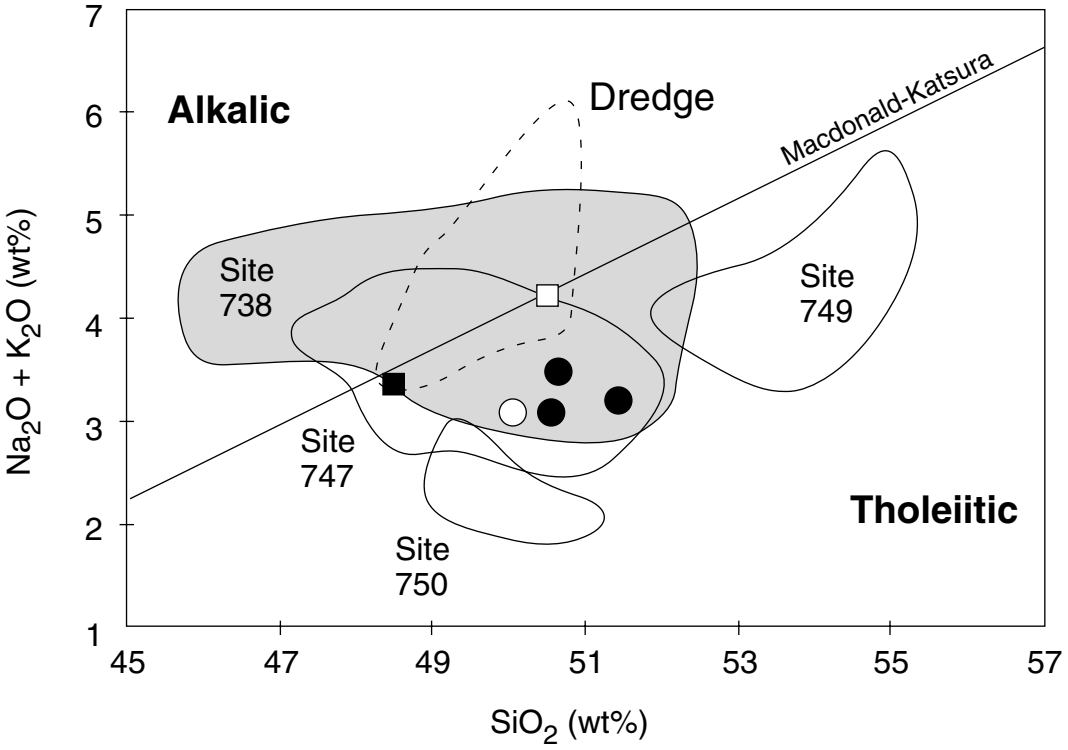

Figure F23. Major and trace element variation diagrams vs. MgO comparing basalts from Hole 1136A with those from other parts of the Kerguelen Plateau. Data sources are Davies et al. (1989), Weis et al. (1989), Alibert (1991), Mehl et al. (1991), Salters et al. (1992), Storey et al. (1992), and Mahoney et al. (1995). Open symbols = samples from Unit 1; solid symbols = samples from Unit 2; circles = fresh samples; open square = Sample 183-1136A-15R-2 (Piece 2, 69–71 cm) (altered basalt); solid square = Sample 183-1136A-18R-4 (Piece 2, 89–92 cm) (vesicle-rich segregation).

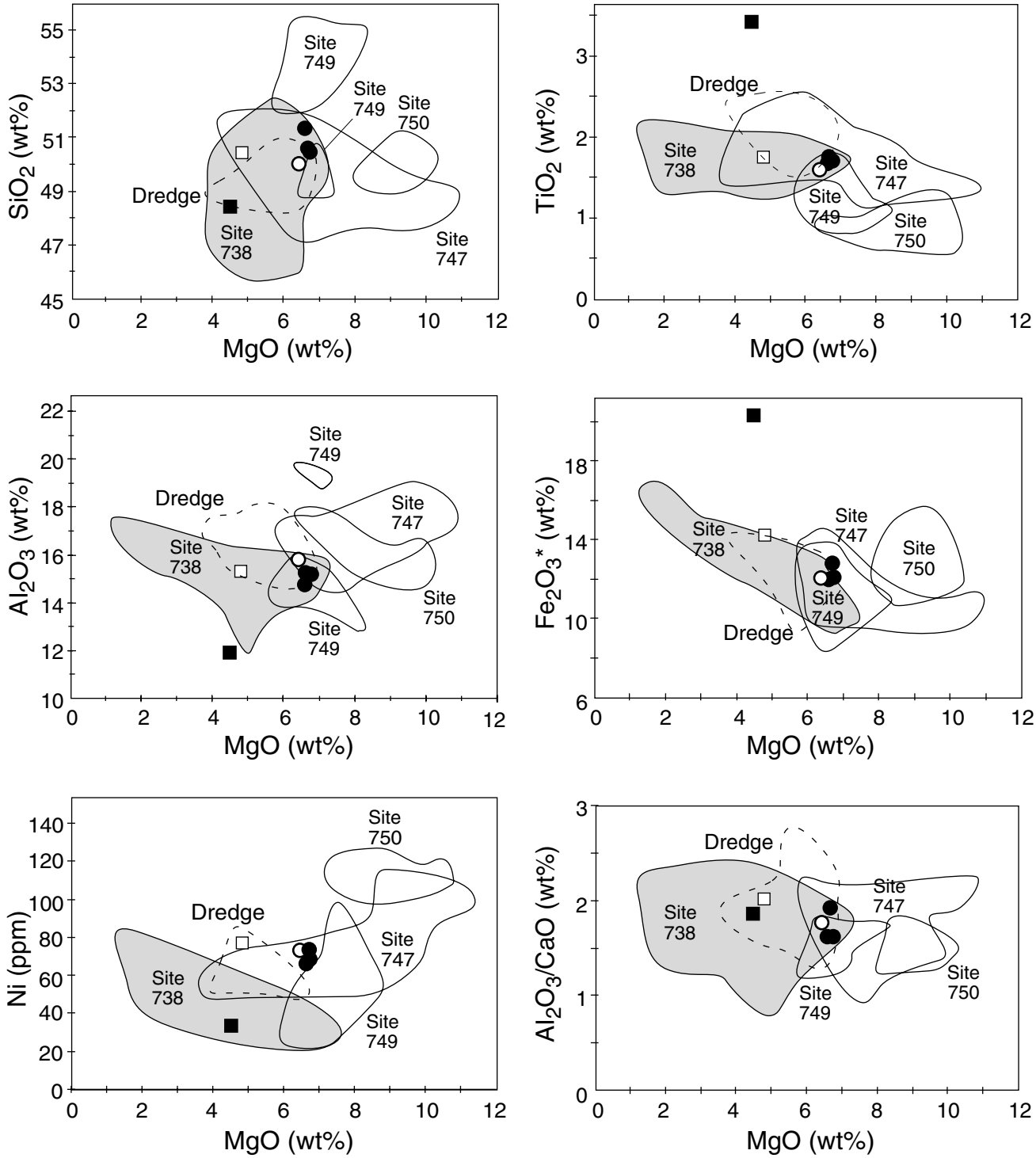

Figure F24. Trace element contents of basalts from Site 1136, normalized to primitive mantle values of Sun and McDonough (1989). This diagram illustrates the mobile behavior of Rb and K, which are highest in the altered basalt, and the relatively immobile behavior of the other elements. The presence of a continental component would produce a relative depletion (trough) at Nb. Instead, a small peak is seen in the four least-altered samples. The high contents of Nb, Zr, Ti, and Y in the vesicle-rich segregation are caused by magmatic evolution, as explained in the text.

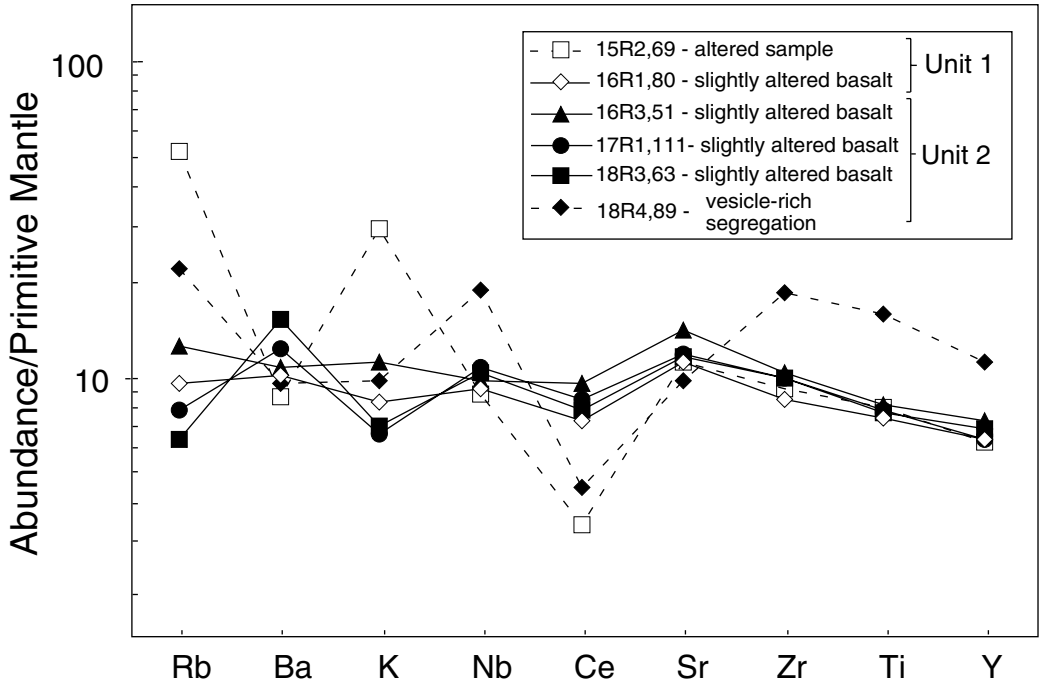

Figure F25. Variations of major and trace element abundances, plotted against depth in Units 1 and 2. **A.** Major elements. **B.** Trace elements. Open circles = samples from Unit 1; closed circles = samples from Unit 2. Depths are based on curated depth in mbsf and are calculated relative to the top of Unit 1.

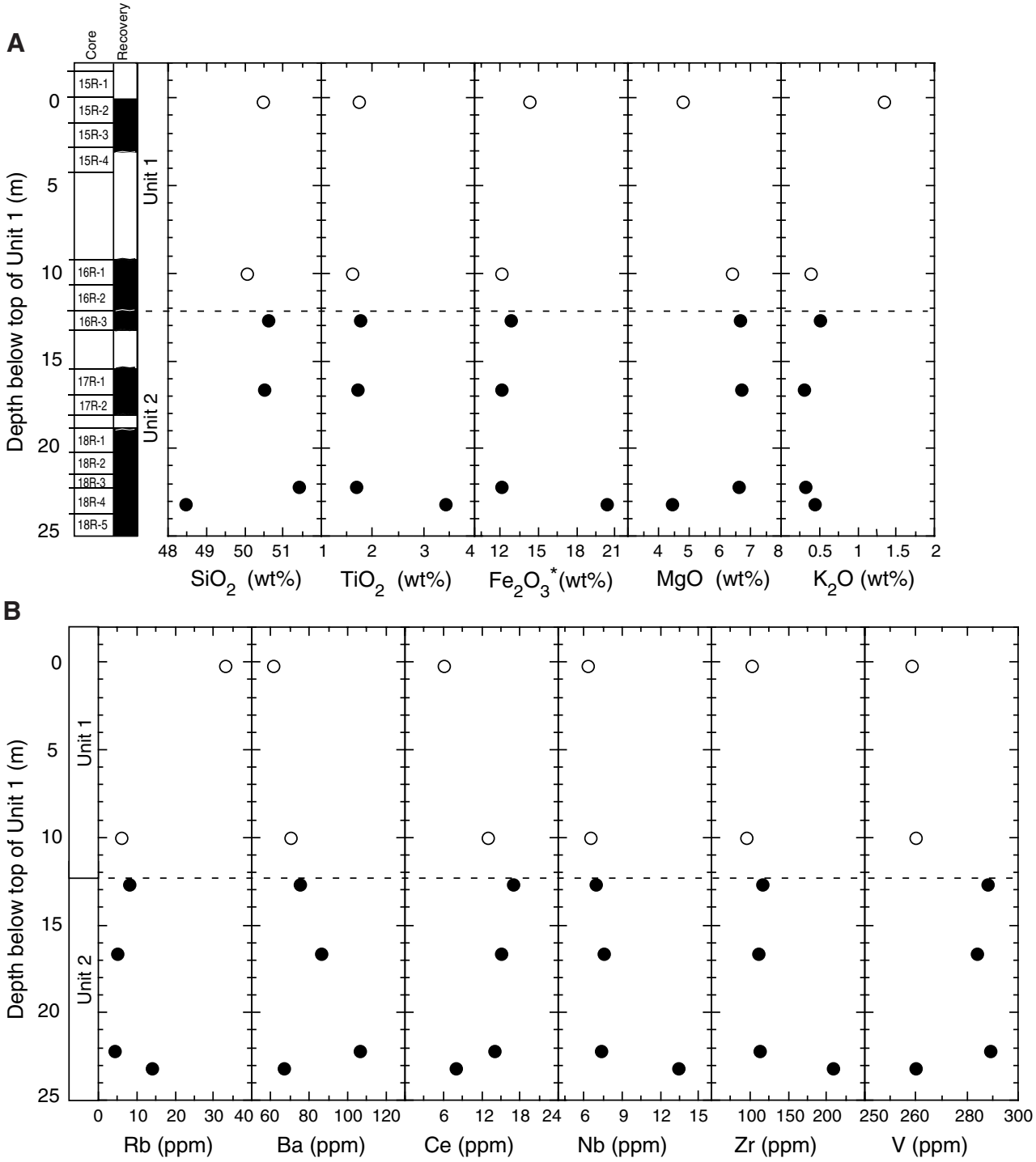

Figure F26. Trace element compositions of basalts from Hole 1136A, compared with those from other parts of the Kerguelen Plateau. Open symbols = samples from Unit 1; solid symbols = samples from Unit 2; circles = fresh samples; open square = Sample 183-1136A-15R-2 (Piece 2, 69–71 cm) (altered basalt); solid square = Sample 183-1136A-18R-4 (Piece 2, 89–92 cm) (vesicle-rich segregation). Data sources are Davies et al. (1989), Weis et al. (1989), Alibert (1991), Mehl et al. (1991), Salters et al. (1992), Storey et al. (1992), and Mahoney et al. (1995).

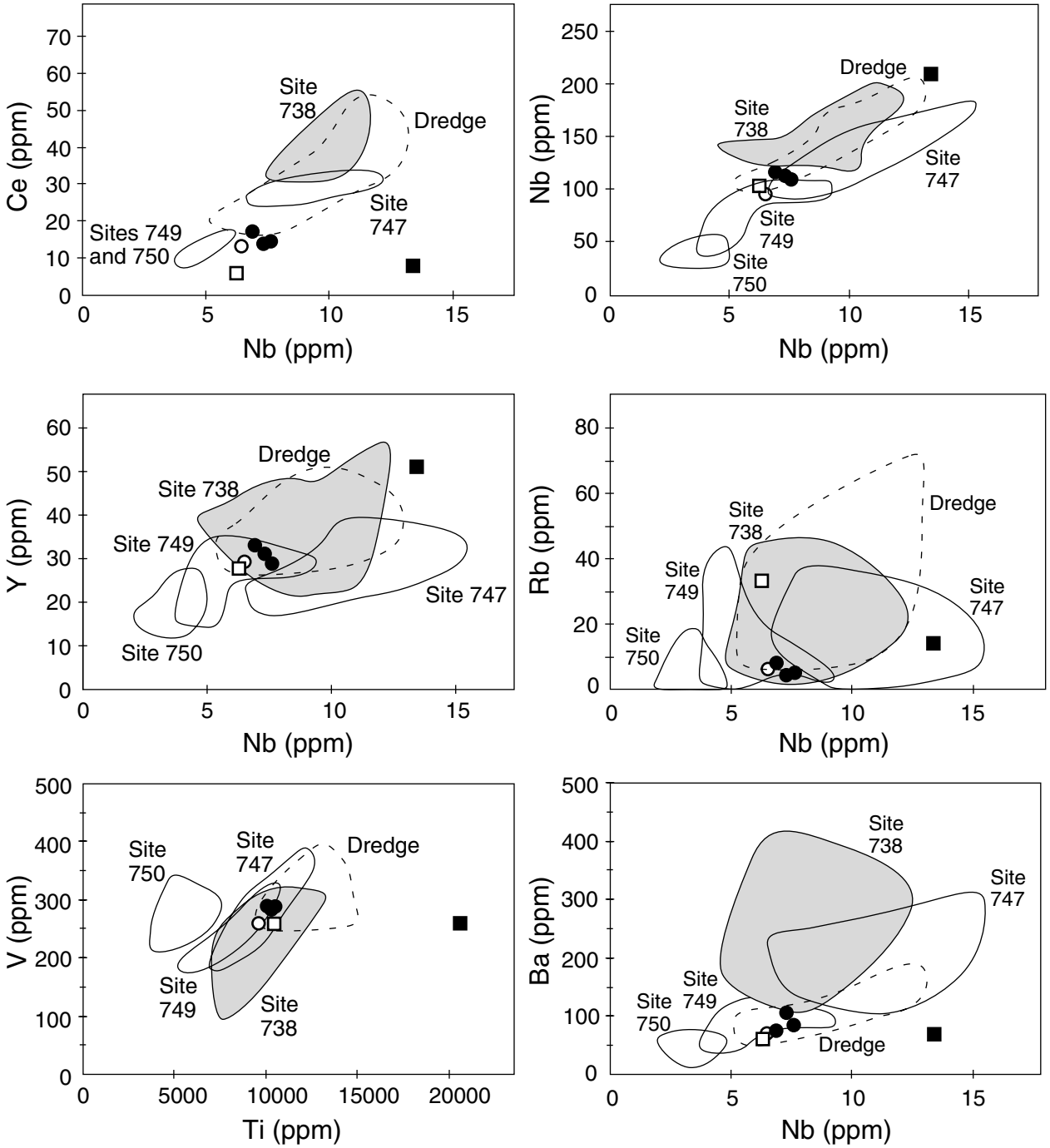

Figure F27. Zr/Ti, Nb/Zr, and Nb/Ce ratios vs. Zr/Y ratio or Zr content. These ratios are sensitive to the presence of a component from the continental crust and have been normalized to primitive mantle values. Note that basalts from Site 738, which are thought to contain a continental component (Mahoney et al., 1995), have the lowest Nb/Ce and Nb/Zr and highest Zr/Ti values. Basalts from Site 1136 most closely resemble the upper compositional group from Site 749. Subscript "N" indicates that ratios are normalized to primitive mantle abundances of Sun and McDonough (1989). Open symbols = samples from Unit 1; solid symbols = samples from Unit 2; circles = fresh samples; open square = Sample 183-1136A-15R-2 (Piece 2, 69–71 cm) (altered basalt); solid square = Sample 183-1136A-18R-4 (Piece 2, 89–92 cm) (vesicle-rich segregation). Data sources are Davies et al. (1989), Weis et al. (1989), Alibert (1991), Mehl et al. (1991), Salters et al. (1992), Storey et al. (1992), and Mahoney et al. (1995).

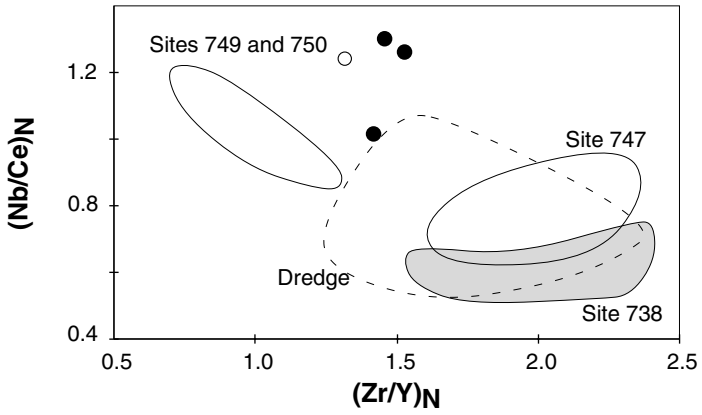

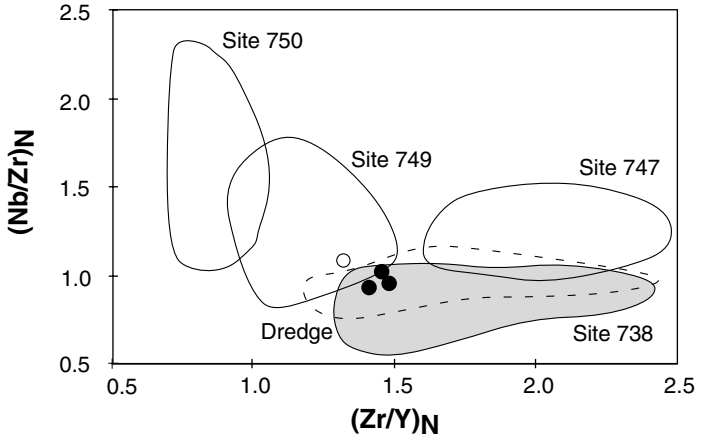

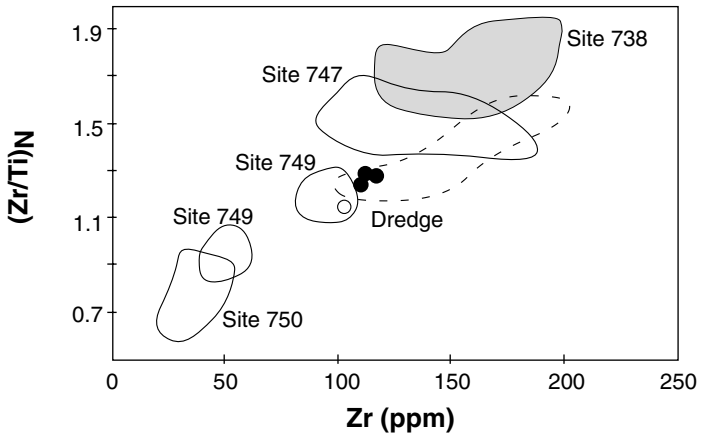

Figure F28. Distribution and abundance of secondary minerals as well as other alteration phenomena in Hole 1136A plotted against expanded depth. The expanded depth was calculated by multiplying the curated depth by the ratio of the recovered core to the interval penetrated. This was done to avoid the clustering of the plotted data at the top of each core caused by the incomplete recovery in a shallow basement penetration. Macroscopic features and mineral occurrences were recorded as observed in hand specimen from the core. The color is the hue of the bulk rock, with dark gray representing the "background" slightly altered basalts. The breccia column shows the distribution of clastic flow tops and tectonic breccias (absent from these cores). Late-stage oxidation (in percent) provides a measure of the extent of late-stage ferric oxide staining present throughout the core. The horizontal dashed lines indicate the igneous unit boundaries. Colors: Bl/Gn = blue-green, Gn = green, dk G = dark gray, Pk/B = pink/brown, Bk = black. Alteration: f = fresh, s = slight, m = moderate, h = high, c = complete. Breccia: V = volcanic flow top, T = tectonic. Mineral abundances of vesicles and veins: 0 = absent, t = trace, c = common, a = abundant.

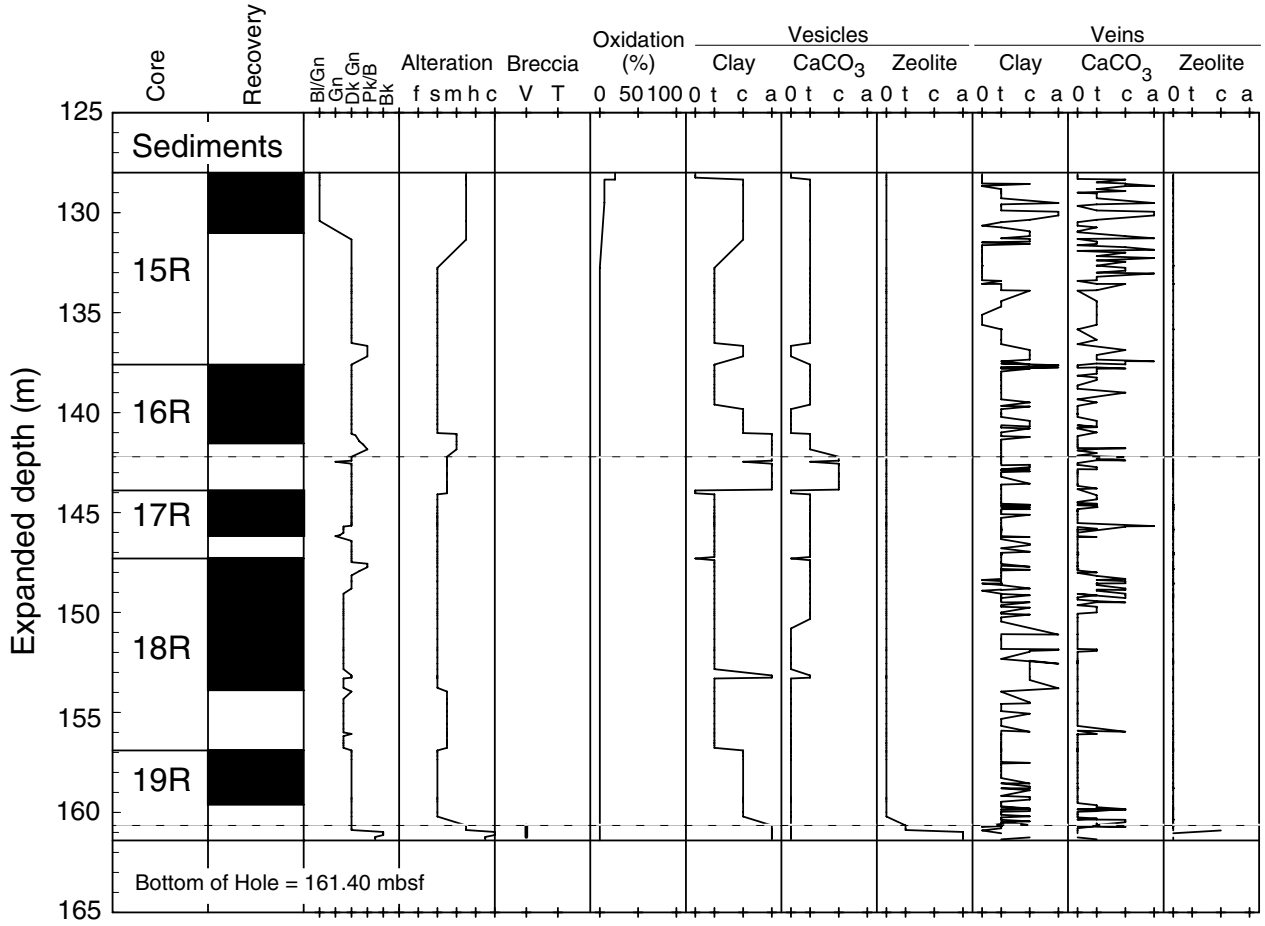

Figure F29. Color close-up photograph of Sample 183-1136A-15R-2 (Piece 1B, 33–41 cm) showing a moderately dipping multiple generation clay + calcite vein. Blue-green celadonite displaces spalled-off slivers of wall rock that are partially to completely altered to celadonite and/or Mg-saponite. The earlier portions of the veins are highly disrupted and recemented with calcite. A ~1-cm-wide diffuse oxidation halo is developed along the margins of the vein.

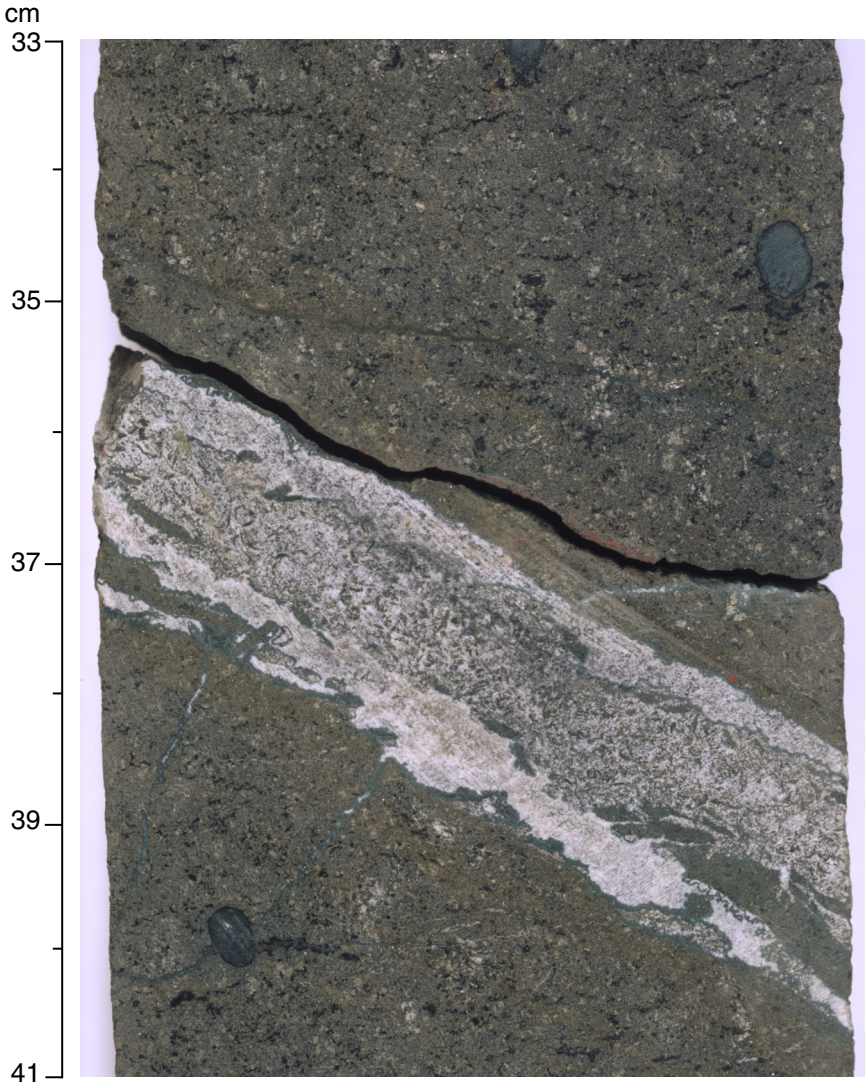

Figure F30. Color close-up photograph of Sample 183-1136A-15R-2 (Piece 1B, 47–62 cm) displaying similar alteration to Figure F29, p. 63. Thin strips of dark green clay replace the host wall rock. Brecciated wall-rock clasts within the vein are partially altered to brown clays. Vesicles have an outer margin of zeolite (calcite?), an inner lining of celadonite, and are infilled with calcite.

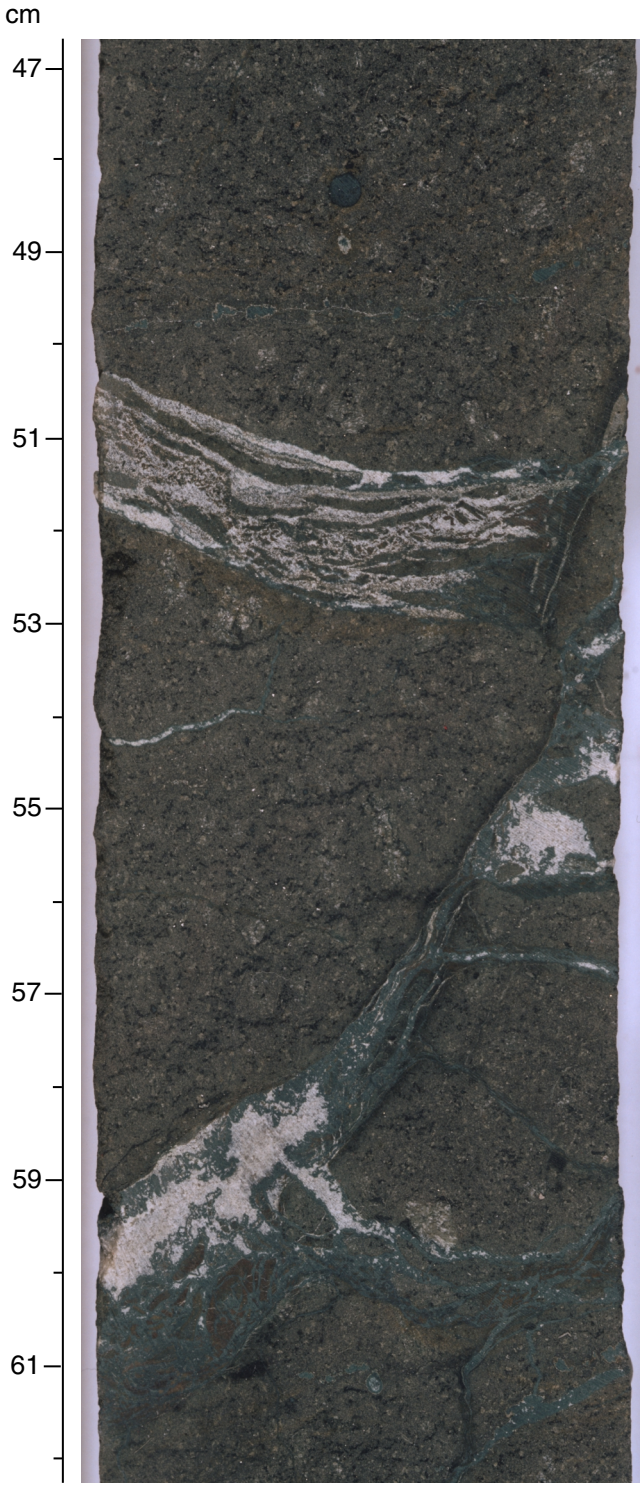

Figure F31. Color close-up photograph of Sample 183-1136A-19R-2 (Pieces 9 to 12, 117–140 cm) showing vesicle-rich glassy flow top of Unit 3. Glass and mesostasis are completely altered to black waxy saponite with late-stage zeolites filling wispy veinlets and vesicles.

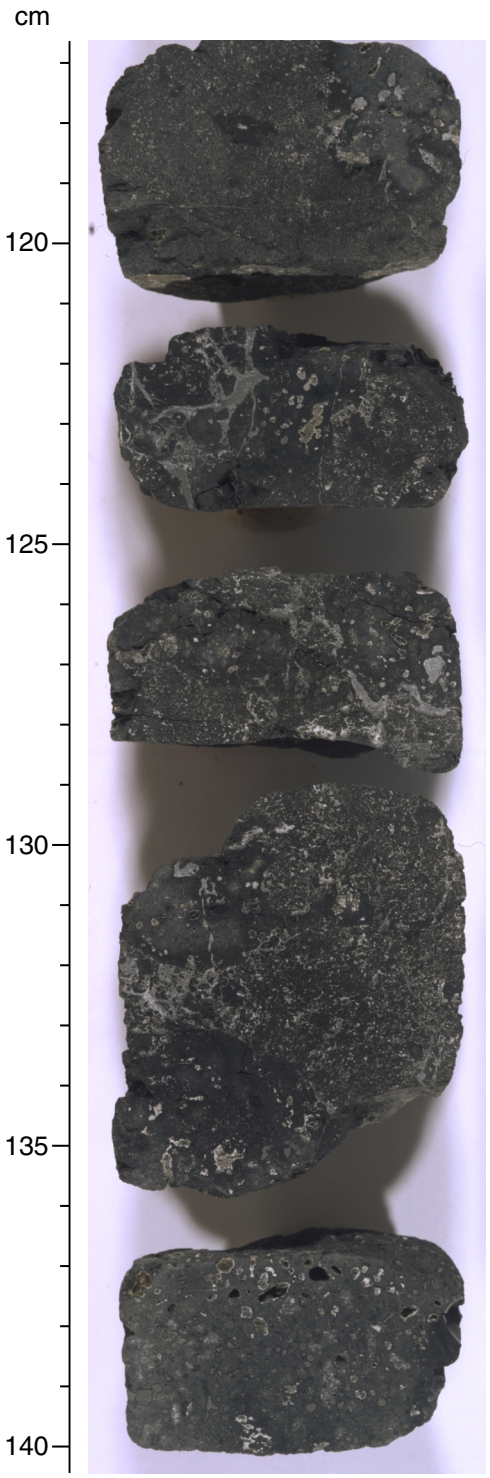

Figure F32. Distribution of clay- and calcium carbonate-filled veins with depth (mbsf) in Hole 1136A. Note that we calculated the abundance of veins by summing the total thickness (vein width) of each vein type for each core divided by the meters of core actually recovered. Only 45 cm of brecciated volcanic glass, completely altered to black clay, was recovered from Unit 3. These rocks are crosscut by numerous fine zeolite-filled veinlets (see **"Alteration and Weathering,"** p. 20).

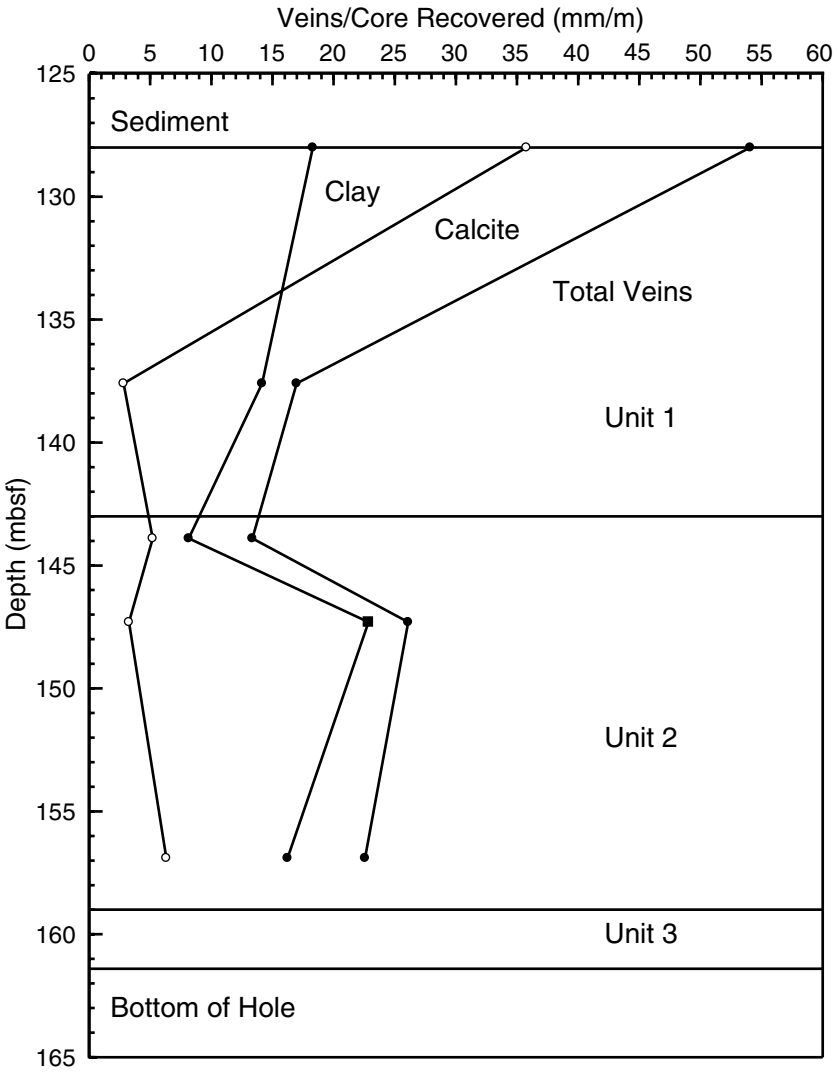

Figure F33. Frequency distribution of the true dips of veins from basaltic host rocks in Hole 1136A.

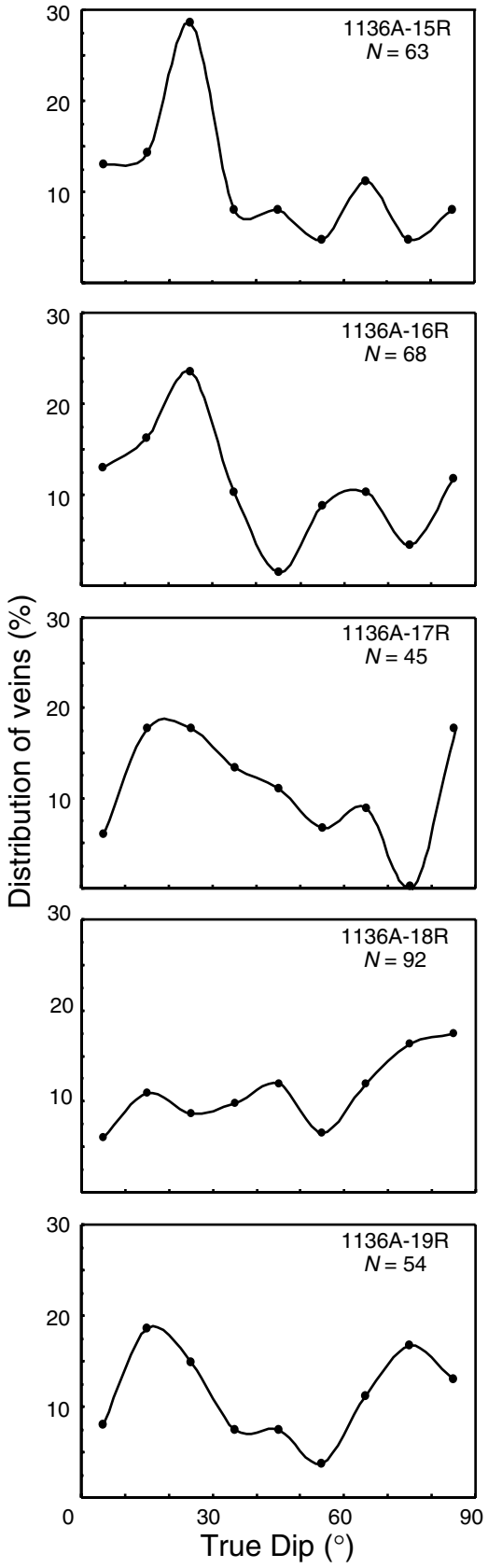

Figure F34. Dips within flows in 1136A. True dips of internal lava structures that are normally subhorizontal are plotted against depth.

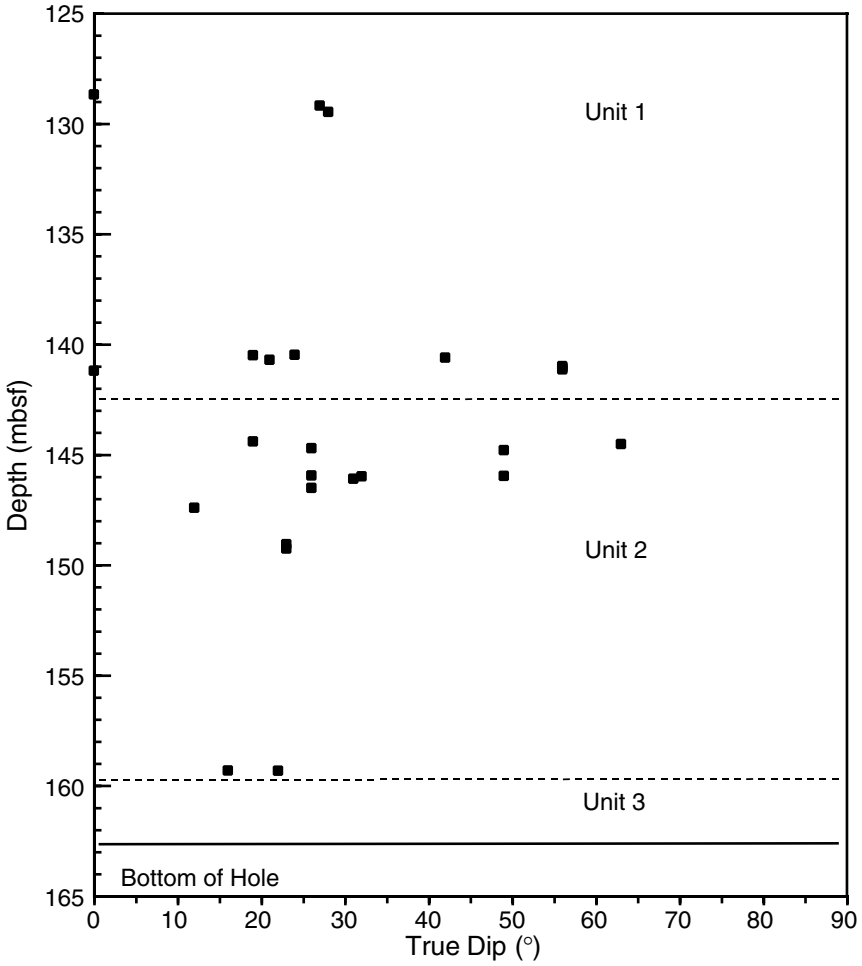

Figure F35. Examples of progressive AF demagnetization of discrete sediment samples from Hole 1136A. The directional change caused by AF demagnetization is plotted on orthogonal vector projections (right). Magnetic directions that tend toward the origin are considered reliable. Intensity changes are plotted on the left. J_0 is the magnetization intensity before AF treatment.

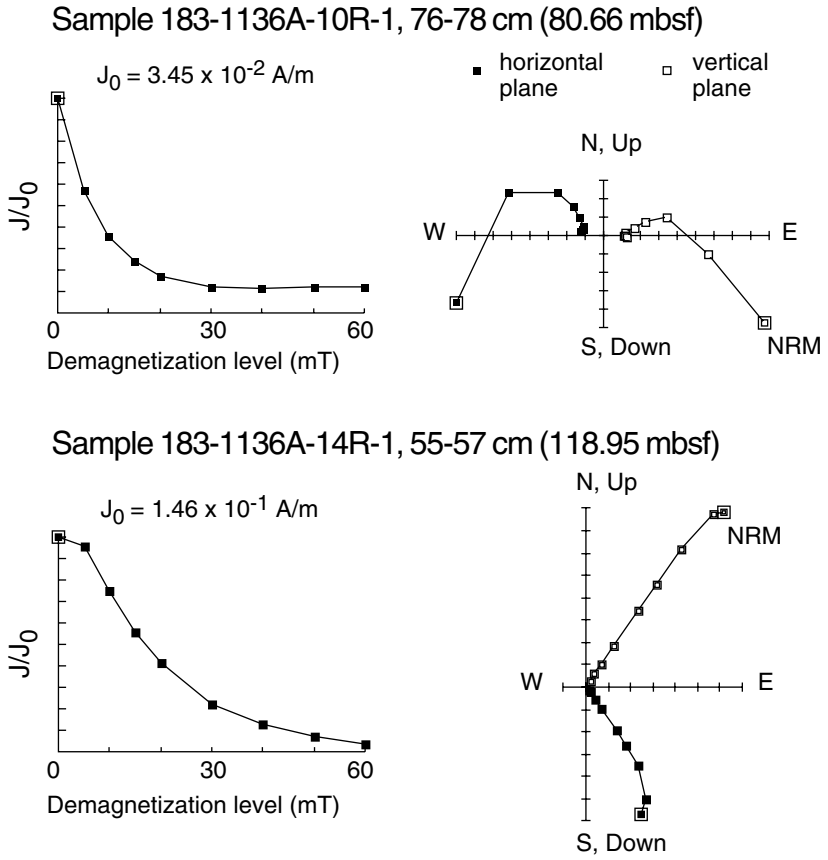

Figure F36. Inclination, intensity of remanent magnetization, and MST susceptibility of Hole 1136A sediments vs. depth. Crosses and lines represent remanent magnetization before and after AF demagnetization at 20 mT, respectively. Selected inclination data (see **"Paleomagnetism,"** p. 23) used for polarity interpretations are shown by open circles. Interpreted normal and reversed geomagnetic chrons are shown by black and white rectangles, respectively. Inclinations from discrete samples are shown by solid circles. Lithologic units are shown on the right.

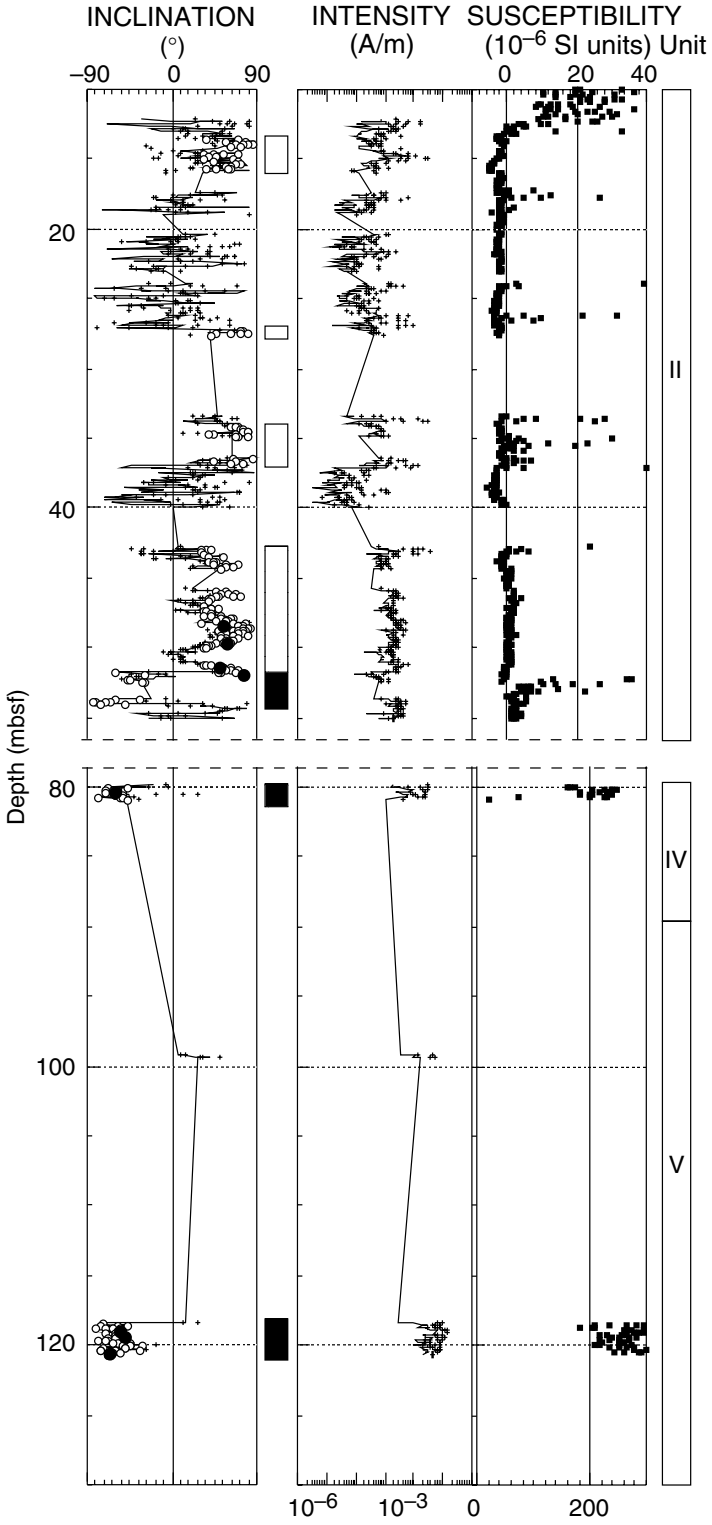

Figure F37. Inclination, intensity of remanent magnetization, and susceptibility of Hole 1136A basement rocks vs. depth. Crosses and lines represent remanent magnetization before and after AF demagnetization at 40 mT, respectively. NRM and characteristic inclinations (see **"Paleomagnetism,"** p. 23) obtained from discrete samples are shown by solid and open circles, respectively. MST, AMST, and discrete-sample susceptibilities are shown by lines, crosses, and open circles, respectively. Basement units are shown on the right.

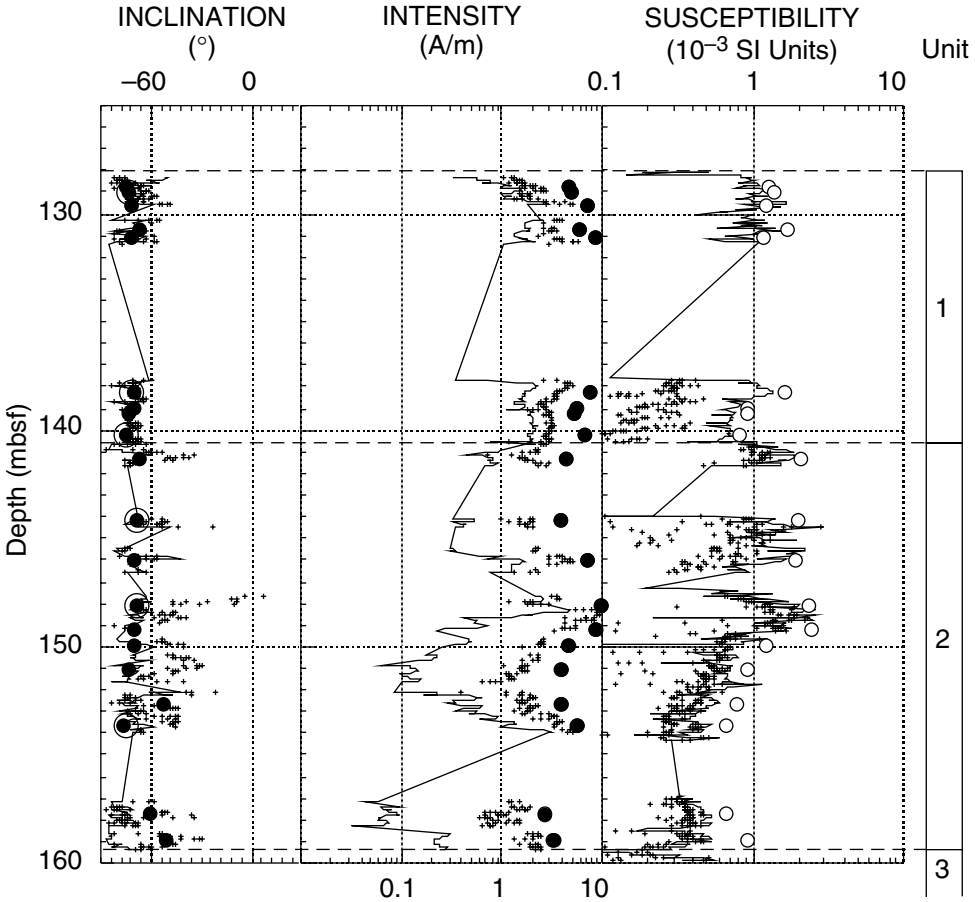

Figure F38. Example of stepwise AF demagnetization up to 60 mT of a discrete sample from basement Unit 2. The straight lines in the orthogonal vector projections indicate that this sample possesses a single-component magnetization. The sample has an inclination of –69°. J_0 is the magnetization intensity before AF treatment.

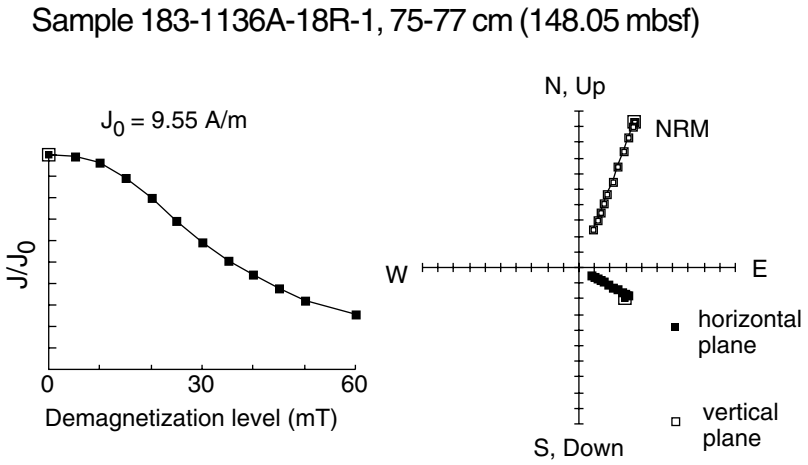

Figure F39. A. Thermal demagnetization of Sample 183-1136A-16R-2, 116–118 cm, from basement Unit 1. The NRM is a stable single-component magnetization. Most unblocking temperatures are above 500°C. The decay curve gives no indication of a second magnetic phase. The magnetic mineral is most likely magnetite, which has a Curie temperature of 580°C. **B.** Thermal demagnetization of Sample 183-1136A-18R-5, 132–134 cm. Most unblocking temperatures are below 300°C. This indicates (titano)maghemite as the magnetic mineral. The increase of normalized susceptibility at 300°C indicates a change of minerals, probably from (titano)maghemite to magnetite. (Titano)maghemite results from low-temperature oxidation of basalt. **C.** Thermal demagnetization of Sample 183-1136A-17R-1, 22–24 cm. The constantly decreasing intensity of magnetization at all temperatures indicates both magnetite and titanomaghemite as the magnetic minerals. The NRM is a stable, single-component magnetization. Gradually increasing susceptibility after 300°C indicates a change from titanomaghemite to magnetite. J_0 is the magnetization intensity before thermal treatment.

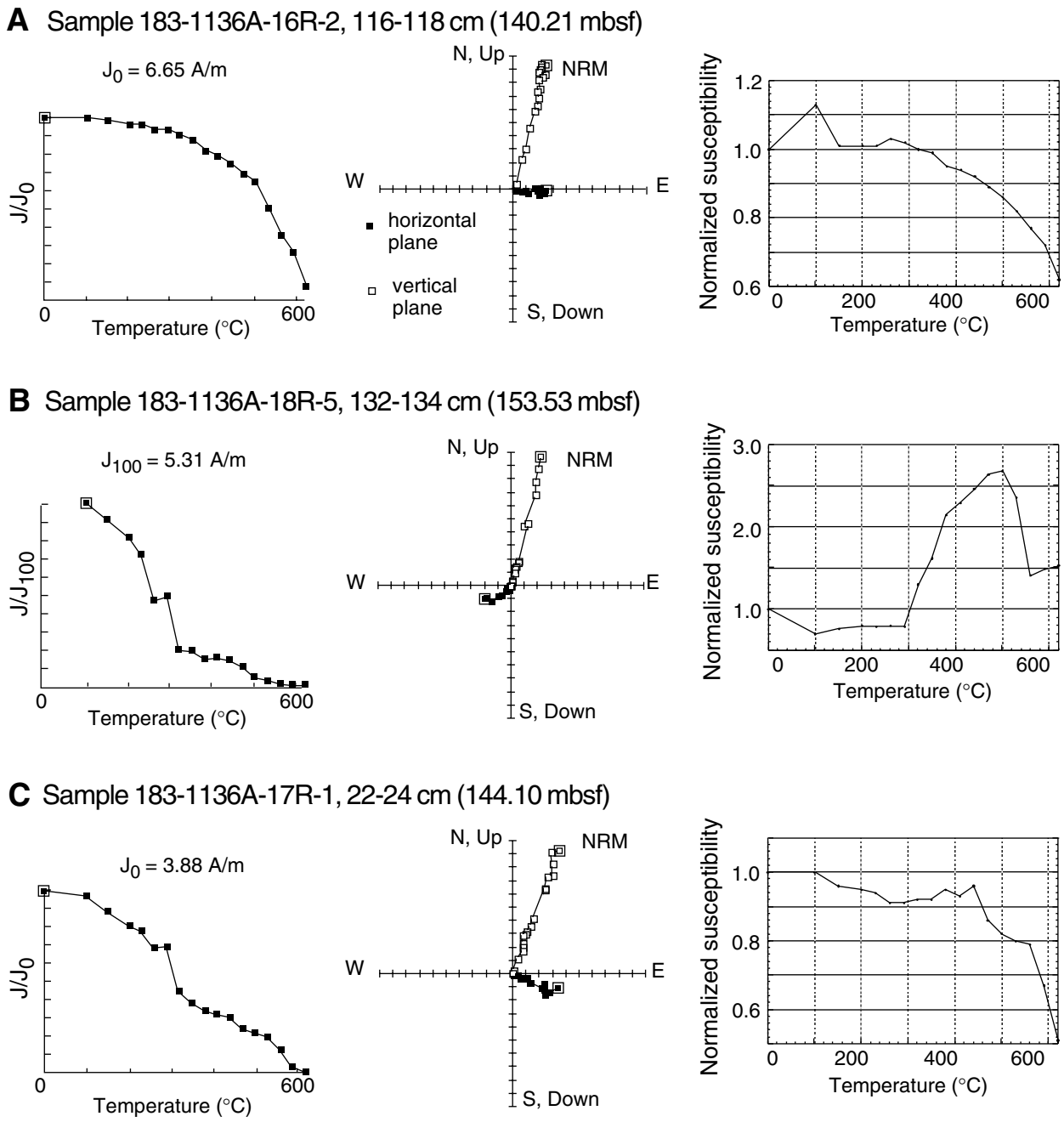

Figure F40. Directional anisotropy data from 20 Hole 1136A discrete basement samples plotted on an equal-area stereographic projection. The directions of maximum principal axes are plotted as triangles, of intermediate principal axes as gray squares, and of minimum principal axes as black squares. The minimum axes are grouped at an inclination of 90°, and the maximum and intermediate directions lie within a girdle 90° from the minima.

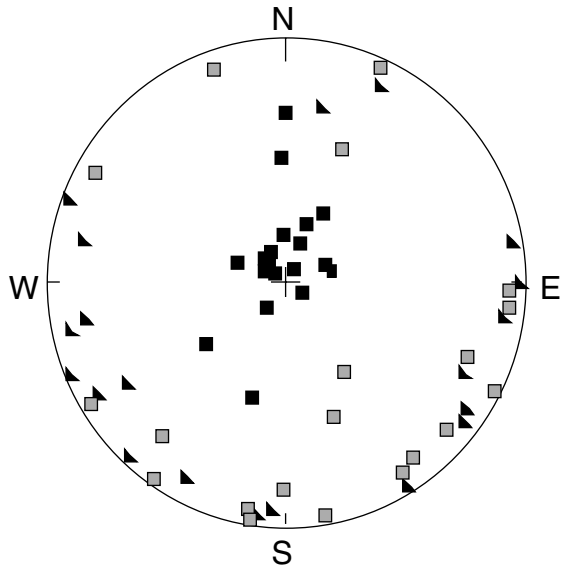

Figure F41. Downhole index properties of (A) bulk density, (B) grain density, and (C) porosity and (D) velocities at Site 1136. Velocities measured in x, y, or z direction are presented by circles, triangles, and squares, respectively. Open symbols = measurements on split cores. Solid symbols = measurements on cut samples. Lithology units to the far right.

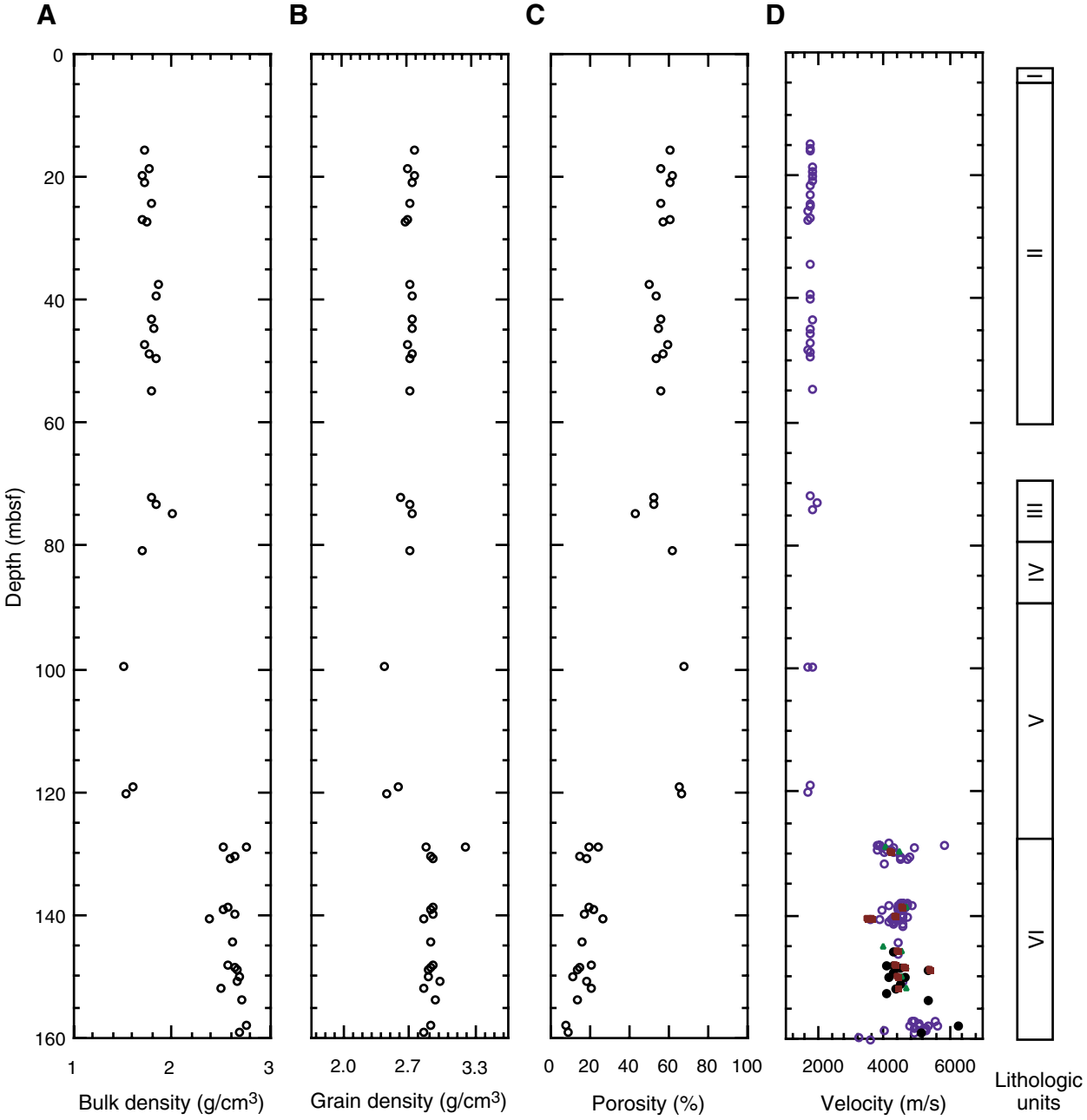

Figure F42. Downhole profiles of whole-core measurements of (**A**) magnetic susceptibility, (**B**) natural gamma ray, and (**C**) GRAPE bulk density from Site 1136. The lines on the GRAPE bulk density graph are the visually estimated maximum GRAPE bulk density. Lithology units to the far right.

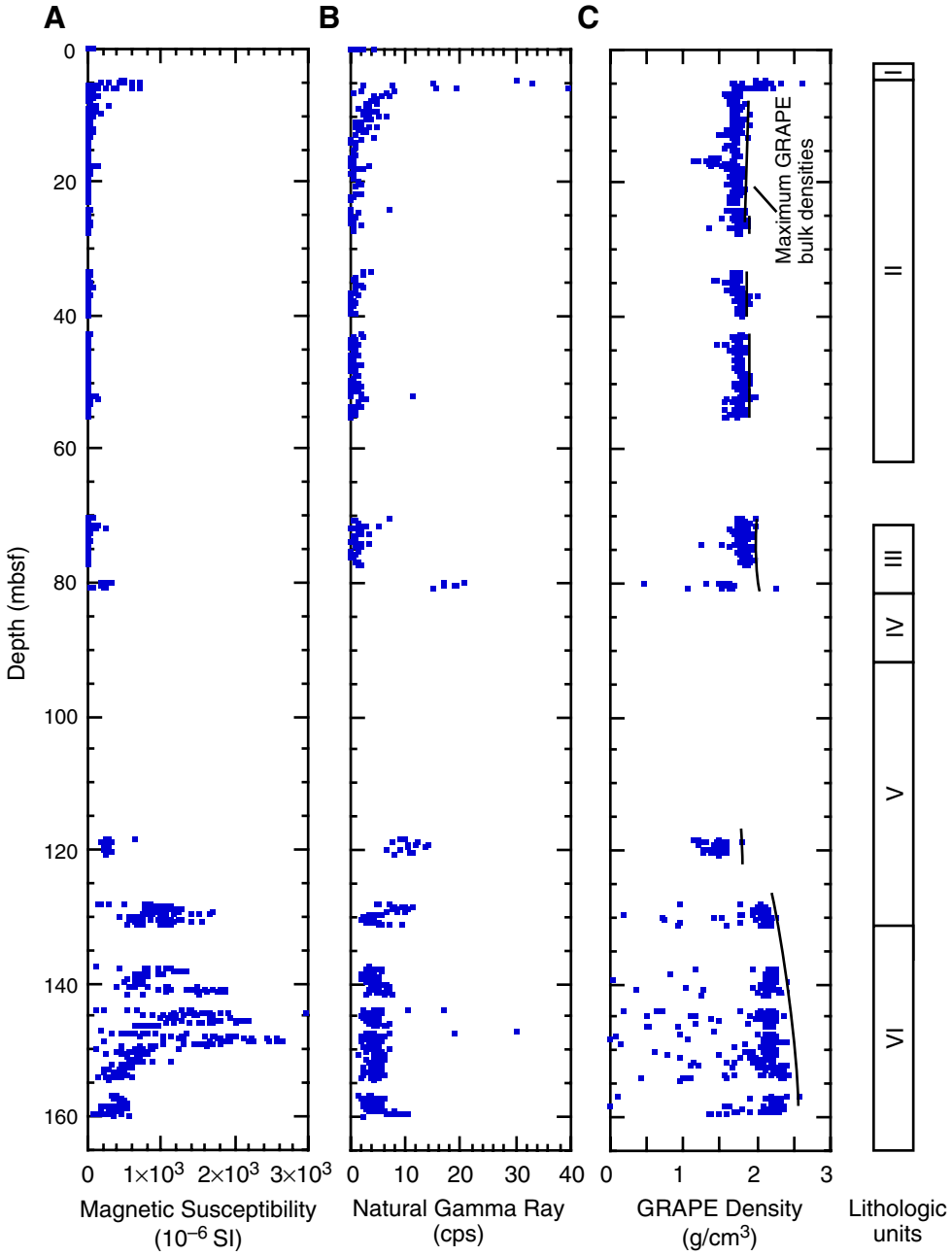

Figure F43. Summary of physical properties determinations in basaltic basement of Hole 1136A including (**A**) magnetic susceptibility, (**B**) bulk density, (**C**) grain density, (**D**) porosity, and (**E**) velocities determined in x, y, or z direction (presented by circles, triangles, and squares, respectively). Open symbols = results from split cores. Solid symbols = results from cut samples. Unit boundary is indicated by horizontal line. Lithologic units and core numbers are shown on the right.

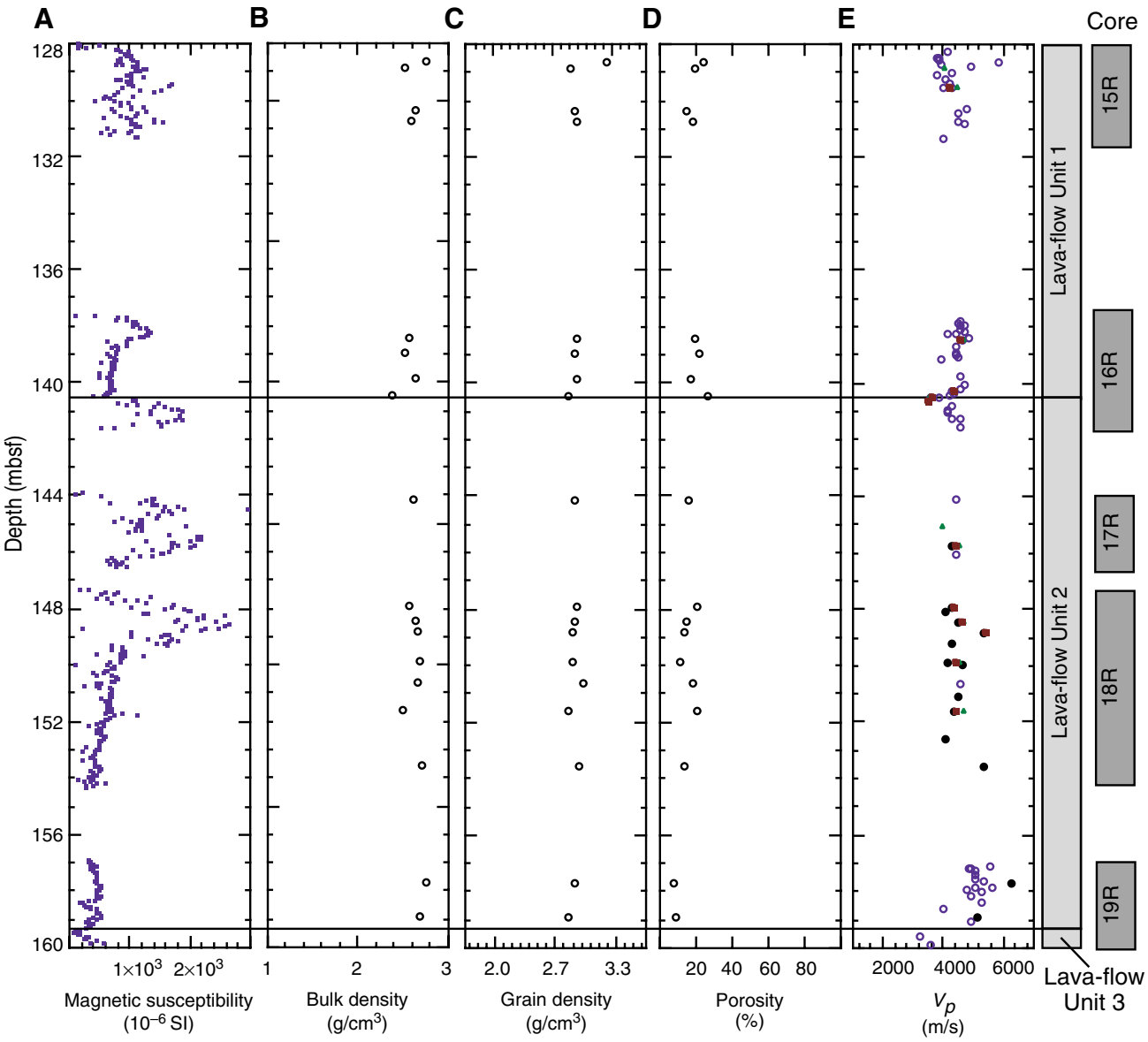

Figure F44. Comparison of densities determined from core samples, gamma-ray attenuation porosity evaluator, multisensor track, and compressional wave velocities from downhole logs and core samples from Hole 1136A (see **"Physical Properties,"** p. 26). Raw and robust mode filtered data are shown.

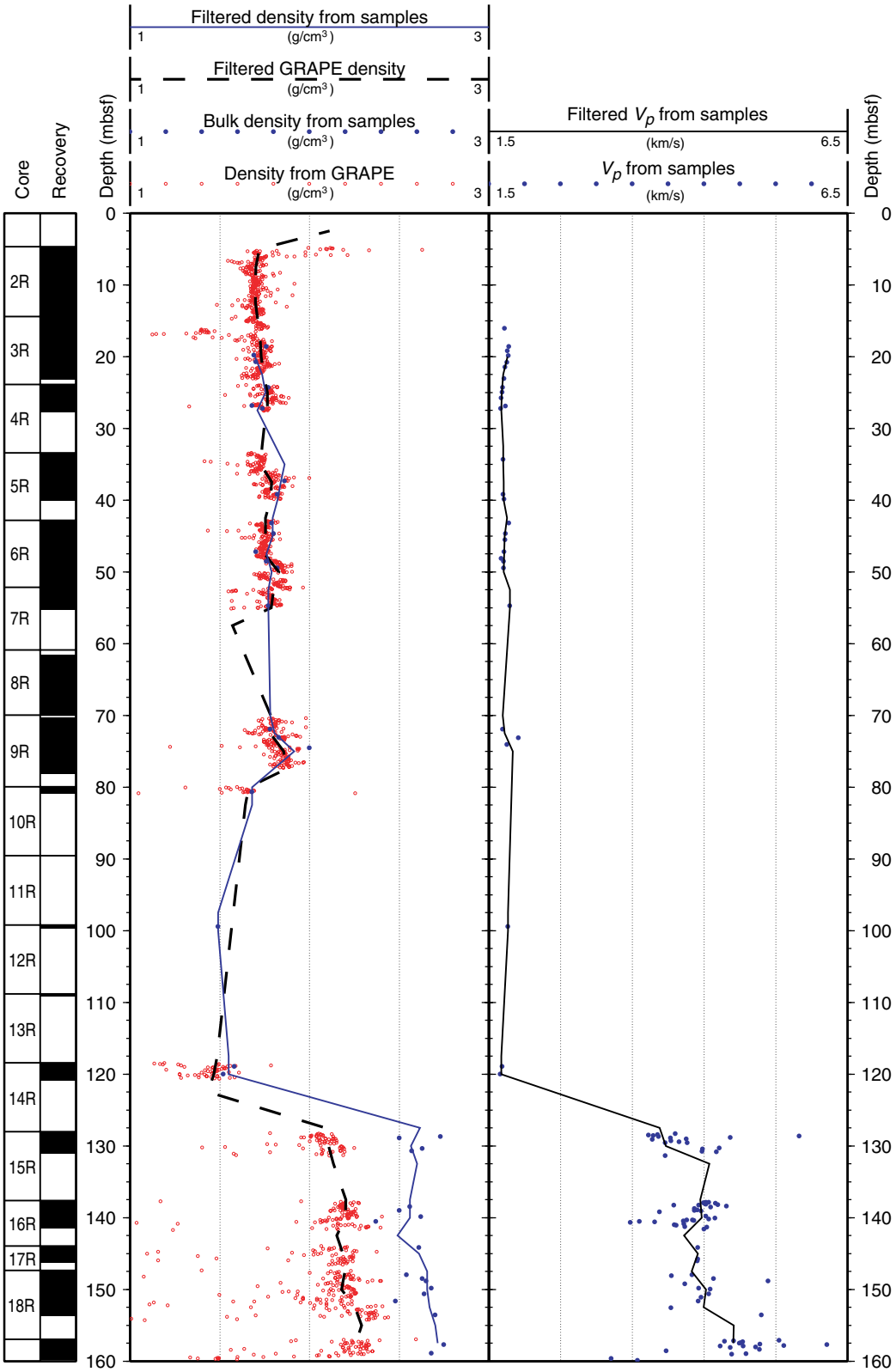

Figure F45. Composite of core recovery, lithostratigraphy, and age (on left) and (**A**) density and velocity as a function of depth, (**B**) density and velocity as a function of two-way traveltime (TWT), (**C**) impedance, (**D**) reflection coefficients without interbed multiples and transmission losses, and (**E**) a synthetic seismogram based on (D) as a function of TWT. sbsf = seconds below seafloor.

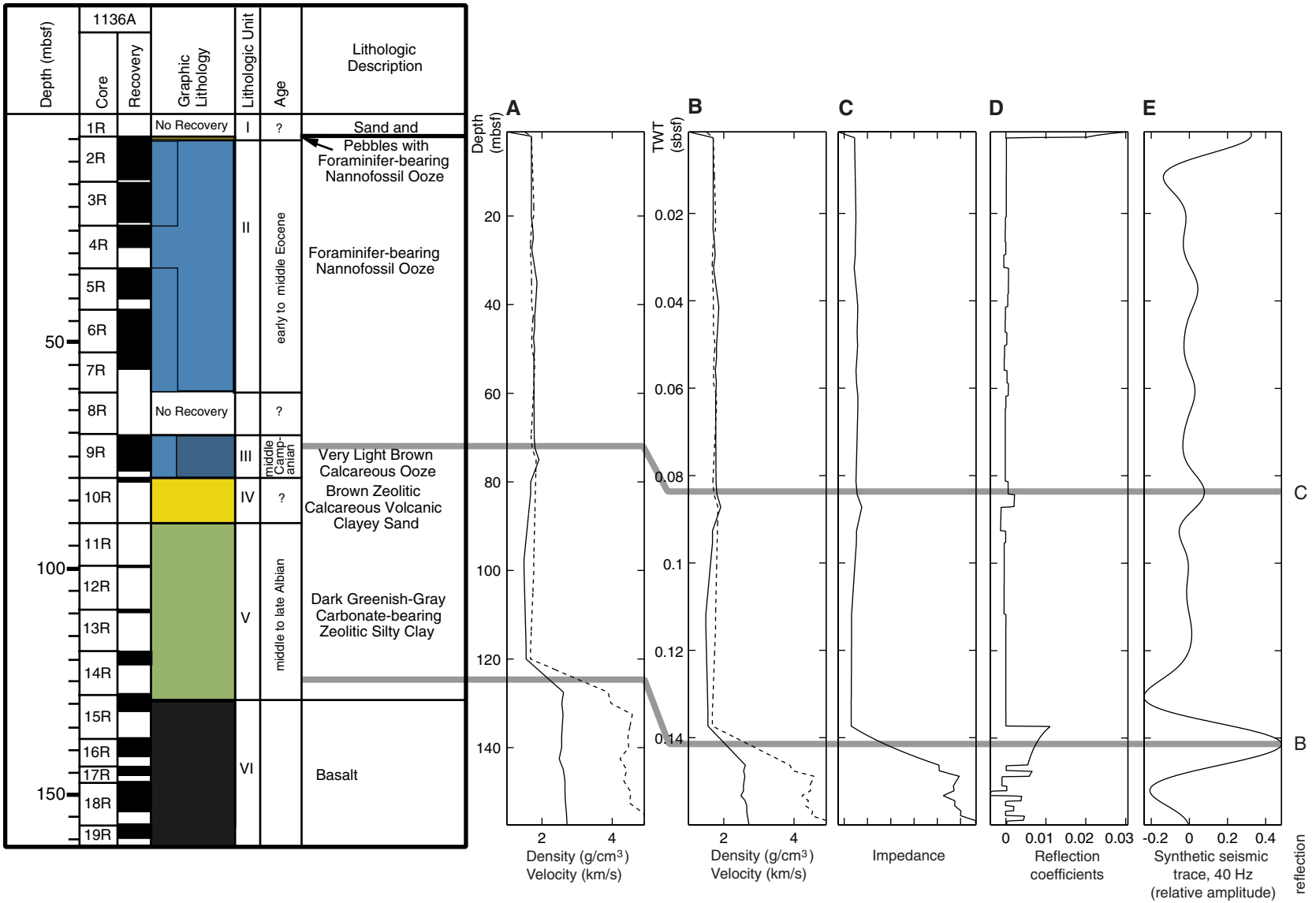

Figure F46. A portion of seismic reflection line 10 from *Marion Dufresne* cruise 47 across Site 1136, and a 1-D synthetic seismic trace from Figure F45, p. 79. Reflections correlated to the synthetic seismogram are labeled. C = mid-Campanian, B = top of basement. The vertical exaggeration is ~6.67 at the seafloor.

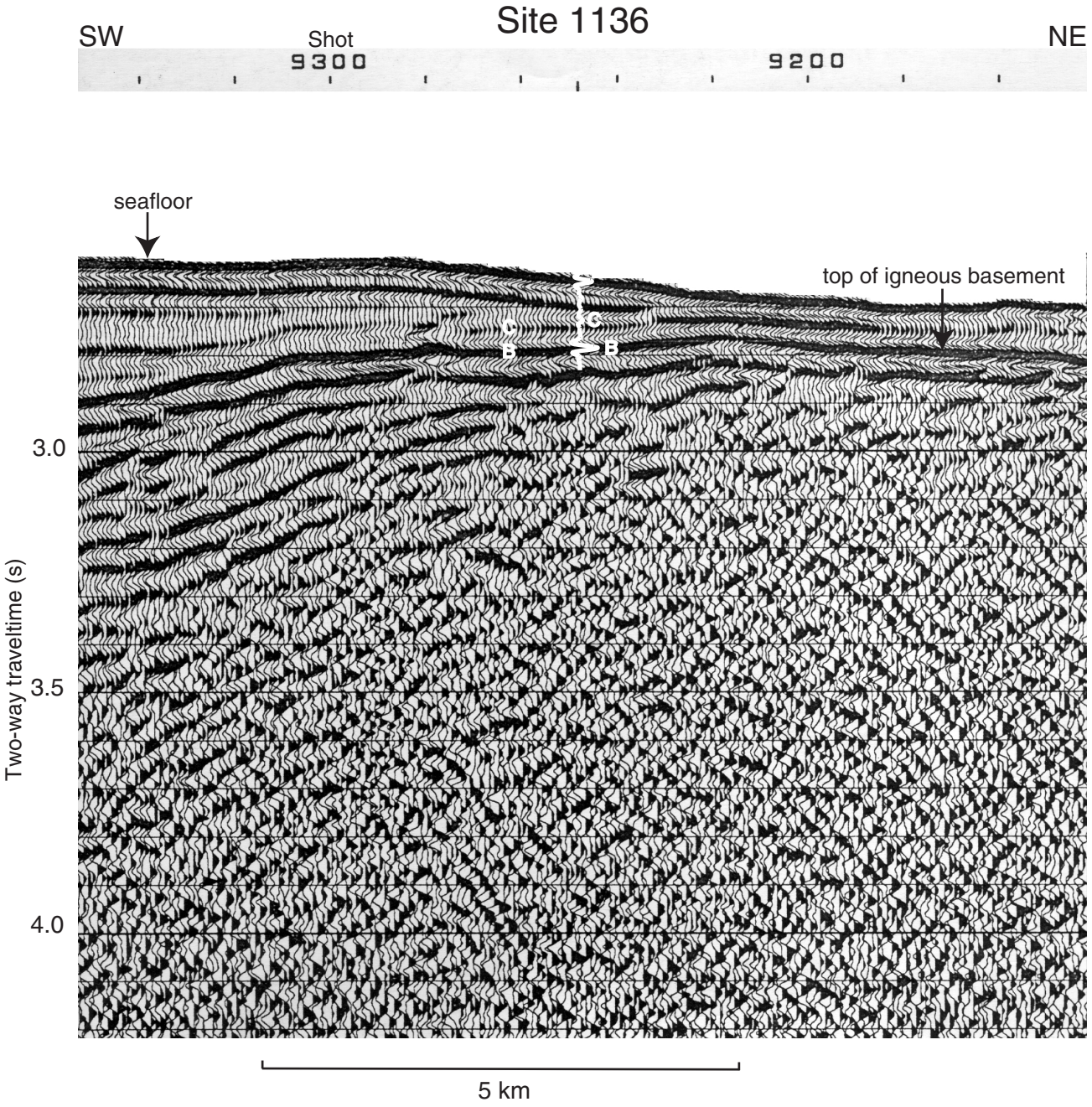

Table T1. Coring summary for Site 1136.

Core	Date (Dec 1998)	Time (UTC)	Depth (mbsf)	Length cored (m)	Length recovered (m)	Recovery (%)
183-1136A-						
1R	27	0615	0.0-4.7	4.7	0.00	0.0
2R	27	0715	4.7-14.4	9.7	9.65	99.5
3R	27	0745	14.4-23.9	9.5	8.81	92.7
4R	27	0835	23.9-33.4	9.5	3.84	40.4
5R	27	0915	33.4-42.8	9.4	6.68	71.1
6R	27	1000	42.8-52.1	9.3	9.72	104.5
7R	27	1045	52.1-60.9	8.8	3.26	37.0
8R	27	1140	60.9-70.3	9.4	0.00	0.0
9R	27	1220	70.3-79.9	9.6	7.93	82.6
10R	27	1330	79.9-89.5	9.6	1.00	10.4
11R	27	1425	89.5-99.2	9.7	0.10	1.0
12R	27	1530	99.2-108.8	9.6	0.49	5.1
13R	27	1615	108.8-118.4	9.6	0.28	2.9
14R	27	1710	118.4-128.0	9.6	2.41	25.1
15R	27	2110	128.0-137.6	9.6	2.98	31.0
16R	28	0315	137.6-143.9	6.3	3.88	61.6
17R	28	0640	143.9-147.3	3.4	2.34	68.8
18R	28	1520	147.3-156.9	9.6	6.35	66.1
19R	28	2000	156.9-161.4	4.5	2.83	62.9
Totals:				161.4	72.55	44.9

Note: This table is also available in **ASCII format.**

Table T2. Expanded coring summary for Hole 1136A. (See table notes. Continued on next page.)

Core	Date (Dec 1998)	Time (UTC)	Depth (mbsf)	Length (m) Cored	Length (m) Recovered	Recovery (%)	Section	Length (m) Liner	Length (m) Curated	Section depth (mbsf)	Catwalk samples	Comment
183-1136A-												
1R	27	0615	0.0-4.7	4.7	0.0	0.0						
2R	27	0715	4.7-14.4	9.7	9.65	99.5						
							1	1.50	1.50	4.7-6.2		
							2	1.50	1.50	6.2-7.7		
							3	1.50	1.50	7.7-9.2		
							4	1.50	1.50	9.2-10.7		
							5	1.50	1.50	10.7-12.2		
							6	1.50	1.50	12.2-13.7	HS	
							7	0.50	0.50	13.7-14.2		
							CC(w/7)	0.15	0.15	14.2-14.35	PAL	
								9.65	9.65			
3R	27	0745	14.4-23.9	9.5	8.81	92.7						
							1	1.50	1.50	14.4-15.9		
							2	1.50	1.50	15.9-17.4		
							3	1.50	1.50	17.4-18.9		
							4	1.50	1.50	18.9-20.4		
							5	1.50	1.50	20.4-21.9	HS	
							6	1.17	1.17	21.9-23.07		
							CC(w/6)	0.14	0.14	23.07-23.21	PAL	
								8.81	8.81			
4R	27	0835	23.9-33.4	9.5	3.84	40.4						
							1	1.50	1.50	23.9-25.4		
							2	1.50	1.50	25.4-26.9		
							3	0.69	0.69	26.9-27.59	HS	
							CC(w/3)	0.15	0.15	27.59-27.74	PAL	
								3.84	3.84			
5R	27	0915	33.4-42.8	9.4	6.68	71.1						
							1	1.50	1.50	33.4-34.9		
							2	1.50	1.50	34.9-36.4		
							3	1.50	1.50	36.4-37.9		
							4	1.50	1.50	37.9-39.4		
							5	0.50	0.50	39.4-39.9	HS	
							CC(w/5)	0.18	0.18	39.9-40.08	PAL	
								6.68	6.68			
6R	27	1000	42.8-52.1	9.3	9.72	104.5						
							1	1.50	1.50	42.8-44.3		
							2	1.50	1.50	44.3-45.8		
							3	1.50	1.50	45.8-47.3		
							4	1.50	1.50	47.3-48.8		
							5	1.50	1.50	48.8-50.3	HS	
							6	1.50	1.50	50.3-51.8		
							7	0.60	0.60	51.8-52.4		
							CC(w/7)	0.12	0.12	52.4-52.52	PAL	
								9.72	9.72			
7R	27	1045	52.1-60.9	8.8	3.26	37.0						
							1	1.50	1.50	52.1-53.6		
							2	1.51	1.51	53.6-55.11	HS	
							CC(w/CC)	0.25	0.25	55.11-55.36		
								3.26	3.26			
8R	27	1140	60.9-70.3	9.4	0.0	0.0						
9R	27	1220	70.3-79.9	9.6	7.93	82.6						
							1	1.00	1.00	70.3-71.3		
							2	1.50	1.50	71.3-72.8		
							3	1.50	1.50	72.8-74.3		
							4	1.50	1.50	74.3-75.8	HS	
							5	1.50	1.50	75.8-77.3		
							6	0.88	0.88	77.3-78.18		
							CC(NS)	0.05	0.05	78.18-78.23	PAL	All to PAL
								7.93	7.93			
10R	27	1330	79.9-89.5	9.6	1.0	10.4						
							1	1.00	1.00	79.9-80.9	PAL, HS	
								1.00	1.00			
11R	27	1425	89.5-99.2	9.7	0.1	1.0						

Table T2 (continued).

Core	Date (Dec 1998)	Time (UTC)	Depth (mbsf)	Length (m) Cored	Length (m) Recovered	Recovery (%)	Section	Length (m) Liner	Length (m) Curated	Section depth (mbsf)	Catwalk samples	Comment
							CC(w/CC)	0.10	0.10	89.5-89.6	PAL	
								0.10	0.10			
12R	27	1530	99.2-108.8	9.6	0.49	5.1						
							1	0.28	0.28	99.2-99.48	HS	
							CC(w/1)	0.21	0.21	99.48-99.69	PAL	
								0.49	0.49			
13R	27	1615	108.8-118.4	9.6	0.28	2.9						
							1	0.23	0.16	108.8-108.96	HS	
							CC(NS)	0.05	0.05	108.96-109.01	PAL	All to PAL
								0.28	0.21			
14R	27	1710	118.4-128	9.6	2.41	25.1						
							1	1.50	1.50	118.4-119.9		
							2	0.71	0.71	119.9-120.61	HS	
							CC(w/2)	0.20	0.20	120.61-120.81	PAL	
								2.41	2.41			
15R	27	2110	128-137.6	9.6	2.98	31.0						
							1	1.03	0.20	128.0-128.2		
							2	0.77	1.39	128.2-129.59		
							3	1.18	1.47	129.59-131.06		
							4	0.00	0.31	131.06-131.37		
								2.98	3.37			
16R	28	0315	137.6-143.9	6.3	3.88	61.6						
							1	1.38	1.46	137.6-139.06		
							2	1.47	1.50	139.06-140.56		
							3	1.03	1.16	140.56-141.72		
								3.88	4.12			
17R	28	0640	143.9-147.3	3.4	2.34	68.8						
							1	0.88	1.48	143.9-145.38		
							2	1.46	1.20	145.38-146.58		
								2.34	2.68			
18R	28	1520	147.3-156.9	9.6	6.35	66.1						
							1	1.49	1.38	147.3-148.68		
							2	1.47	1.30	148.68-149.98		
							3	1.43	0.81	149.98-150.79		
							4	1.48	1.44	150.79-152.23		
							5	0.48	1.50	152.23-153.73		
							6	0.00	0.66	153.73-154.39		
								6.35	7.09			
19R	28	2000	156.9-161.4	4.5	2.83	62.9						
							1	1.52	1.54	156.9-158.44		
							2	1.31	1.49	158.44-159.93		
								2.83	3.03			
			Totals:	161.4	72.55	45.0						

Notes: UTC = Universal Time Coordinated. CC = core catcher (number in parenthesis indicates which section the core catcher is stored with), NS = all of the core catcher was used for paleontology sample. HS = headspace gas sample, PAL = paleontology sample. This table is also available in **ASCII format.**

Table T3. Summary of lithologic units at Site 1136.

Unit	Core interval	Depth (mbsf)	Thickness (m)	Age	Lithology	Interpretation
I	2R-1, 0 cm, to 2R-1, 118 cm	4.70-5.88	1.18	Pleistocene	Mixed sediment	Pelagic ooze with ice-rafted debris (from drilling)
II	2R-1, 118 cm, to 7R-CC, 25 cm	5.88-60.90	55.02	early to middle Eocene	Foraminifer-bearing nannofossil ooze	Pelagic sediment
III	9R-1, 0 cm, to 9R-CC, 5 cm	70.30-79.90	9.60	mid-Campanian	Very light brown calcareous ooze	Pelagic and hemipelagic sediment with volcanic material
IV	10R-1, 0 cm, to 10R-1, 100 cm	79.90-89.50	9.60	mid- to late Albian	Brown calcareous zeolitic volcanic clayey sand	Mixed biogenic and altered volcanic sand deposited in neritic environment
V	11R-1, 0 cm, to 15R-1, 8 cm	89.50-128.08	38.58	mid- to late Albian	Dark greenish-gray carbonate-bearing zeolitic silty clay	Mixed biogenic and altered volcanic sand deposited in neritic environment
VI	15R-1, 8 cm, to 19R-2, 149 cm	128.08-161.40	33.32	mid- to late Albian	Basalt	Lava flows

Table T4. X-ray diffraction results and calcium carbonate contents expressed as $CaCO_3$ for Hole 1136A.

Unit	Core, section, interval (cm)	Depth (mbsf)	Minerals	$CaCO_3$ (wt%)
II				
	183-1136A-			
	2R-1, 90	5.60	Calcite	92
	3R-1, 90	15.30	Calcite	95
	4R-1, 89	24.79	Calcite	95
	5R-1, 90	34.30	Calcite	95
	6R-1, 90	43.70	Calcite	95
	7R-1, 106	53.16	Calcite	89
III				
	183-1136A-			
	9R-1, 53	70.83	Calcite, (quartz)	92
IV				
	183-1136A-			
	10R-1, 25	80.15	Calcite, clinoptilolite, heulandite, glauconite, nontronite, plagioclase, glass	NA
	10R-1, 63	80.53	Calcite, clinoptilolite, heulandite, glauconite, nontronite, plagioclase, glass	NA
V				
	183-1136A-			
	12R-1, 9	99.29	Calcite, clinoptilolite, heulandite, glauconite, nontronite, plagioclase, lawsonite(?), glass	12
	14R-1, 74	119.14	Calcite, clinoptilolite, heulandite, glauconite, glass, plagioclase (?)	18

Note: NA = not analyzed, ( ) = minor amount. See **"Organic and Inorganic Geochemistry,"** p. 29.

Table T5. Summary of Hole 1136A volcaniclastic components.

Lithologic Unit	Core interval	Depth (mbsf)	Thickness (m)	Age	Lithologies with volcanic components	Volcanic components	Authigenic and secondary minerals
III	9R-1, 0 cm, to 9R-CC, 5 cm	70.30-79.90	9.60	early Santonian to Cenomanian	Very light brown foraminifer-bearing calcareous ooze	<5% silt-sized palagonitized basaltic glass shards	Trace of Fe smectite clay minerals (nontronite?)
IV	10R-1, 0 cm, to 10R-1, 100 cm	79.90-89.50	9.60	Cenomanian to early Albian	Brown zeolitic calcareous volcanic clayey sand	10–15% silt to fine sand-sized palagonitized basaltic glass shards	Zeolites (clinoptilolite, heulandite), Fe smectite (nontronite), glauconite
V	11R-1, 0 cm, to 15R-1, 5 cm	89.50-133.00	43.50	early Albian	Dark greenish gray carbonate-bearing zeolitic silty clay	<5% silt-sized palagonitized basaltic glass shards	Zeolites (clinoptilolite, heulandite), Fe smectite (nontronite), glauconite

Table T6. Location of three lava-flow units in Hole 1136A.

Basement unit	Core, section, interval (cm) Top	Bottom	Curated depths (mbsf)	Recovered thickness (m)	Estimated original thickness (m)
	183-1136A-				
1	15R-1, 8	16R-2, 150	128.08-140.56	6.22	~12
2	16R-3, 0	19R-2, 93	140.56-159.37	13.28	~18
3	19R-2, 93	19R-2, 149	159.37-159.93	0.53	>2

Table T7. Major and trace element data.

Leg, hole, core, section:	183-1136A-15R-2,	183-1136A-16R-1,	183-1136A-16R-3,	183-1136A-17R-1,	183-1136A-18R-3,	183-1136A-18R-4,
Interval (cm):	69-71	80-82	51-53	111-117	63-65	89-92
Piece:	1C	3E	4	15	2	2
Unit:	1	1	2	2	2	2
Rock type:	Highly altered basalt	Slightly altered basalt	Slightly altered basalt	Slightly altered basalt	Slightly altered basalt	Vesicle-rich segregation
Depth (mbsf):	128.89	138.40	141.07	145.01	150.61	151.68
Major oxides (wt%):						
SiO_2	50.47	50.04	50.62	50.52	51.42	48.46
TiO_2	1.74	1.60	1.76	1.71	1.68	3.43
Al_2O_3	15.35	15.84	15.26	15.23	14.77	11.94
Fe_2O_3*	14.26	12.13	12.83	12.12	12.06	20.33
MnO	0.07	0.13	0.12	0.16	0.19	0.36
MgO	4.77	6.40	6.65	6.69	6.59	4.46
CaO	7.59	9.00	7.92	9.38	9.02	6.41
Na_2O	2.89	2.70	2.96	2.78	2.88	2.90
K_2O	1.34	0.38	0.51	0.30	0.32	0.44
P_2O_5	0.19	0.16	0.21	0.19	0.19	0.45
Total	98.65	98.37	98.82	99.07	99.11	99.17
LOI	1.80	1.40	2.10	0.90	1.10	0.90
Mg#	0.44	0.55	0.55	0.56	0.56	0.34
Trace elements (ppm):						
Rb	33	6	8	5	4	14
Ba	61	70	75	86	106	67
Sr	234	237	294	248	244	205
Ce	6	13	17	15	14	8
Nb	6.3	6.5	6.9	7.6	7.3	13.4
Zr	103	95	116	110	112	208
Y	28	29	33	29	31	51
V	258	260	288	284	289	260
Cr	172	176	155	156	142	2
Ni	70	66	66	61	59	26
Cu	27	138	106	127	113	212
Zn	132	100	104	98	101	152

Notes: * = total iron as Fe_2O_3. LOI = loss on ignition at 1025°C for 4 hr. Mg# = MgO/(MgO + FeO), mol%, with FeO calculated (as 80% of total Fe).

Table T8. Alteration minerals hosted by igneous rocks in Hole 1136A identified by X-ray diffraction.

Core, section, interval (cm)	Depth (mbsf)	Description	XRD identification
183-1136A-			
15R-1 (Piece 2, 8-14)	128.08	Highly altered basalt	Celadonite + saponite + nontronite
15R-2 (Piece 1B, 65-67)	128.85	Green clay in vein	Celadonite + saponite + nontronite
15R-2 (Piece 1D, 124-125)	129.44	Carbonate vein	Calcite
17R-1 (Piece 8, 78-79)	144.68	Green clay in coalesced vesicle	Saponite + nontronite
18R-1 (Piece 1, 61-63)	147.91	Carbonate in vesicle	Calcite
18R-3 (Piece 1C, 31-32)	150.29	Green clay in vein	Saponite + nontronite + quartz
18R-4 (Piece 1F, 85-86)	151.64	Green clay in vein	Saponite + nontronite illite
19R-1 (Piece 5L, 120-122)	158.10	Zeolite and clay in vein	Clinoptilolite + heulandite + saponite + nontronite
19R-2 (Piece 8, 106-108)	159.50	Zeolite and clay in vesicle	Clinoptilolite + heulandite + saponite + nontronite

Note: XRD = X-ray diffraction.

Table T9. Summary of natural remanent magnetization (NRM) intensity and susceptibility for Hole 1136A.

Unit		Average	Maximum	Minimum	Median
Sediment					
Unit II	NRM intensity	1.95×10^{-3}	3.33×10^{-2}	7.55×10^{-6}	9.39×10^{-4}
	Susceptibility	1.53×10^{-5}	7.24×10^{-4}	-5.80×10^{-6}	0.20×10^{-6}
Unit III	Susceptibility	1.69×10^{-5}	2.50×10^{-4}	4.00×10^{-6}	1.28×10^{-5}
Unit IV	NRM intensity	1.90×10^{-2}	3.26×10^{-2}	4.35×10^{-2}	1.91×10^{-2}
	Susceptibility	2.02×10^{-4}	3.18×10^{-4}	2.10×10^{-5}	2.16×10^{-4}
Unit V	NRM intensity	6.99×10^{-2}	1.49×10^{-1}	1.36×10^{-2}	6.33×10^{-2}
	Susceptibility	2.62×10^{-4}	6.31×10^{-4}	1.33×10^{-4}	2.62×10^{-4}
Hole 1136A sediment average					
	NRM intensity	8.34×10^{-3}	1.49×10^{-1}	7.55×10^{-6}	1.31×10^{-3}
	Susceptibility	2.96×10^{-5}	7.24×10^{-4}	-5.80×10^{-6}	1.20×10^{-6}
Basement					
Unit 1	NRM intensity	2.91	5.77	1.06	2.95
	Susceptibility	8.88×10^{-4}	1.69×10^{-3}	1.14×10^{-4}	8.44×10^{-4}
Unit 2	NRM intensity	2.55	1.00×10^{-1}	3.89×10^{-1}	2.06
	Susceptibility	9.13×10^{-4}	2.96×10^{-3}	9.55×10^{-5}	6.92×10^{-4}
Hole 1136A basement average					
	NRM intensity	2.69	1.00×10^{-1}	3.89×10^{-1}	2.36
	Susceptibility	9.05×10^{-4}	2.96×10^{-3}	9.55×10^{-5}	7.51×10^{-4}

Note: Units for NRM = (A/m), for susceptibility = (SI units).

Table T10. Characteristic inclinations and natural remanent magnetization intensities of discrete basalt samples, Hole 1136A.

Core, section, interval (cm)	Inclination (°)	NRM Intensity (Å/m)	Depth (mbsf)	Demagnetization range (°C or mT)
183-1136A-				
15R-2, 78-81	–73	4.79	128.97	TH 320-620
16R-1, 62-65	–72	7.56	138.22	AF 10-60
16R-2, 116-118	–76	6.65	140.21	TH 290-620
17R-1, 22-25	–70	3.88	144.10	TH 230-620
18R-1, 75-78	–69	9.55	148.05	AF 15-60
18R-5, 132-134	–75	5.31*	153.53	TH 320-620

Notes: Inclination = characteristic inclination determined from progressive demagnetization. Demagnetization range = demagnetization method and characteristic inclination is determined from the component in this range. TH = thermal demagnetization. AF = alternating field. * = after thermal demagnetization at 100°C.

Table T11. Index properties data from Site 1136.

Core, section, interval (cm)	Depth (mbsf)	Water content (wet%)	Water content (dry%)	Density			Porosity (%)	Void ratio
				Bulk (g/cm^3)	Dry (g/cm^3)	Grain (g/cm^3)		
183-1136A-								
3R-1, 117	15.57	36.2	56.7	1.71	1.09	2.75	60.4	1.52
3R-3, 113	18.53	32.4	47.8	1.76	1.19	2.67	55.5	1.25
3R-4, 86	19.76	37.0	58.7	1.69	1.07	2.75	61.2	1.57
3R-5, 30	20.70	36.0	56.2	1.70	1.09	2.70	59.7	1.48
4R-1, 35	24.25	31.9	46.9	1.77	1.21	2.69	55.2	1.23
4R-2, 143	26.83	36.9	58.5	1.68	1.06	2.67	60.4	1.53
4R-3, 28	27.18	33.0	49.3	1.74	1.16	2.64	56.0	1.27
5R-3, 88	37.28	27.4	37.7	1.86	1.35	2.68	49.7	0.99
5R-4, 122	39.12	30.0	42.9	1.82	1.27	2.72	53.3	1.14
6R-1, 32	43.12	31.5	46.0	1.79	1.23	2.72	55.0	1.22
6R-2, 29	44.59	30.7	44.2	1.80	1.25	2.71	53.9	1.17
6R-3, 133	47.13	35.4	54.8	1.70	1.10	2.68	58.9	1.43
6R-4, 119	48.49	32.8	48.9	1.76	1.18	2.71	56.3	1.29
6R-5, 59	49.39	29.7	42.2	1.82	1.28	2.70	52.7	1.11
7R-2, 105	54.65	31.8	46.7	1.77	1.21	2.70	55.1	1.23
9R-2, 57	71.87	29.9	42.7	1.78	1.25	2.60	52.1	1.09
9R-3, 23	73.03	29.1	41.1	1.83	1.29	2.70	52.0	1.08
9R-4, 17	74.47	22.0	28.1	2.00	1.56	2.72	42.8	0.75
10R-1, 68	80.58	37.2	59.2	1.68	1.05	2.69	60.9	1.55
12R-1, 17	99.37	46.0	85.3	1.49	0.80	2.42	66.8	2.02
14R-1, 45	118.85	41.7	71.4	1.58	0.92	2.58	64.3	1.80
14R-2, 6	119.96	44.1	78.9	1.52	0.85	2.45	65.4	1.89
15R-2, 44	128.64	8.9	9.8	2.73	2.49	3.27	23.7	0.31
15R-2, 67	128.87	7.9	8.6	2.50	2.30	2.86	19.4	0.24
15R-3, 75	130.34	5.6	5.9	2.63	2.48	2.90	14.3	0.17
15R-3, 109	130.68	7.3	7.8	2.57	2.38	2.92	18.2	0.22
16R-1, 80	138.40	7.7	8.4	2.56	2.36	2.92	19.2	0.24
16R-1, 134	138.94	8.7	9.5	2.50	2.29	2.90	21.2	0.27
16R-2, 75	139.81	6.6	7.0	2.62	2.44	2.94	16.8	0.20
16R-2, 140	140.46	11.0	12.4	2.37	2.11	2.83	25.5	0.34
17R-1, 20	144.10	6.2	6.7	2.61	2.45	2.91	15.9	0.19
18R-1, 61	147.91	8.0	8.7	2.54	2.34	2.92	19.8	0.25
18R-1, 114	148.44	5.6	5.9	2.63	2.48	2.90	14.3	0.17
18R-2, 10	148.78	5.0	5.3	2.65	2.51	2.89	12.9	0.15
18R-2, 114	149.82	4.1	4.2	2.68	2.57	2.88	10.6	0.12
18R-3, 63	150.61	6.9	7.4	2.64	2.46	2.99	17.8	0.22
18R-4, 80	151.59	8.2	8.9	2.48	2.28	2.84	19.8	0.25
18R-5, 130	153.53	4.9	5.1	2.70	2.57	2.94	12.8	0.15
19R-1, 77	157.67	2.9	2.9	2.75	2.68	2.90	7.7	0.08
19R-2, 45	158.89	3.1	3.2	2.68	2.60	2.83	8.1	0.09

Note: This table is also available in **ASCII format.**

Table T12. Compressional wave velocities determined using the Hamilton Frame, Site 1136.

Core, section, interval (cm)	Depth (mbsf)	Direction	Velocity (m/s)
183-1136A-			
3R-1, 44	14.84	LX	1691
3R-1, 118	15.58	LX	1703
3R-2, 8	15.98	LX	1722
3R-3, 112	18.52	LX	1780
3R-4, 21	19.11	LX	1757
3R-4, 87	19.77	LX	1772
3R-5, 33	20.73	LX	1751
3R-5, 101	21.41	LX	1725
3R-6, 108	22.98	LX	1716
4R-1, 36	24.26	LX	1691
4R-1, 106	24.96	LX	1689
4R-2, 32	25.72	LX	1672
4R-2, 144	26.84	LX	1734
4R-3, 29	27.19	LX	1669
5R-1, 90	34.30	LX	1702
5R-4, 123	39.13	LX	1699
5R-5, 41	39.81	LX	1716
6R-1, 33	43.13	LX	1779
6R-2, 30	44.60	LX	1730
6R-2, 114	45.44	LX	1728
6R-3, 133	47.13	LX	1714
6R-4, 74	48.04	LX	1673
6R-4, 119	48.49	LX	1710
6R-5, 59	49.39	LX	1710
7R-2, 105	54.65	LX	1791
9R-2, 58	71.88	LX	1691
9R-3, 25	73.05	LX	1914
9R-3, 122	74.02	LX	1755
12R-1, 18	99.38	LX	1768
12R-1, 18	99.38	LX	1673
14R-1, 45	118.85	LX	1690
14R-2, 6	119.96	LX	1662
15R-2, 6	128.26	X	4103
15R-2, 23	128.43	X	3851
15R-2, 26	128.46	X	3724
15R-2, 33	128.53	X	3793
15R-2, 37	128.57	X	5826
15R-2, 49	128.69	X	3867
15R-2, 58	128.78	X	4868
15R-2, 66	128.86	CY	4036
15R-2, 78	128.98	X	4254
15R-2, 84	129.04	X	3778
15R-2, 104	129.24	X	4038
15R-2, 118	129.38	X	4150
15R-2, 129	129.49	CY	4470
15R-2, 129	129.49	CZ	4169
15R-2, 132	129.52	X	3957
15R-2, 133	129.53	X	4266
15R-2, 133	129.53	X	4266
15R-3, 68	130.27	X	4712
15R-3, 84	130.43	X	4483
15R-3, 112	130.71	X	4473
15R-3, 121	130.80	X	4672
15R-4, 27	131.33	X	3958
16R-1, 18	137.78	X	4525
16R-1, 20	137.80	X	4566
16R-1, 25	137.85	X	4491
16R-1, 30	137.90	X	4505
16R-1, 32	137.92	X	4657
16R-1, 46	138.06	X	4525
16R-1, 54	138.14	X	4692
16R-1, 62	138.22	X	4078
16R-1, 63	138.23	X	4427
16R-1, 75	138.35	X	4813
16R-1, 84	138.44	X	4596
16R-1, 84	138.44	CY	4673
16R-1, 84	138.44	CZ	4555
16R-1, 109	138.69	X	4368
16R-1, 128	138.88	X	4409
16R-1, 134	138.94	X	4368
16R-1, 141	139.01	X	4459
16R-2, 9	139.15	X	3882
16R-2, 67	139.73	X	4524
16R-2, 93	139.99	X	4654
16R-2, 108	140.14	X	4568
16R-2, 118	140.24	X	4260
16R-2, 122	140.28	CZ	4343
16R-2, 128	140.34	X	4357
16R-2, 134	140.40	X	4212
16R-2, 141	140.47	CX	3564
16R-2, 141	140.47	CY	3532
16R-2, 141	140.47	CZ	3601
16R-2, 144	140.50	X	3813
16R-3, 6	140.62	Z	3473
16R-3, 21	140.77	X	4220
16R-3, 38	140.94	X	4084
16R-3, 47	141.03	X	4112
16R-3, 66	141.22	X	4234
16R-3, 70	141.26	X	4541
16R-3, 97	141.53	X	4498
17R-1, 21	144.11	X	4411
17R-1, 113	145.03	Y	3945
17R-2, 38	145.76	CX	4234
17R-2, 38	145.76	CY	4537
17R-2, 38	145.76	CZ	4415
17R-2, 64	146.02	X	4404
18R-1, 62	147.92	CX	4233
18R-1, 62	147.92	CY	4341
18R-1, 62	147.92	CZ	4333
18R-1, 76	148.06	MX	4047
18R-1, 115	148.45	CX	4472
18R-1, 115	148.45	CY	4660
18R-1, 115	148.45	CZ	4636
18R-2, 11	148.79	CX	5313
18R-2, 11	148.79	CY	5362
18R-2, 11	148.79	CZ	5390
18R-2, 52	149.20	MX	4231
18R-2, 115	149.83	CX	4092
18R-2, 115	149.83	CY	4535
18R-2, 115	149.83	CZ	4426
18R-2, 124	149.92	MX	4587
18R-3, 62	150.60	X	4566
18R-4, 25	151.04	MX	4459
18R-4, 81	151.60	CX	4335
18R-4, 81	151.60	CY	4684
18R-4, 81	151.60	CZ	4423
18R-5, 33	152.56	MX	4037
18R-5, 131	153.54	MX	5301
19R-1, 16	157.06	X	5547
19R-1, 24	157.14	X	4911
19R-1, 28	157.18	X	4786
19R-1, 36	157.26	X	5042
19R-1, 51	157.41	X	5010
19R-1, 59	157.49	X	4993
19R-1, 69	157.59	X	5281
19R-1, 78	157.68	MX	6211
19R-1, 89	157.79	X	5612
19R-1, 94	157.84	X	5048
19R-1, 98	157.88	X	4727
19R-1, 108	157.98	X	5221
19R-1, 119	158.09	X	4864
19R-1, 144	158.34	X	5272
19R-2, 12	158.56	X	3970
19R-2, 46	158.90	MX	5088
19R-2, 56	159.00	X	4889
19R-2, 113	159.57	X	3205
19R-2, 140	159.84	X	3572

Notes: The directions of the velocity determined are represented by X (into the core), Y (across the core), and Z (along the core). Type of samples is denoted by prefix; M = oriented minicore, C = oriented cubes, L = split core in line, and no prefix = split core sections without core liner. This table is also available in **ASCII format.**

Table T13. Thermal conductivity values for Site 1136.

Core, section, interval (cm)	Depth (mbsf)	Thermal conductivity (W/[m·K])
183-1136A-		
4R-2, 75	26.15	1.199
5R-3, 75	37.15	1.258
6R-4, 75	48.05	1.213
15R-3, 117–127	130.76	2.022
16R-2, 13–23	139.19	1.531
17R-2, 72–83	146.10	1.832
18R-2, 71–81	149.39	1.620
19R-1, 10–20	157.00	1.485

Note: This table is also available in **ASCII format.**

Table T14. Carbon, nitrogen, sulfur, and hydrogen analyses of sediments from Site 1135.

Core, Type, Section	Depth (mbsf)	$CaCO_3$ (wt%)	IC (wt%)	OC (wt%)	N (wt%)	S (wt%)	H (wt%)
183-1136A-							
2R-1	5.59-5.60	91.69	11.01	0.33	0.03	BD	0.04
3R-1	15.29-15.30	95.37	11.45				
4R-1	24.80-24.81	95.24	11.43				
5R-1	34.29-34.30	94.47	11.34	BD	0.05	0.15	0.04
6R-1	43.69-43.70	94.67	11.36				
7R-1	53.15-53.16	88.87	10.67				
9R-1	70.82-70.83	92.28	11.08	0.23	0.03	BD	0.05
12R-1	99.30-99.31	11.92	1.43				
14R-1	119.13-119.14	18.18	2.18	0.44	0.03	BD	0.76

Note: BD = below detection limit. This table is also available in **ASCII format.**

Table T15. Carbon, nitrogen, sulfur, and hydrogen analyses of volcaniclastic sediments and basalts from Site 1136.

Core, section	Depth (mbsf)	TC (wt%)	N (wt%)	S (wt%)	H (wt%)
183-1136A-					
10R-1	80.17-80.21	2.50	BD	BD	0.96
10R-1	80.49-80.53	2.50	BD	BD	0.89
12R-CC	99.51-99.53	1.78	BD	0.25	0.91
14R-1	119.10-119.13	2.25	BD	BD	0.83
14R-1	119.73-119.75	2.79	BD	0.23	0.78
15R-2	128.89-128.91	0.34	BD	BD	0.23
16R-3	141.07-141.09	0.08	0.02	BD	0.32
16R-1	138.40-138.42	0.04	0.01	BD	0.28
17R-1	145.01-145.07	0.36	BD	BD	0.13
18R-3	150.61-150.63	0.04	0.02	BD	0.18
18R-4	151.68-151.71	0.38	0.02	BD	0.27

Notes: BD = below detection limit. Samples from Sections 183-1136A-10R-1 through 14R-1 are sediments with volcanic components. Samples from Sections 15R-2 through 18R-4 are basalts. This table is also available in **ASCII format.**